Continuous and discontinuous modelling of ductile fracture

Please check the document version of this publication:

Continuous and discontinuous modelling of ductile fracture

Continuous and discontinuous modelling of ductile fracture

Proefschrift

ter verkrijging van de graad van doctor
aan de Technische Universiteit Eindhoven,
op gezag van de Rector Magnificus, prof.dr. C.J. van Duijn,
voor een commissie aangewezen door het College voor Promoties
in het openbaar te verdedigen op
maandag 11 april 2005 om 16.00 uur

door

Jesus Mediavilla Varas

geboren te Ciudad Real, Spanje

Dit proefschrift is goedgekeurd door de promotor:

prof.dr.ir. M.G.D. Geers

Copromotor:
dr.ir. R.H.J. Peerlings

Contents

Summary

In many metal forming processes (e.g. blanking, trimming, clipping, machining, cutting) fracture is triggered in order to induce material separation along with a desired product geometry. This type of fracture is preceded by a certain amount of plastic deformation and requires additional energy to be supplied in order for the crack to propagate. It is known as ductile fracture, as opposed to brittle fracture (as in ceramics, concrete, etc). Ductile fracture originates at a microscopic level, as the result of voids initiated at inclusions in the material matrix. These microscopic degradation processes lead to the degradation of the macroscopic mechanical properties, causing softening, strain localisation and finally the formation of macroscopic cracks.

The initiation and propagation of cracks has traditionally been studied by fracture mechanics. Yet, the application of this theory to ductile fracture, where highly nonlinear degradation processes (material and geometrical) take place in the fracture process zone, raises many questions. To model these processes, continuum models can be used, either in the form of softening plasticity or continuum damage mechanics. Yet, continuous models can not be applied to model crack propagation, because displacements are no longer continuous across the crack. Hence, a proper model for ductile fracture requires a different approach, one that combines a continuous softening model with a strategy to represent cracks, i.e. displacement discontinuities. This has been the main goal of the present work. In a combined approach, the direction of crack propagation is automatically determined by the localisation pattern, and its rate strongly depends on the evolution of damage (or other internal variables responsible for the strain softening). This contrasts with fracture mechanics, where the material behaviour is not directly linked to the crack propagation criteria.

Softening materials have to be supplied with an internal length, which acts as a localisation limiter, thereby ensuring the well-posedness of the governing partial differential equations and mesh independent results. For this purpose, a nonlocal gradient enhancement has been used in this work, which gives similar results to nonlocal models of an integral form.

A number of numerical methods are available to model displacement discontinuities in a continuum. In the present context, we have used a remeshing strategy, since it has additional advantages when used with large strain localising material models: it prevents excessive element distortions and allows to optimise the element distri-

bution through mesh adaptivity.

As a first step towards a continuum-discontinuum approach, an uncoupled damage model is used first, in which damage merely acts as a crack initiation-propagation indicator, without causing material softening. Since uncoupled models do not lead to material localisation, no regularisation is needed. Yet, uncoupled approaches can not capture the actual failure mechanisms and therefore, in general, can give reliable results only when the size of the fracture process zone is so small that its effect can be neglected.

When the size of the fracture process zone is large enough, a truly combined model must be used, which is developed in the second part of this study. Due to softening, the transition from the continuous damage material to the discrete crack occurs gradually, with little stress redistribution, in contrast with the previous uncoupled approach. The gradient regularised softening behaviour is introduced in the yield behaviour of an elastoplastic material. The combined model has been applied satisfactorily to the prediction of ductile failure under shear loading conditions.

Third, to be able to apply the model to more general loading conditions, the material description has been improved by introducing the influence of stress triaxiality in the damage evolution of a gradient regularised elastoplastic damage model. The model has been obtained using the continuum damage mechanics concept of effective stress. Results show how compressive (tensile) states of triaxiality may increase (decrease) the material ductility.

Finally, the combined approach is applied to the modelling of actual metal forming processes, e.g. blanking, fine blanking, score forming. The gradient regularisation has been implemented in an operator-split manner, which can be very appealing for engineering purposes. To capture the large strain gradients in the localisation zones, a new mesh adaptivity criterion has been proposed. The results of the simulations are in good agreement with experimental data from literature.

Notation

In the following definitions, a Cartesian coordinate system with unit vectors $\{\vec{e}_1 \ \vec{e}_2 \ \vec{e}_3\}$ is used, with Einstein summation, i.e. repeated indices indicate summation.

Quantities

scalar	a
vector	$\vec{a} = v_i \vec{e}_i$
second order tensor	$\boldsymbol{A} = A_{ij} \vec{e}_i \otimes \vec{e}_j$
higher (n^{th}) order tensor	${}^{n}\boldsymbol{A} = A_{ij\ldots n} \vec{e}_i \otimes \vec{e}_j \ldots \otimes \vec{e}_n$
column	$\underset{\sim}{a}$
matrix	$\underline{A}$

Operations

tensorial product	$\boldsymbol{C} = \vec{a} \otimes \vec{b} = a_i b_j \vec{e}_i \otimes \vec{e}_j, \ {}^{4}\boldsymbol{C} = \boldsymbol{A} \otimes \boldsymbol{B} = A_{ij} B_{kl} \vec{e}_i \otimes \vec{e}_j \otimes \vec{e}_k \otimes \vec{e}_l$
inner product	$c = \vec{a} \cdot \vec{b} = a_i b_i, \ \boldsymbol{C} = \boldsymbol{A} \cdot \boldsymbol{B} = A_{ij} B_{jk} \vec{e}_i \otimes \vec{e}_k$
double inner product	$\boldsymbol{C} = {}^{4}\boldsymbol{A} : \boldsymbol{B} = A_{ijkl} B_{lk} \vec{e}_i \otimes \vec{e}_j, \ c = \boldsymbol{A} : \boldsymbol{B} = A_{ij} B_{ji}$
transpose	$\boldsymbol{C}^T = C_{ji} \vec{e}_i \otimes \vec{e}_j$

second order unity tensor	$\boldsymbol{I} = \delta_{ij}\vec{e}_i\otimes\vec{e}_j$
trace	$\mathrm{tr}(\boldsymbol{A}) = \boldsymbol{A} : \boldsymbol{I}$
Eulerian deviatoric part of second order tensor	$\boldsymbol{A}^d = \boldsymbol{A} - \frac{1}{3}\mathrm{tr}(\boldsymbol{A})$
fourth order unit tensor	${}^{4}\boldsymbol{I} = \delta_{il}\delta_{jk}\vec{e}_i\otimes\vec{e}_j\otimes\vec{e}_k\otimes\vec{e}_l$
symmetric fourth order unit tensor	${}^{4}\boldsymbol{I}^s = \frac{1}{2}(\delta_{il}\delta_{jk} + \delta_{ik}\delta_{jl})\vec{e}_i\otimes\vec{e}_j\otimes\vec{e}_k\otimes\vec{e}_l$
right conjugated fourth order unit tensor	${}^{4}\boldsymbol{I}^{RT} = {}^{4}I_{ijlk}\vec{e}_i\otimes\vec{e}_j\otimes\vec{e}_k\otimes\vec{e}_l$
gradient operator	$\vec{\nabla}\vec{a} = \dfrac{\partial a_j}{\partial x_i}\vec{e}_i\otimes\vec{e}_j$

Chapter 1

Introduction

1.1 Motivation

Fracture of materials, and of metals in particular, often carries a negative connotation, since it is associated with destruction and failure. In fact, the most important advances in fracture mechanics related sciences were triggered by the collapse of major structures. Huge budgets are spent every year in the maintenance of structures, ranging from bridges to airplanes, in order to prevent the development of cracks, since these may have disastrous consequences. Yet, fracture can also be beneficial. In metal forming processes such as blanking, fracture is used on purpose. Macroscopic cracks are triggered by imposing a certain amount of deformation in the product material, which allows to separate a piece from a sheet of material. The location where the onset of fracture occurs and the crack trajectory determine the geometry, and hence the quality of the product. This location and trajectory depend on the type of material, the design of the tools and the execution of the forming process. The right combination of these factors will minimise the number of secondary operations needed to reach the desired product quality. For this purpose, it is important to be able to make accurate predictions of failure.

In the past, the design of manufacturing processes was usually based on empirical rules. These rules are only applicable under very special circumstances, beyond which they are generally not valid. A modern 'damage engineering' approach requires full insight into the material separation process, which goes hand in hand with a predictive tool to handle its detailed description. A deeper understanding of the material behaviour is therefore required. The rapid developments in software and hardware allow to tackle complex modelling issues arising in metal forming which seemed unsurmountable a few decades ago. These include fracture (displacement discontinuities), softening (loss of stress with increase in strain), contact, etc. It is the aim of this work to deal with these issues, in order to further contribute to the description of failure, with an emphasis on the enabling of 'damage engineering'.

1.2   Ductile fracture

Most metals at room temperature fail in a ductile fashion, preceded by extensive plastic deformation and associated energy dissipation ('toughness'), in contrast with brittle fracture (Fig. 1.1), which occurs without noticeable permanent deformations. Originally brittle materials can also become more ductile by small changes in their composition, resulting in high performance materials, e.g. concrete with reinforced fibers. Notch blunting, necking and cup-cone failure under tension are also characteristic phenomena of ductile fracture. Crack propagation occurs in a stable manner, i.e. with crack growth resistance during crack propagation, and extensive plastic deformation. A ductile behaviour in failure is preferred over a brittle response in most engineering applications. For example, in civil or naval engineering, ductile failure can prevent the catastrophic failure of a bridge or a ship. In metal forming processes, e.g. deep drawing, ductile materials may undergo very large deformation without breaking; in blanking and machining on the other hand, ductile fracture is used to separate a metal piece in a controlled manner.
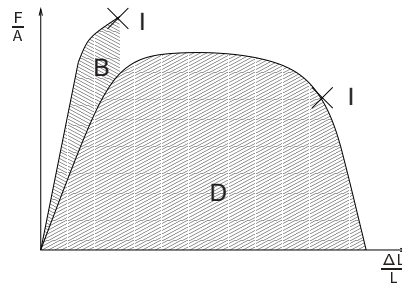
Figure 1.1 — *Ductile (D) versus brittle (B) failure. Ductile failure is accompanied by extensive plastic deformation and energy absorption ('toughness') before fracture ((I) denotes fracture initiation).*

Microscopically, ductile failure is caused by the nucleation, growth, and coalescence of voids. Nucleation occurs at inclusions and second-phase particles, ranging from 0.01 μm to 1 μm, either by interfacial decohesion or by failure of the inclusions. Void growth is promoted by positive hydrostatic stress states. Coalescence of voids can be due to a 'void sheeting mechanism" within the ligaments joining adjacent voids or by internal necking of these ligaments. Crack advancement occurs by the continuous joining of voids to the main crack. The two main factors that lead to ductile failure are plastic strain and hydrostatic stress. Depending on the type of loading, their relative importance varies. Under tension loading, both plastic strain and hydrostatic stress play an important role. Fig. 1.2 (a) shows the failure surface obtained from a tensile test, with its characteristic rounded voids. In the case of shear loading, failure is caused by plastic straining and the relative volume occupied by voids remains limited. Fig. 1.2 (b) illustrates the fracture mode in shear failure in

the score forming process. Elongated voids align and coalesce in shear localisation bands, which gives rise to macroscopic cracks.
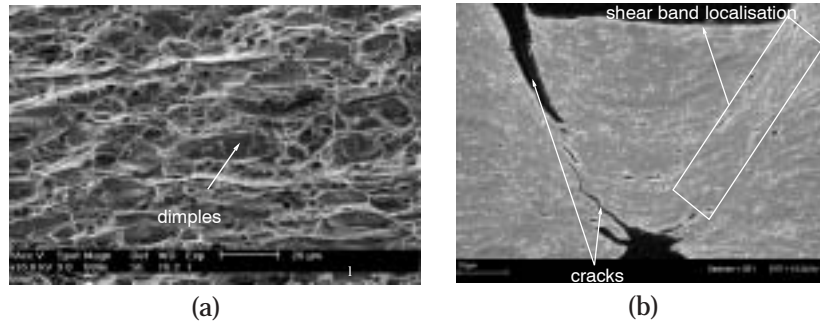
Figure 1.2 — *Ductile failure. Scanning Electron Microscopy images: (a) Tensile failure (from L. Gooren, 2004). (b) Shear failure (from S.H.A. Boers, 2003).*

1.3   Computational modelling of ductile failure

Most of the void growth leading to ductile failure occurs in the fracture process zone, i.e. a small region in front of the crack tip where the highly nonlinear processes that trigger fracture take place. At a microscopic scale, the actual material usually consists of a matrix, voids, inclusions and cracks (see Fig. 1.3). Yet, at a macroscopic level the material is generally considered as a continuum material, with perhaps a number of macroscopic cracks. In a continuum, the mechanical behaviour is commonly characterised in terms of stress and strain quantities. The averaged mechanical properties of this continuum material are inferior to those of the original material without voids, which is manifested as continuum damage. During crack propagation, softening (i.e. a decrease of the local stress measures for increasing strain) at the crack tip is maximum, resulting in a final stress equal to zero upon complete material separation. This behaviour is in sharp contrast with classical fracture mechanics, which predicts an infinite stress value at the crack tip. As the crack advances, the previous fracture process zone becomes part of the growing wake, which has failed earlier.

 In the modelling of ductile fracture three issues need to be addressed:

1. How to account efficiently for the degradation of the material mechanical properties ('softening'), still reflecting the overall impact of the microscopic processes that lead to it?

2. How to model cracks, which are displacement discontinuities, in a continuum?
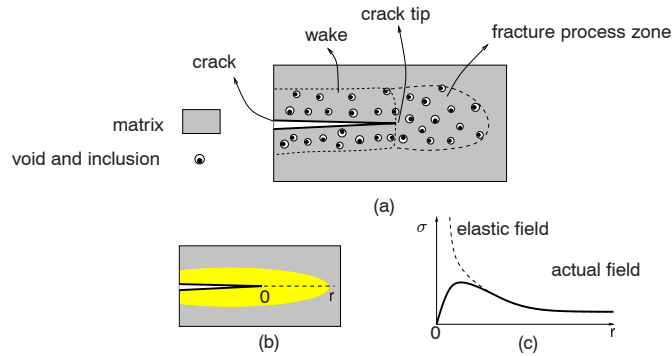
Figure 1.3 — *Stress field in the fracture process zone. (a) Actual material. (b) Continuum model plus crack. (c) Softening in the fracture process zone.*

  3. How to handle the transition from the continuum to the discontinuum in a reliable, efficient and physically relevant manner?

Most existing models deal with one or the two aspects mentioned, and seldom with all. In general the existing models to describe failure can be grouped in three classes: discontinuous, continuous and combined, although the precise distinctions are not always clear. Discontinuous models allow to incorporate displacement discontinuities, whereas continuous models describe failure as a softening continuum with continuous displacements. In Table 1.1, an attempt has been made to classify some of the existing models applicable to fracture processes. More details on each these models are given later in the introduction of the different chapters.

Table 1.1 — *Approaches to fracture*

continuous	discontinuous	combined
damage [65, 73, 118]	fracture mechanics [133]	damage/softening plasticity plus discontinuity [59, 121]
softening plasticity [40, 48]	cohesive zones [12, 44]	
smeared cracks [90, 110]	uncoupled damage plus discontinuity [30]	
embedded crack bands (weak discontinuity) [16, 92]	embedded (strong) discontinuities [9, 64, 120]	

Discontinuous models allow to model the crack geometry as it advances. The main difficulty faced by discontinuous models is how, when and where to include a discontinuity in a continuum model. Usually discontinuities are introduced rely-

ing on special numerical techniques, e.g. remeshing, interface elements, partition of unity methods (PU, XFEM), meshless methods, boundary elements (for linear problems), etc. No interaction between the crack sides exists, e.g. fracture mechanics, or it is reduced to a plane, e.g. cohesive zones, through a softening traction-opening displacement curve. Strong discontinuity models are discontinuous models obtained by applying the Dirac-delta function to a continuum softening model.

Continuous models describe the failure of the underlying microstructure in an average sense by means of a softening response. A continuous description of failure is acceptable up to the onset of fracture. At this point, the kinematics are no longer correct, since a continuous model cannot properly describe a physical crack. Damage and softening models are the most representative examples of continuous failure models. Smeared crack approaches and embedded crack models can be considered as anisotropic damage models.

The limitations of the above two approaches, too crude failure description (discontinuous) and limited kinematics (continuous), can be overcome by combining both approaches (combined model). This will allow the complete description of the failure process, from initiation to propagation. Major problems characterising local descriptions of damage (e.g. pathological localisation) are thereby to be carefully avoided. A nonlocal approach will therefore be used for the continuum part. Since the material nonlinearity is accounted for in the continuum part, there is no need for cohesive zones in the discontinuous crack model. Likewise, the crack growth is governed by the continuum degradation, instead of by separate fracture criteria.

1.4 Scope and outline

This thesis intends to provide an improved modelling of ductile fracture, with special emphasis on crack propagation. For this purpose discrete cracks are modelled in a computational framework, in which the material is described by a large strain (damage) elastoplasticity model. The presence of softening demands an internal length in order to have meaningful results, for which a gradient enhancement is used. Discrete cracks may initiate or propagate depending on the current state of damage. Attention is paid to the choice of the damage driving variables, since they have a direct effect on the direction and rate of crack growth. Anisotropic damage and plasticity, which play an important role in e.g. in sheet metal forming, are not considered here; isotropic behaviour has been assumed throughout for simplicity. Besides enabling the description of crack propagation for arbitrary crack paths, adaptive remeshing plays a paramount role in this context, both for large deformations, strain localisation and crack formation.

In Chapter 2, ductile crack propagation is assumed to be governed by an uncoupled damage variable. In this simplified model, there is no softening in the material constitutive model. Therefore no internal length is needed and a separate crack direction criterion can be used. Crack propagation is modelled by remeshing the

discretisation domain. One of the main discussion points is the robustness of the computations, which can be severely affected by the crack opening and the transfer of state variables during remeshing. A new strategy is therefore used to tackle both issues separately. To validate the model, simulations and experimental results are compared.

In Chapter 3, the effect of softening (localisation) and crack propagation is analysed using a combined approach. Softening is introduced in the yielding behaviour using a gradient regularised damage variable. Upon failure, the transition from a continuous damage state to a discrete crack takes place. The two governing partial differential equations of the gradient model, equilibrium and nonlocal averaging, are solved in a coupled manner. Due to the localisation, the crack direction is determined by the damage variable. A simplified damage evolution law is used, which is validated in mode-II crack propagation.

In Chapter 4, the effect of the stress triaxiality in the damage evolution is incorporated in the applied elastoplastic model. Attention is paid to the derivation of consistent algorithmic tangents. The model's response is compared with experiments on notched and unnotched specimens.

The knowledge obtained from the previous chapters is valorised in Chapter 5, which is devoted to industrial applications, namely: blanking, fine blanking and score forming. The implementation of the damage-elastoplasticity model is done in an operator-split manner, which enables to use it in combination with commercial codes. A new damage-rate based mesh adaptivity criterion is thereby proposed, in combination with crack propagation. One of the important points is the influence of the triaxiality state on the material ductility. The results of the simulations are compared with experiments.

Chapter 6 summarises the conclusions drawn in this thesis with recommendations for future work.

Chapter 2

Robustness and consistency of the remeshing-transfer operator in ductile fracturing [1]

Abstract: This chapter addresses the numerical simulation of quasi-static ductile fracture. The main focus is on numerical and stability aspects related to discrete crack propagation. Crack initiation and propagation are taken into account, both driven by the evolution of a discretely coupled damage variable. Discrete ductile failure is embedded in a geometrically nonlinear hyperelasto-plastic model, triggered by an appropriate criterion that has been evaluated for tensile and shear failure. A crack direction criterion is proposed, which is validated for both failure cases and which is capable of capturing the experimentally observed abrupt tensile-shear transition. In a large strain finite element context, remeshing enables to trace the crack geometry as well as to preserve an adequate element shape. Stability of the computations is an important issue during crack propagation that can be compromised by two factors, i.e. large stress redistributions during the crack opening and the transfer of variables between meshes. A numerical procedure is developed that renders crack propagation considerably more robust, independently of the mesh fineness and crack discretisation. A consistent transfer algorithm and a crack relaxation method are proposed and implemented for this purpose. Finally, illustrative simulations are compared with published experimental results to highlight the features mentioned.

2.1   Introduction

From a historical perspective, the design of metal forming processes was mostly done by trial and error. Such an experimentally driven approach is time consuming and expensive. Large amounts of costly trial products are manufactured and numerous tool designs have to be manufactured and re-engineered. During the last decades, however, the widespread use of dedicated numerical models has had a clear impact, leading to a significant reduction in production cost and time by lim-

---

[1]This chapter is based on [82].

iting the number of trial and error steps, as well as to an improvement in product quality. Computational mechanics, mostly based on finite elements, has played an important role herein. However, some manufacturing processes are still difficult to deal with from a modelling perspective, due to the inherent complexity of the underlying geometrical and physical processes.

Cutting, clipping, blanking or machining are metal forming techniques which all have in common that, starting from a piece of metal, new products are created by material separation. Complex interacting phenomena generally occur, e.g. fracture, damage, large deformations, length-scale effects, viscous and thermal effects, contact, which require the use of advanced numerical techniques. In this chapter, attention focussed on the geometrical changes that take place during these processes. Within the perspective of optimising the shape of a product, these changes have to be monitored on the basis of an adequate numerical description of the process. In particular, the ductile fracture process which governs the creation of new material surface must be described accurately and reliably.

Ductile fracture is triggered by nucleation, growth and coalescence of microscopic voids [5]. Nucleation takes place at second phase particles and inclusions in the material matrix, either by interface decohesion or particle cracking. Existing voids will grow and new voids nucleate with increasing hydrostatic stress. When the distance between the voids is sufficiently small, the ligaments joining them will start to neck and larger voids are formed by coalescence. Eventually, voids link up with the main crack. For the modelling of fracture, three different approaches can be distinguished, depending on whether the crack geometry and the microscopic processes from which it originates are taken into account, i.e. discontinuous, continuous and combined, see Fig. 2.1.
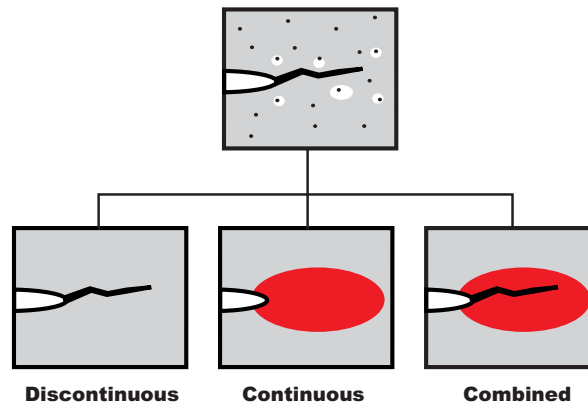

Discontinuous   **Continuous**   **Combined**

Figure 2.1 — *Crack and microstructure (above); approaches to fracture (below).*

DISCONTINUOUS APPROACH

In a discontinuous approach, the crack geometry is explicitly modelled. It is tacitly assumed that the fracture process zone (FPZ) is so small that its effect on the overall behaviour is either negligible or can be concentrated in a planar area, as in the cohesive zone models. This is mostly the case for ductile materials in which the size of the FPZ is much smaller than the product geometry. Thus, the mechanical behaviour of the surrounding material remains elasto-plastic and the cumulative effect of the growing crack is modelled by an adequate update of the geometry. Additional criteria must be formulated regarding crack initiation, propagation and crack growth direction. A drawback of this type of approach is that, in general, cracks only can initiate from a stress concentrator.

Commonly used crack growth criteria are: the J-integral [63, 107], the CTOD (Crack Tip Opening Displacement) [134] and the CTOA (Crack Tip Opening Angle) [6]. In most cases, these criteria are not based on the micromechanics that drives ductile fracture. Cohesive Zone models (CZM) [12, 44] constitute a tool for gradually developing cracks, by lumping the FPZ into a zero-width band, the behaviour of which is represented by a traction-displacement type constitutive equation.

Computationally, the discontinuous approach entails modelling strong discontinuities, i.e displacement discontinuities. This particular difficulty constituted a main challenge for many researchers who proposed a solution strategy within the context of the Finite Element Method. Among them, one may identify smeared crack [90] and embedded crack models [64, 120]. Their kinematics, however, do not allow them to model strong discontinuities. Element erosion [80] is known to cause mass loss and results in mesh dependent crack shapes. The latter problem is also common in inter-element crack models [31]. Solutions based on the partition of unity, such as the eXtended Finite Element Method (XFEM) [15, 86], are promising new techniques whose full capabilities are being further explored. Remeshing techniques of various types [22, 27] have been designed for the modelling of crack propagation. Most of the techniques listed above work well for small or moderate displacements, for which element distortion is not too severe. In metal forming processes, however, deformations tend to be extremely large and extreme element distortions would thus result if no remeshing is used. Remeshing strategies towards crack growth modelling allow to simultaneously guarantee well shaped finite elements - something which seems difficult to achieve with the other techniques listed above.

Besides the Finite Element Method, other numerical tools have also been employed. The Boundary Element Method (BEM) [1, 38] possesses appealing features for the modelling of crack propagation. Yet, its application to nonlinear constitutive models is still limited. Meshless methods or element-free methods are versatile [17, 66]. Yet, besides being computationally expensive, boundary conditions (e.g. contact) are difficult to impose.

CONTINUOUS APPROACH

In contrast with discontinuous approaches, continuous approaches fully model the FPZ. The fracture process is described by a continuous multi-dimensional model

for the material degradation. Cracks are represented by continuum regions which have lost their load-carrying capacity. This approach is sometimes referred to as local approach to fracture.

Continuous softening models can be grouped into two categories: microscopically based models and phenomenological continuum damage mechanics models. To the first category belong the works of Rice and Tracey [108], McClintock [81], Gurson [56], Tvergaard and Needleman [89, 130], who derived the macroscopic material response from the behaviour of microscopic voids. Continuum damage mechanics [65, 74] uses a homogenised representation of micro-cracks, voids and other small flaws in a macroscopic format. One or more damage variables represent the state of material degradation. The material undergoes softening, which is manifested in a loss of material strength and/or stiffness. Damage evolution is governed by a phenomenological evolution law, which depends on some measure for the governing strain and/or stress state. Various plastic damage models of this type have been developed, both for infinitesimal [10] and finite strain problems [118].

The main drawback of a local description of softening behaviour is the well-known pathological localisation such models exhibit. This is the consequence of the governing partial differential equations becoming ill-posed, which leads to mesh dependence in a numerical framework. In order to overcome this, a number of regularisation techniques have been developed (see Ref. [41] for an overview): strongly nonlocal, gradient (weakly nonlocal), rate-dependent and micro-polar models. Theories of these types are gradually also becoming available in large-strain plasticity, see Geers et al. [53] and references therein. Most of these models incorporate an internal length parameter, which is the most straightforward manner to enrich a macroscopic constitutive equation from the perspective of the underlying microstructure. The existence of an intrinsic relation between this length scale and the underlying microstructural processes is obvious. Yet, its quantitative determination remains a difficult and debatable issue.

In terms of numerical implementation, continuous degradation models have the advantage of not requiring special discretisation techniques in order to trace the propagation of a discrete crack. The continuous representation of this crack simply follows from the evolution of the damage field. However, since the regions in which this damage concentrates are usually small compared with the dimensions of the component, some form of mesh adaptivity is nevertheless required to accurately capture it in large-scale computations.

COMBINED CONTINUOUS-DISCONTINUOUS APPROACH

It can be concluded from the above that a discontinuous approach can be used to describe crack propagation, yet in general it does not properly capture the mechanisms leading to it. On the other hand, a continuous approach can describe these mechanisms more accurately, but cannot model the resulting crack geometry. These conclusions naturally lead to the idea of an integrated continuous-discontinuous approach in which the degradation in the FPZ is modelled by a (regularised) softening material description and a discontinuity is introduced when the local material

strength is exhausted. Crack propagation is governed by the interaction between the discrete crack and the weakened material region around it. Unlike discontinuous models, no additional assumptions have to be made for the crack initiation and propagation, nor for the crack orientation. From a numerical point of view, the modelling of a discrete crack can be done by any of the techniques that were discussed above.

Robust regularised damage models for ductile fracture are not yet very commonly available. This explains why only few attempts to a combined model have been made so far. In a quasi-brittle fracture context Peerlings et al. [98] used an element killing technique to model crack propagation of a gradient regularised model. Yet, the treatment of a crack once it appeared as a discontinuity did not have emphasis. In recent years regularised damage models have been used in combination with XFEM to model crack propagation [121, 136]. This combination appears to be powerful for the modelling of crack propagation at small strains. Yet, in a large strain setting XFEM must be combined with remeshing to avoid large element distortions, hence losing part of its main attraction.

AN UNCOUPLED CONTINUOUS-DISCONTINUOUS APPROACH

As a first step towards a fully continuous-discontinuous modelling, we pursue a simplified strategy in this chapter, in which a measure of the microstructural changes in the FPZ is computed, but its influence on the material behaviour is neglected, as proposed by Brokken et al. [29, 30]. Discrete cracks are modelled, using a ductile damage variable as a crack initiation and propagation indicator. This damage variable does not influence the material behaviour until it reaches a critical value at which a new crack increment is inserted in the problem. Since there is no actual material softening, no regularisation technique is necessary. This approach can be justified when the fracture process zone is small and length scale effects are negligible at the macro scale. Remeshing is used to trace the crack path, to relax the forces at the cracked faces and to prevent large element distortions. Computationally, two factors can have a deteriorating effect on the stability of the computations: the transfer of variables between subsequent meshes and the geometric changes during the creation of new surface. Therefore, particular attention is given to the robustness of the numerical algorithm for crack propagation. Consistency and equilibrium of the transferred variables are addressed in detail; whereas a nodal relaxation procedure is used to allow a gradual crack opening. Additionally, determining the proper crack growth direction under different loading conditions has also been addressed.

The outline of this chapter is as follows. Section 2.2 deals with the continuum model and the discontinuous crack modelling: the hyperelasto-plasticity model which forms the basis of our developments, the uncoupled damage and the crack growth direction. Section 2.3 covers the consistent transport, remeshing, crack relaxation and related aspects of the numerical implementation. In Section 2.4 some examples are shown to illustrate the adopted methodology and the achieved improvements. Finally conclusions are drawn in Section 2.5.

2.2   Constitutive modelling

2.2.1   Large deformation elasto-plasticity model

To describe the large elasto-plastic strains of the considered ductile material, a hyper-elasto-plastic material has been adopted which is based on earlier work by Simo and Miehe [119]. This rate independent, large strain elasto-plasticity model is based on the use of a hyperelastic potential for the elastic part of the deformation and a plastic flow rule which is entirely formulated on the spatial configuration. Evidently, stresses need not be integrated, since they can be obtained directly through evaluation of the hyperelastic stress-strain relation. Below, only the most relevant equations are presented. For a detailed derivation and implementation the reader is referred to Refs. [53, 119].

Using crystal plasticity arguments, a stress-free local intermediate configuration is considered, which motivates the standard multiplicative split of the deformation gradient into an elastic and a plastic part

$$\boldsymbol{F} \; = \; \boldsymbol{F}_e \cdot \boldsymbol{F}_p \, . \tag{2.1}$$

The hyper-elastic relationship between stresses and strains reads

$$\boldsymbol{\tau} \; = \; \frac{K}{2} \left(J^2 - 1 \right) \, \boldsymbol{I} + G \, \bar{\boldsymbol{b}}_e^d \, , \tag{2.2}$$

where $\boldsymbol{\tau}$ is the Kirchhoff stress tensor, J is the volume change ratio

$$J \; = \; \det \left(\boldsymbol{F} \right) \tag{2.3}$$

and $\bar{\boldsymbol{b}}_e^d$ is the deviatoric part of the isochoric elastic left Cauchy-Green tensor [1]. K and G are the bulk modulus and the shear modulus respectively. The elastic stored energy potential W from which the above stress-strain relation (2.2) is derived reads

$$W \; = \; \frac{1}{2} K \left[\frac{1}{2} \left(J^2 - 1 \right) - \ln J \right] + \frac{1}{2} G \left(\mathrm{tr} \bar{\boldsymbol{b}}_e^d - 3 \right) \, . \tag{2.4}$$

Plastic flow is assumed to be isochoric

$$\det \left(\boldsymbol{F}_p \right) = 1 \rightarrow J = \det \left(\boldsymbol{F} \right) = \det \left(\boldsymbol{F}_e \right) \, . \tag{2.5}$$

Rather than expressing the flow rule in terms of a plastic strain rate, the formulation derived in Ref. [119] is used. Realising that $\boldsymbol{b}_e$ is the push-forward of $\boldsymbol{C}_p^{-1}$ with the deformation $\boldsymbol{F}$, i.e. $\boldsymbol{b}_e \; = \; \boldsymbol{F} \cdot \boldsymbol{C}_p^{-1} \cdot \boldsymbol{F}^T$, the Lie derivative of $\boldsymbol{b}_e$ is obtained as the push-forward of the material time-derivative of $\boldsymbol{C}_p^{-1}$ (pull-back of $\boldsymbol{b}_e$)

$$\overset{\triangledown}{\boldsymbol{b}}_e = \; \boldsymbol{F} \cdot \dot{\boldsymbol{C}}_p^{-1} \cdot \boldsymbol{F}^T \, . \tag{2.6}$$

---

[1]In the following, $\boldsymbol{A}^d$ will denote the deviatoric part of a tensor $\boldsymbol{A}$.

The associative flow rule, derived from the principle of maximum plastic dissipation reads [117]

$$\left[\overset{\triangledown}{\boldsymbol{b}}_e\right]^d = -3\,\dot{\varepsilon}_p\,\frac{\boldsymbol{\tau}^d}{\tau_{eq}}\cdot\boldsymbol{b}_e\;,\tag{2.7}$$

which for small elastic deformations may be simplified to (Ref. [119])

$$\left[\overset{\triangledown}{\boldsymbol{b}}_e\right]^d = -3\,\dot{\varepsilon}_p\,\frac{\boldsymbol{\tau}^d}{\tau_{eq}}\;.\tag{2.8}$$

The equivalent von Mises stress is defined as

$$\tau_{eq} = \sqrt{\frac{3}{2}\,\boldsymbol{\tau}^d\,:\,\boldsymbol{\tau}^d}\tag{2.9}$$

and the effective plastic strain rate $\dot{\varepsilon}_p$ as

$$\dot{\varepsilon}_p = \sqrt{\frac{1}{6}\left[\overset{\triangledown}{\boldsymbol{b}}_e\right]^d\,:\,\left[\overset{\triangledown}{\boldsymbol{b}}_e\right]^d}\;.\tag{2.10}$$

A hardening law relates the yield stress to the effective plastic strain, conveniently expressed as

$$\tau_y = \tau_y(\varepsilon_p)\tag{2.11}$$

and the yield function is defined as

$$\phi = \tau_{eq} - \tau_y\;.\tag{2.12}$$

The model is finally completed by the standard Kuhn-Tucker loading-unloading conditions

$$\dot{\gamma} \geq 0\,,\qquad \phi(\boldsymbol{\tau},\varepsilon_p) \leq 0\,,\qquad \dot{\gamma}\,\phi(\boldsymbol{\tau},\varepsilon_p) = 0\tag{2.13}$$

and the consistency condition

$$\dot{\gamma}\,\dot{\phi}(\boldsymbol{\tau},\varepsilon_p) = 0\;.\tag{2.14}$$

2.2.2   Uncoupled damage model

In the uncoupled damage framework which we adopt here, cracks initiate or propagate at material points that reach a critical level of degradation, characterised by a ductile damage variable ω_p. Initially we have $\omega_p = 0$. Upon loading ω_p may grow with increasing plastic deformation until the material fails at $\omega_p = 1$. It is emphasised that the damage variable ω_p is uncoupled from the constitutive equations and

thus does not influence the material behaviour until $\omega_p = 1$. It merely acts as a crack initiation-propagation indicator [20, 111].

For the damage evolution, an earlier version of the criterion proposed by Goijaerts et al. [55] has been adopted, which is in fact equal to Oyane et al.'s model [93] in case of tension. Based on the theory of porous materials in elastoplasticity, the ductile damage evolution can be written in rate form as

$$\dot{\omega}_p \;=\; \frac{1}{C} \left\langle 1 + A\, \frac{\tau_h}{\tau_{eq}} \right\rangle \dot{\varepsilon}_p \;, \quad 0 \leq \omega_p \leq 1 \;. \tag{2.15}$$

Here τ_h and τ_{eq} stand for the hydrostatic and equivalent deviatoric stress respectively, C is a material parameter which governs the onset of fracture ($\omega_p = 1$) and A reflects the degree of interaction between void growth and triaxiality ($\frac{\tau_h}{\tau_{eq}}$). The Macaulay brackets $\langle \cdot \rangle$ are defined as $\langle x \rangle = \frac{1}{2}(x + |x|)$ and account for the fact that damage can not decrease.

The above relation (2.15), like other ductile damage models [56, 108], is driven by the plastic deformation and the hydrostatic stress. Triaxiality acts as a promotor of damage growth.

2.2.3   Crack growth direction

Damage growth and crack orientation are closely related, since cracks tend to propagate in the direction where the deformation (ε_p) and damage (ω_p) are more severe. Based on this concept, Brokken [29, 30], was able to predict satisfactorily the crack trajectories in a metal blanking process, using a damage criterion based on Rice and Tracey's void growth model. In the blanking analyses, a plastic shear band developed which guided the crack(s). Yet, there are other cases in which the spatial damage distribution does not provide the proper crack growth direction. Consequently, experimental results and associated numerical predictions do not match. For example, in a Compact Tension (CT) specimen under tensile loading, two damage regions originate from the plastic deformations at the crack tip (Eq. (2.15)), which would result in crack growth at angles of $\pm 70^o$ with the horizontal direction, hence in disagreement with the generally observed horizontal path [39] (See Fig 2.2). This nonphysical result is due to the inability of the damage formulation to distinguish between shear-dominated fracture (as in the blanking simulations) and fracture under predominantly tensile stress (as in the CT test).

In order to overcome this problem, a crack orientation criterion is added to the formulation, which provides more realistic crack paths. In brittle fracture, a number of reliable crack direction criteria exist, e.g. the maximum hoop stress (MHS) [46], the minimum strain energy density [114] and the maximum energy release criteria [139]. For this type of fracture, these criteria have proven to agree reasonably well with experimental data for the entire loading range (mode-I to mode-II) [78]. Yet, ductile fracture under mixed-mode conditions shows a less consistent behaviour. When
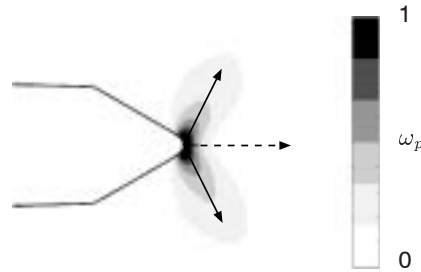
Figure 2.2 — *Crack direction. Generally observed straight crack direction (dashed arrow) versus predicted crack directions based on the damage field.*

tension is dominant, the above mentioned brittle criteria still show a good agreement with ductile fracture experiments. However, for increasing shear, a change in crack growth behaviour is observed and large discrepancies arise. Under pure shear, cracks follow a straight path, rather than the predicted angles at $\pm 70^o$ (See Fig. 2.6). Experiments show that at a certain tensile-shear loading ratio, an abrupt change of the crack growth direction occurs. This change is related to a transition from tensile to shear dominated crack growth. The micro-mechanics of ductile crack growth show two competing mechanisms which act simultaneously at a crack tip, i.e. nucleation and growth of voids on the blunt side and localised plastic deformation on the sharp side (Fig. 2.3). Under dominant tension (near mode-I), the first
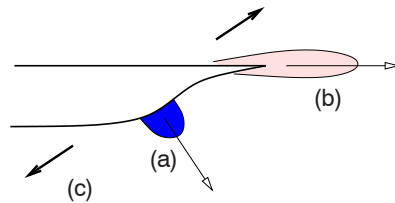
Figure 2.3 — *Possible crack growth directions of ductile materials under mixed loading. The picture shows the deformed state of an initially rounded notch. (a) blunt notch: maximum hydrostatic stress (mode-I direction); (b) sharp notch: maximum shear strain (mode-II direction); (c) loading direction.*

mechanism prevails, while under dominant shear (mode-II), the second mechanism prevails [54]. Besides the loading type, the governing mechanism will depend upon the work hardening and distribution and size of inclusions in the material [21]. This means that the mode mixity at which the transition between the two mechanisms

takes places varies from material to material.

In order to predict the differences under tensile and shear loading in ductile fracture, a number of phenomenological models have been proposed. Hallback [57] observed that under predominant shear, cracks tend to follow the maximum shear stress; whereas under predominant tension they tend to follow the maximum hoop stress. The same was observed by Chao et al. [33], who also found that either tensile or shear failure will occur depending on the ratio between shear and tensile strength. According to Sutton [124], depending on the triaxiality, cracks will either grow in the direction of maximum triaxiality (mode-I) or the maximum effective stress direction (mode-II). Sutton later applied a CTOD model for predicting the onset and direction of mixed mode fracture [125]. Pirondi et al. [103] found that cracks orient themselves along the maximum tangential stress or the maximum shear strain direction, depending on whether mode-I or mode-II is dominant.

Based on these observations, a simple criterion is proposed here which properly captures the tensile to shear transition. The criterion is based on the fact that the maximum hoop stress ($\tau_{\theta\theta}$) and maximum tangential stress ($\tau_{r\theta}$) provide the correct directions under near mode-I and mode-II conditions respectively. A mixed-mode scalar stress measure τ_m is therefore defined as

$$\tau_m(\theta) = \max\left(\left\langle(1-\alpha)\tau_{\theta\theta}(\theta)\right\rangle, \alpha\left|\tau_{r\theta}(\theta)\right|\right), \qquad 0 \leq \alpha \leq 1, \qquad (2.16)$$

where $\tau_{\theta\theta}$ and $\tau_{r\theta}$ are the polar components of the stress tensor with respect to the crack tip, shown in Fig. 2.4, and α is a material dependent parameter which sets the tensile to shear transition. Crack growth is now assumed to occur in the direction
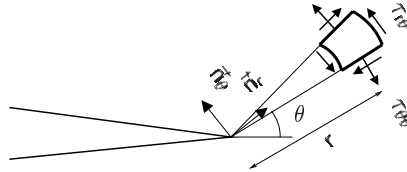
Figure 2.4 — *Polar reference system at the crack tip and relevant stress components.*

θ_{dir} in which τ_m has its maximum. For $\alpha = 0$ and $\alpha = 1$ this criterion is equal to the maximum $\tau_{\theta\theta}$ and maximum $\tau_{r\theta}$ criteria, respectively. The parameter α must be determined from experiments, so that the transition from mode-I to mode-II type of growth takes place at the experimentally observed tensile-shear loading ratio. The proposed criterion unifies the two types of crack growth, which originate from the two competing mechanisms acting at a crack tip. It does not require any preliminary assessment of the loading type, which is convenient for the simulation of complex multi-mode ductile fracture processes.

Even though the fields in ductile fracture evidently differ from those predicted by linear fracture mechanics, it remains interesting to assess the newly proposed

crack direction criterion (2.16) for these particular well-known fields. The use of a HRR-field [63, 107], common in elasto-plastic fracture mechanics, would change the picture only quantitatively. Consider the well-known expressions of the mixed mode stress components $\tau_{\theta\theta}$ and $\tau_{r\theta}$ in linear fracture mechanics

$$\tau_{\theta\theta} = \frac{1}{\sqrt{2\,\pi\,r}} \cos\left(\frac{\theta}{2}\right)\left(K_I \cos^2\left(\frac{\theta}{2}\right) - \frac{3}{2} K_{II} \sin(\theta)\right), \qquad (2.17)$$

$$\tau_{r\theta} = \frac{1}{2\sqrt{2\,\pi\,r}} \cos\left(\frac{\theta}{2}\right)\left(K_I \sin(\theta) + K_{II}\left(3\cos(\theta) - 1\right)\right), \quad (2.18)$$

where K_I and K_{II} are the mode I and mode II stress intensity factors respectively. The mixed mode stress intensity factor is defined as

$$K = \sqrt{K_I{}^2 + K_{II}{}^2}. \qquad (2.19)$$

The mode mixity ratio can be expressed in terms of the angle β where

$$\tan(\beta) = \frac{K_I}{K_{II}}. \qquad (2.20)$$

In mode-I, the angle $\beta = 90^o$ ($K_{II} = 0$); while in mode-II, $\beta = 0^o$ ($K_I = 0$). Equations (2.17), (2.18), (2.19) and (2.20) have been substituted in (2.16), leading to an expression of the form

$$\tau_m = f(\theta,\,\beta,\,\alpha), \qquad (2.21)$$

for a given distance r and a stress intensity K. Fig. 2.5 (a) shows how the crack direction is computed. The diagram shows the two competing components in (2.16) as a function of the angle θ for $\beta = 30^o$ and $\alpha = 0.5$. The mixed mode stress $\tau_m(\theta)$ follows the maximum of these two curves and has its maximum for $\theta_{dir} = -60^o$. Clearly, in this case the mode-I mechanism governs over the crack growth. Fig. 2.5 (b) illustrates the influence of the parameter α on $\tau_m(\theta)$. Depending on α, $\langle(1 - \alpha)\tau_{\theta\theta}\rangle$ will be larger or smaller than $\alpha|\tau_{r\theta}|$ and cracks will then follow the maximum $\tau_{\theta\theta}$ criterion (mode-I) or the maximum $\tau_{r\theta}$ criterion (mode-II), respectively.

Fig. 2.6 shows the crack direction angles θ_{dir} as function of the mode mixity angle β for a number of α values. For each α a curve has been plotted; the curve for $\alpha = 0.64$ has been drawn as a thick curve. The bottom and top curves represent the angles predicted by the maximum $\tau_{r\theta}$ ($\alpha = 1$) and the $\tau_{\theta\theta}$ ($\alpha = 0$) criterion respectively. For small β's, this curve follows that of the maximum hoop stress criterion. At an angle of approximately 52° however, a sudden change of direction is predicted and for $\beta > 52^o$ the tangential stress criterion is followed. For other values of α the mixity β at which this transition occurs differs. Note that only for α within the range $(0.54 - 0.72)$, the expected abrupt change in crack growth mode is seen. For $\alpha \lesssim 0.54$, there is no transition and the τ_m and $\tau_{\theta\theta}$ criteria coincide for all mode mixities β. No transition is either observed for $\alpha \gtrsim 0.72$ for which the τ_m and $\tau_{r\theta}$ criterion coincide for all β.
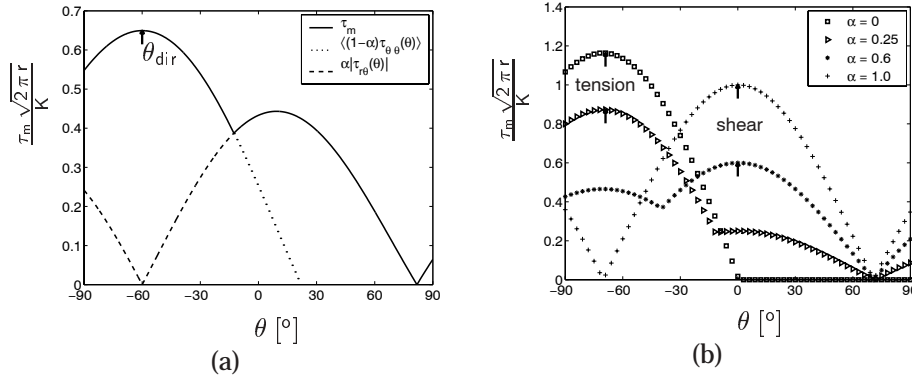
Figure 2.5 — *(a) Computation of the crack direction* θ_{dir} *($\beta = 30^o$, $\alpha = 0.5$); (b) influence of* α *($\beta = 30^o$). Arrows denote the direction of crack growth.*
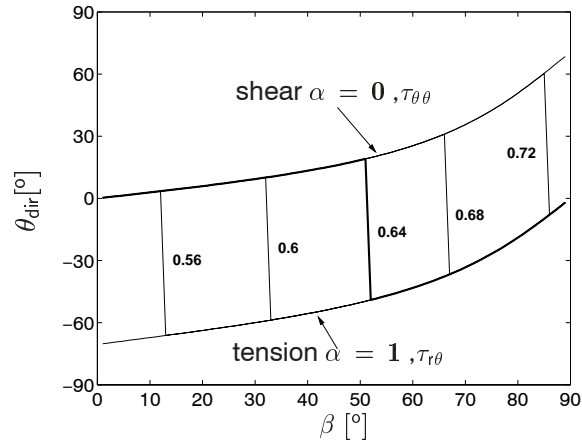
Figure 2.6 — *Crack propagation angle* θ_{dir} *versus mode mixity* β *for different values of* α.

2.3   Aspects of the finite element implementation

The finite element formulation of the large strain elasto-plastic model follows standard procedures, for which details can be found in Refs. [18, 115, 116]. An Updated Lagrangian formulation has been chosen, whereby equilibrium is expressed with respect to the current configuration. The integration of the rate evolution equations is accomplished by a radial return mapping algorithm, based on an implicit backward-

Euler rule.

After elaboration of the weak form, insertion of the constitutive equations and the return mapping, followed by a consistent linearisation and discretisation by finite elements, the usual Newton-Raphson iterative procedure is obtained, which is written in a matrix form as

$$\underline{K}^{(i)} \, \delta\Delta\underline{u} \ = \ \underline{f}_{ext} - \underline{f}_{int}^{(i)} \, , \tag{2.22}$$

where $\underline{K}^{(i)}$ is the consistent stiffness matrix obtained from the ith iteration (full Newton-Raphson), $\underline{f}_{ext}$ and $\underline{f}_{int}$ are the columns of the nodal external and internal forces respectively, and $\delta\Delta\underline{u}$ is the column with the incremental nodal displacements $\Delta\underline{u}$. The entire algorithm has been formulated in terms of incremental displacements $\Delta\underline{u}$, rather than the total displacement $\underline{u}$, for compatibility with the transfer operator (see Section 2.3.2).

The damage variable ω_p is updated at the end of every increment by a mid-point numerical integration rule

$$\omega_p \ = \ \omega_{p_t} + \frac{h_\omega + h_\omega^t}{2}\Delta\varepsilon_p \quad \text{with} \quad h_\omega \ = \ \frac{1}{C}\langle 1 + \frac{A\,\tau_h}{\tau_{eq}}\rangle \, , \tag{2.23}$$

where *t* denotes the previous converged increment.

The computational scheme which is used to simulate crack initiation and crack growth is illustrated in Fig. 2.7. Loads and imposed displacements are applied incrementally. An automatic load increment size algorithm adjusts the load increment size so that convergence is reached within a certain number of iterations. The lower-left part of the diagram corresponds to the case of crack propagation. Full remeshing is done to accommodate every new crack segment of the discretised crack. The lower-right part is a regular remeshing step, aimed at keeping the mesh elements well-shaped.

Remeshing is inevitably accompanied by the transfer of state variables. This transfer introduces errors in the state variables, thus leading to inconsistencies between state variables and violations of the equilibrium equations. To minimise inconsistencies, a minimum set of state variables is transferred and the remaining variables are consistently recovered. Equilibrium is then restored in an elastic null-step, after which remaining inconsistencies in the loading-unloading conditions are corrected. Details of these operations, which have been found to be critical for the numerical stability of the simulations, are given in Section 2.3.2.

Crack initiation and propagation are checked after every converged increment. Initiation will occur at any boundary node that satisfies $\omega_p = 1$ (nodal values are obtained by extrapolation from the integration points) and existing cracks will continue to propagate as long as $\omega_p = 1$ at the crack tip. However, in order to reduce the influence of local damage variations which are a result of the discretisation, the damage variable ω_p at the crack tip is computed as the weighted average of an algorithmic
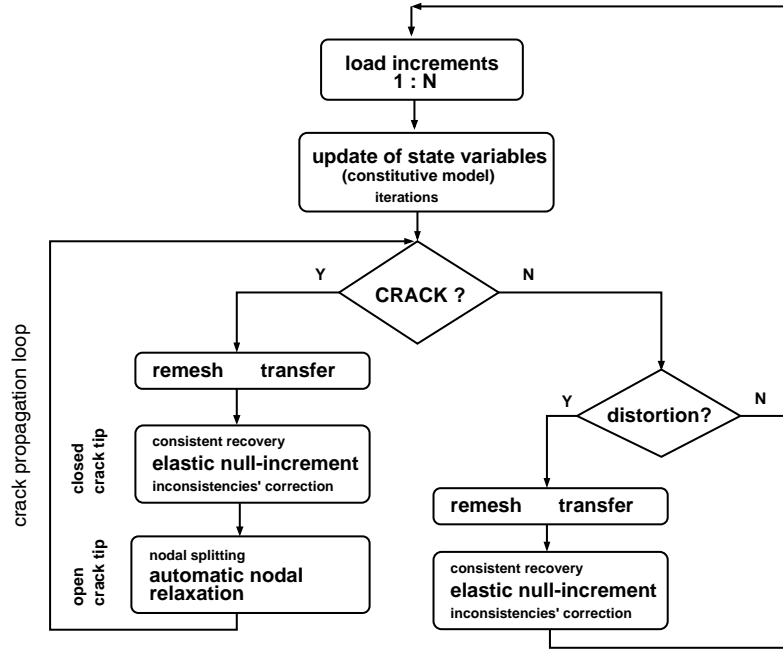
Figure 2.7 — *Computational scheme.*

value $\hat{\omega}_p$ in a region near the tip according to

$$\omega_p = \frac{\int_\Omega \mathsf{w}\,\hat{\omega}_p\,d\Omega}{\int_\Omega \mathsf{w}\,d\Omega}\,. \tag{2.24}$$

The algorithmic damage $\hat{\omega}_p$ is computed according to Eq. (2.15), but it may become larger than one. For the weighting function w, which decreases monotonically away from the crack tip, a Gaussian distribution has been assumed [135]. The averaging area Ω has been represented in Fig. 2.8, which is usually a half circle of radius R, containing at least two or three element rings. The crack orientation is computed using Eq. (2.16). In order to have a more reliable crack direction value, the crack direction is computed as the mean of the angles Θ_i at various distances d_i (Fig. 2.8). The distances d_i should not be too small, because the crack would then start to zig-zag, nor too large, because they would not be representative for the crack tip. For accuracy, the minimum distance should be large enough to contain a number of elements around the crack tip.

The insertion of a new crack segment is the most critical point for the stability of the computations, since in addition to the transfer errors the boundary conditions of the problem change. This combined effect may cause a large unbalance between internal and external forces and result in the breakdown of the incremental-iterative
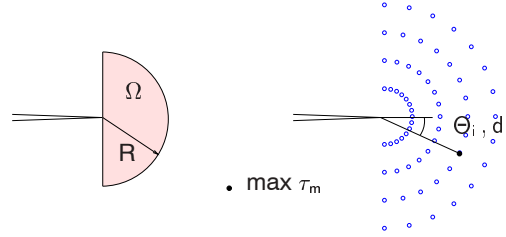
Figure 2.8 — *Damage averaging area for crack propagation (left); crack direction (right).*

algorithm. In order to eliminate this source of instability, a procedure is proposed which deals with both unbalance sources separately. First, the transfer unbalance is relaxed following the same steps which are also taken after regular remeshing. These steps will be detailed in Section 2.3.2. Secondly, the unbalance which results from the change in geometry (new crack segment) is removed by nodal relaxation (see Section 2.3.3). The step-wise removal of the unbalance forces renders a crack propagation algorithm that converges even for extremely coarse meshes and crack discretisations, as will be demonstrated.

Further loading will continue once all cracks have stopped to propagate. Multiple cracks can be present and propagate simultaneously. Crack closure is not considered here. A detailed description of the algorithm is given next, in particular remeshing, transfer, consistency, equilibrium and nodal relaxation issues are discussed.

2.3.1   Remeshing

Remeshing is done on the deformed geometry, which is defined by the nodal positions of the last converged load increment. Relying on a good performance in nearly incompressible problems (e.g. elastoplasticity), quadrilateral elements with reduced integration are used.

Besides preventing excessive element distortions, full remeshing is also used to model discrete crack propagation. Compared to local remeshing [76], in which the mesh in only a small region around the crack tip is adapted, full remeshing has the advantage of keeping the mesh elements in an overall better shape. Yet, it introduces more diffusion. As indicated above, for the sake of robustness of the crack propagation procedure, transfer and geometrical unbalances will be separated. This is done by generating a mesh which conforms to the new crack segment, but with the elements on both sides are still connected, thus preventing its opening (see Fig. 2.9). As a result, transfer unbalances can be removed prior to opening the crack and thus introducing geometrical unbalance. The crack segment length is usually taken in the order of a few elements at the crack tip, e.g. 2-10.

(a)   (b)
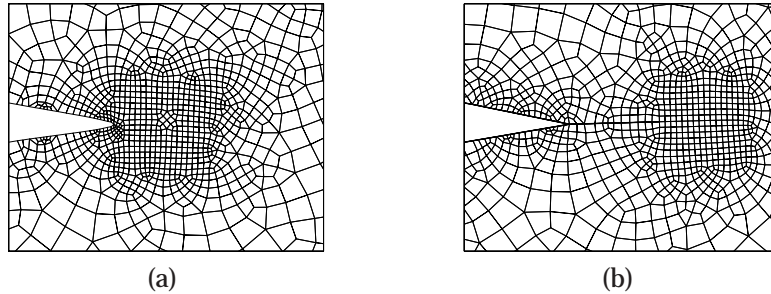
Figure 2.9 — *Meshing of an embedded crack segment allows the separation of the transfer and geometric unbalances: (a) old mesh, (b) new mesh with embedded new crack segment (still closed).*

2.3.2   Transfer, consistent recovery and equilibrium

Upon remeshing, since hyperelasto-plastic materials are history dependent, material history data and internal variables have to be mapped from the old to the new mesh. In practice, this involves transferring state variables from a discrete number of points (nodes and integration points) of the old mesh to another set of points in the new mesh. Transfer issues, in spite of their importance, mostly receive little attention. A reliable transfer operator should: (1) preserve consistency with the constitutive equations, (2) satisfy equilibrium, (3) minimise numerical diffusion and (4) ensure compatibility with the boundary conditions [101]. Lee and Bathe devised several mapping schemes for a large deformation analysis [71]. Perić et al. [101] wrote a comprehensive treaty on the use of transfer operators, which was applied to small strain plasticity. A general overview can be found in Ref. [24] (Section 3.2).

Transfer

Since state variables are stored at both integration points and nodes, two different types of transfer operators are generally needed [71, 101]. However, since remeshing is done here in the deformed configuration, within an updated lagrangian approach, only integration point variables need to be transferred. The displacement data of the nodes is already present in the updated geometry of the problem. Besides simplifying the algorithm (only one type of transfer operator), this directly eliminates inconsistencies. The transfer of nodal displacements would not agree with the transferred kinematic quantities at integration points. Since nodal displacements are not transferred, the model has to be formulated in an incremental format. In fact, this only entails a minor change of the constitutive algorithm compared with Ref. [53], namely in the incremental deformation tensor f (needed for the stress update), which is de-

fined as

$$f \;=\; F \cdot F_t^{-1} \;,\tag{2.25}$$

where the index t refers to the last converged increment. In terms of the incremental displacements ($\Delta\vec{u}$), this tensor reads

$$f \;=\; \left(\, I \;-\; \vec{\nabla}\Delta\vec{u}\,\right)^{-T}.\tag{2.26}$$

The transfer algorithm has been adopted largely from Perić et al. (Ref. [101], Section 3.1). The steps involved have been depicted in Fig. 2.10:

(a)   (b)   (c)   (d)
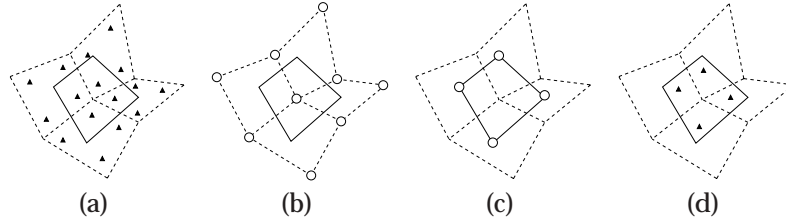
Figure 2.10 — *Transport: (a) old mesh Gauss points; (b) old mesh nodes; (c) new mesh nodes; (d) new mesh Gauss points. Old elements are drawn with dashed lines and the new element with solid lines.*

- *(a) → (b)* Extrapolation towards a continuous state variable field on the old mesh.

  Using a standard extrapolation and nodal averaging, a continuous state variable field is obtained from the discrete values known at the integration points. Evidently, this step constitutes an important source of diffusion. More advanced techniques have also been proposed to limit this. For instance, Hinton and Cambell [61] used a global least squares approximation and Loubignac [77] used an iterative procedure to construct a smooth stress field.

- *(b) → (c)* Interpolation towards a continuous state variable field on the new mesh.

  Having a continuous state variable field on the old mesh, defined by the extrapolated nodal values and the old interpolation functions, a continuous state variable field is easily obtained on the new mesh by direct interpolation. For every new node, the element of the old mesh in which this node is situated is determined, as well as its associated local isoparametric coordinates. The new nodal values are then easily computed using the old shape functions. The continuous field is now defined by these nodal values and the shape functions of the new mesh.

- *(c) → (d)* Interpolation to the discrete set of Gauss points.

  The new Gauss point variables can now be readily computed with the shape functions of the new mesh.

Less diffusion can be achieved by computing the new integration point variables directly from the continuous stress field on the old mesh [71]. Yet, this introduces more inconsistencies as was shown in Ref. [95].

Consistent recovery

Consistency here refers to the correct mutual dependencies between the transferred state variables on the basis of the governing constitutive equations. Ortiz and Quigley [91] showed that by applying the Hu-Washizu principle, a consistent transfer operator can be derived. Eventually, after a number the simplifications, this procedure was reduced to a common transfer scheme. Camacho and Ortiz [32] discussed in detail the problem of transfer consistency in terms of volumetric (elastic and plastic) strains. Logarithmic measures of the deformation gradients were transferred in order to ensure preservation of the volumetric parts of these strains.

Consistency among field variables may be lost as a result of the fact that nonlinear relations between them are not carried over correctly by a linear transfer operator. It should be noted in this context that the transfer operator which was explained above is such a linear operator. Inconsistencies can be eliminated by transferring a reduced, yet fully representative, set of state variables, from which the remaining variables can be derived using the very constitutive equations, which would otherwise be violated [47]. In the present framework, the reduced set of variables consists of the Kirchoff stress tensor τ and the yield stress τ_y. The transferred variables, τ' and τ'_y, along with the new nodal coordinates $\vec{x}'_I$, fully represent the state in the new mesh [2].

The choice of the stress tensor τ' is not arbitrary. The transfer of, let us say b'_e, would invoke large errors in the volumetric part of the stress tensor because of the volume change ratio (see Eq. (2.2)) would then have to be determined via a nonlinear relation. Whereas an error in τ' has a linear effect on J'^2 (see Eq. (2.27)), an error in b'_e is raised to the power of three (see Eq. (2.30)). Moreover, for very small deformations, b'_e can be very close to I, thus leading to large round-off errors. The yield stress τ'_y characterises the plastic straining history of the material. Rather than the effective plastic strain, the yield stress is transferred because this quantity can be directly used in the yield condition, without first invoking the - possibly nonlinear - hardening law.

Using this minimal set, the variables J' and b'_e are easily recovered from the vol-

---

[2]transferred variables or quantities derived thereof are denoted by a prime ($'$)

umetric and deviatoric parts of τ' via Eq. (2.2):

$$J' = \sqrt{1 + \frac{2}{3\,K}\mathrm{tr}(\tau')}\,, \qquad (2.27)$$

$$\bar{b}'_e = \frac{1}{G}\,\tau'^d\,, \qquad (2.28)$$

where $\mathrm{tr}(\tau')$ stands for the trace of the stress tensor τ'. This gives $b_e'^d$

$$\left[b'_e\right]^d = J'^{\frac{2}{3}}\left[\bar{b}'_e\right]^d\,. \qquad (2.29)$$

Since plastic deformation is isochoric, the volumetric part of b'_e can be obtained by solving the equation for the unknown $\mathrm{tr}(b'_e)$

$$\det\left(b'_e\right) = J'^2\,, \qquad (2.30)$$

as explained in Refs. [53, 119]. The effective plastic strain in the transferred state can be recovered by solving the hardening relation $\tau_y(\varepsilon'_p) = \tau'_y$ for it.

Nevertheless, inconsistencies between the transferred stress tensor and the plastic deformation may still arise, in the sense that stress states which were on the yield surface $\tau_{eq}(\tau) = \tau_y$ before the transfer, may no longer lie on it afterwards.

This is easily illustrated with a simple example. Let us assume that the state at a new integration point, defined by $\{\tau', \tau'_y\}$, can be computed from just two integration points in the old mesh, whose stress states are given by τ_1 and τ_2, and which both lie on the same yield surface, i.e. $\tau_{eq} = \tau_y$, with $\tau_{eq} = \tau_{eq}^1 = \tau_{eq}^2$ and $\tau_y = \tau_y^1 = \tau_y^2$. Realising that the transfer is a linear operator, the new transferred variables τ' and τ'_y can then be computed as

$$\tau' = \chi_1\,\tau_1 + \chi_2\,\tau_2\,, \qquad (2.31)$$

$$\tau'_y = \chi_1\,\tau_y + \chi_2\,\tau_y = \tau_y\,, \qquad (2.32)$$

where χ_1 and χ_2 represent the coefficients by which the two old Gauss points influence the new Gauss point ($\chi_1 + \chi_2 = 1$). Relation (2.32) implies that the yield stress has not changed after the transfer. However, since the stress tensor is interpolated linearly and the yield surface is convex, the transferred stress will generally lie inside it, even if τ_1 and τ_2 were on it, except in the trivial case $\tau_1 = \tau_2$. Hence $\tau_{eq}(\tau') < \tau'_y$ in this situation. The graphical representation in Fig. 2.11 illustrates a transferred stress state which clearly became elastic. This not only is an inaccurate representation of the local state before remeshing and transfer, but it may also lead to poor convergence behaviour in subsequent loading increments, in which the yield surface will often be met again. In the more general case where also the yield surface is interpolated between old Gauss point yield surfaces, the transferred stress may even end up outside the transferred yield surface, which clearly also compromises the stability of subsequent equilibrium iterations.

The above inconsistency in the yield condition occurs simultaneously with the failure of the transferred stresss field to satisfy the discretised equilibrium equations. Our strategy to deal with these two difficulties consists in first removing the unbalance in the equilibrium equations and then correcting the remaining inconsistencies in the yield condition. These issues will be detailed in the next subsections.
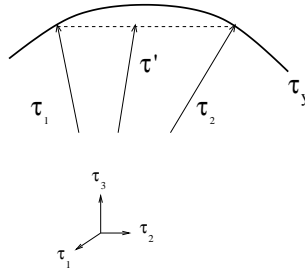
Figure 2.11 — *Influence of transfer on the stress tensor. Transferred stress states no longer lie on the yield surface.*

Equilibrium null step

The transferred and possibly corrected state generally will not satisfy the internal (discrete) equilibrium equations and may be incompatible with the traction boundary conditions. In order to preserve numerical stability, it is necessary to restore equilibrium before proceeding with a new load increment or with the opening of a new crack segment (if already embedded). This is done in a so called balancing-step, i.e. an equilibrium step in which there is no change in the external loading or boundary conditions, but a number of equilibrium iterations are made simply to retrieve an equilibrated reference state. This balancing-step eliminates the artificially introduced unbalance caused by the transfer and therefore does not represent a physical deformation process. Because of this, the constraints that apply on state variables in the constitutive equations may be relaxed in the balancing step.

If the balancing-step is considered as a material step (satisfying deformation and/or stress constraints), the convergence behaviour is relatively poor and sometimes even shows divergence. The transferred state variables, in violation of the loading-unloading conditions, then may cause stresses at integration points that alternate between an elastic and a plastic state at each iteration. To ensure convergence, this switching is prevented by assuming that all deformation in the balancing-step is elastic. This is allowed since no physical evolution process in the material takes place in the balancing-step.

Table 2.1 shows the influence of the type of null-step and the consistent recovery on the convergence rate. The computation which was used is that of the CT

test as detailed in Section 2.4. The convergence parameter that has been chosen is $\|f_{res}\|/\|f_{ext}\|$, where $f_{res} = f_{ext} - f_{int}^{(i)}$ are the unbalanced forces and $\|\cdot\|$ denotes the Euclidean norm. If all integration points are free to switch from an elastic to a plastic state, the convergence rate is slow when consistency is enforced (see column C) while divergence is observed otherwise (see column NC). On the contrary, during an elastic null-step the convergence rate is quadratic, as expected (columns NCE and CE). It can also be seen that when consistency is enforced (column CE), the unbalance in the first iteration is reduced (by a factor of approximately 8), thereby converging in fewer iterations.

The analysis performed here shows that the consistent recovery followed by an elastic balancing-step is optimal. Enforcing consistency of the transferred variables reduces errors and prevents the loss of convergence, while the elastic null-step guarantees a quadratic convergence rate. Since this null-step is an 'artificial' equilibrium step (no evolution in the material takes place), there are no physical grounds to justify e.g. an elasto-plastic switching.

Table 2.1 — *Influence of enforcing consistency and allowing for plastic deformation on the convergence behaviour in the balancing step; data obtained for CT test simulation (see Section 2.4).*

iterations	(NC)	(C)	(NCE)	(CE)
1	6.04011e+00	8.53857e-01	6.04011e+00	8.53857e-01
2	5.53544e-01	2.41680e-02	2.82171e-01	3.04375e-04
3	7.26324e-02	6.73060e-03	9.13409e-04	4.74924e-09
4	6.72483e-02	8.56056e-04	7.06020e-08	
5	1.77130e-01	1.04655e-05	3.00993e-11	
6	diverges	3.59424e-10		

(NC): Non Consistent, (C): Consistent, (NCE): Non Consistent and Elastic null-step,
(CE): Consistent and Elastic null-step.

Fig. 2.12 shows the effect of the transfer and the elastic null-step on the von Mises stresses at a crack tip. Note the good agreement between the stresses before the transfer (a), after the transfer (b), and after the equilibrium elastic null-step (c). Only very small differences can be seen, due to the stress smoothening (b) and the release of the plastic constraint (c).

During the elastic balancing step the yield surface does not change, which might lead to stresses that violate the yield condition. The mismatch between $\tau_{eq}(\tau)$ and τ_y can be resolved by either projecting the stress tensor τ on to the yield surface, or rather by scaling down the yield stress. The latter is done because projecting a tensor is not trivial. ε_p can then be consistently derived from the corrected yield stress. Finally, a fully consistent set of state variables which is in equilibrium has been recovered.
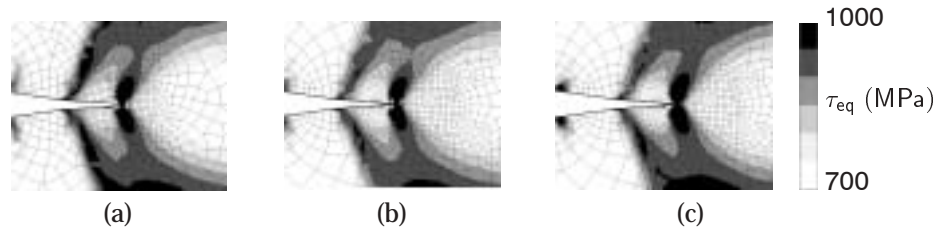
Figure 2.12 — *Qualitative representation of the transfer stages: (a) von Mises stress τ_{eq} before transfer; (b) after transfer $\tau_{eq}(\tau')$; (c) and after the elastic equilibrium null-step.*

2.3.3   Crack opening: Nodal splitting and nodal relaxation

Since there is no continuous influence of the damage on the stresses, large stress redistributions take place at the crack tip and a considerable amount of energy is released during crack propagation. Whereas for an idealised continuous crack this redistribution proceeds gradually as the crack grows, for a discretised crack finite amounts of energy are released in an incremental manner. With every new crack segment, large stresses built up at the old crack tip must suddenly vanish to comply with the new boundary conditions (see Fig. 2.13). At the same time, there is a large stress increase at the new crack tip. If not properly dealt with, these stress redistributions can have a detrimental effect on the stability of the computations. A straightforward solution is to take smaller crack segments. Yet, this increases the computational cost quite significantly and still does not guarantee convergence.
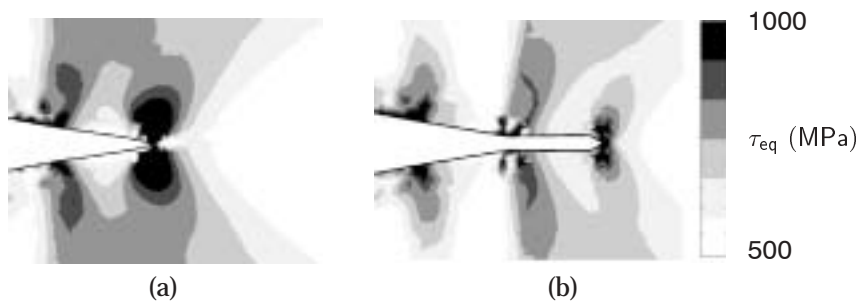
Figure 2.13 — *Stress redistributions (von Mises stress): (a) old crack tip; (b) new crack tip.*

The opening of the new crack segment, which up to this point was closed, is done by splitting and releasing the nodes along its faces. At this stage the unbalance is only due to the non-zero nodal forces acting on both sides of the new crack

segment. These nodal forces were self-equilibrating as long as the crack segment was closed, but become external forces upon nodal splitting and are no longer in equilibrium with the new boundary conditions (free surface of the new crack faces) (see Fig. 2.14). Equilibrium requires the complete removal of these forces. However, if they are removed at once, the subsequent equilibrium iterations are often found to diverge, especially for relatively coarse meshes. Note in this connection that the iterations made here cannot be kept elastic, but must be elastoplastic, because the crack opening represents a physical change. A relaxation procedure has been implemented during which these unbalanced nodal forces are removed through subincrementation if necessary. This methodology has already been applied to the opening of cracks whose path is known a priori (e.g. symmetry [43]). The use of relaxation in combination with remeshing, as applied here, is particularly useful to simulate cracks whose path is not known a priori.

To allow for the total removal of the unbalanced internal forces without having to specify the number of substeps needed, an adaptive subincrementation algorithm has been implemented which reduces the amount of unbalance that is removed at a time as necessary to guarantee convergence. Starting from the situation where the forces across the crack are completely removed, the iterative process tries to restore equilibrium. If this iteration process fails to converge, 50% of the forces is temporarily retained and the process is repeated. Upon convergence the remaining forces are removed in a second substep. In case of divergence, further substepping can take place in the fraction of the forces that is retained. This method ensures the complete removal of the residual forces in a minimum number of substeps. More importantly, it shows convergence regardless of the crack segment size. Large unbalance forces, caused by large crack segments, only require more substeps for equilibrium to be restored.

2.4 Applications

In order to assess the performance of the numerical model presented in the previous sections, a number of test case simulations have been carried out and the results are next compared with published experimental data. All examples shown are displacement-driven load cases for which plane strain elements have been used. Bi-linear 4-node isoparametric elements with selectively reduced integration have been adopted to avoid locking. For equation (2.11), a non-linear hardening law of the type

$$\tau_y \;=\; \tau_{y0} \,+\, h\,\varepsilon_p \,+\, (\tau_{y\infty} \,-\, \tau_{y0})(\,1\,-\,\exp^{-\eta\,\varepsilon_p}\,) \tag{2.33}$$

has been used.

2.4.1 Tensile test on a double notched specimen

A benchmark simulation has been performed in order to assess the robustness of the computations for different meshes and crack discretisations. Motivated by the
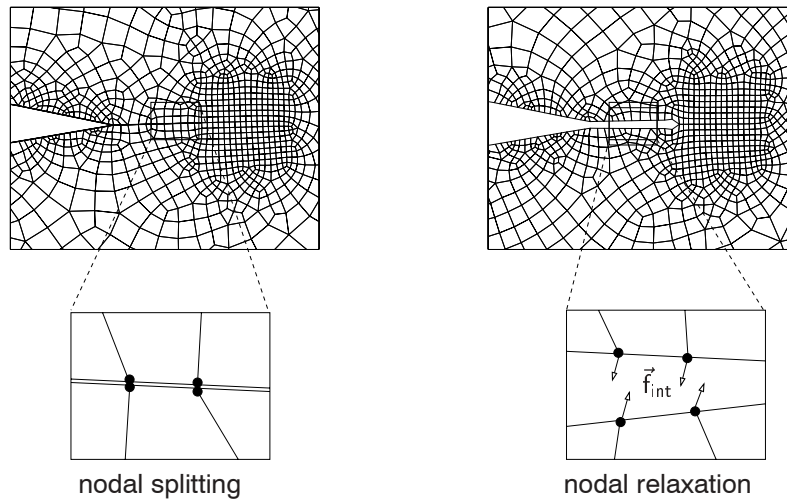
Figure 2.14 — *Opening of last crack segment: nodal splitting-nodal relaxation.*

blanking process, a problem geometry with two asymmetrically placed rounded notches is used for this purpose [28]. Vertical displacements are imposed on the top and left boundaries, while horizontal displacements have been prevented. The bottom and right boundaries remain fixed, see Fig. 2.15. The dimensions (in *mm*) are, $r_1 = 2$, $r_2 = 2.5$, $r_c = 1$, $a = 10$. The material properties have been summarised in
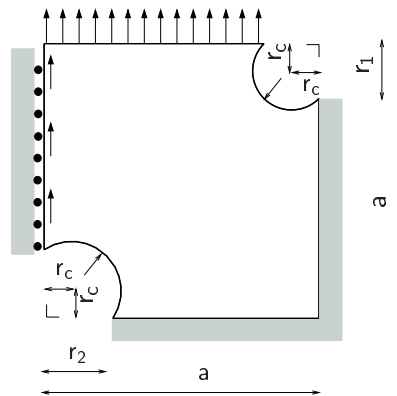
Figure 2.15 — *Tensile test on notched specimen: geometry and boundary conditions.*

Table 2.2. Linear hardening has been assumed, i.e. the parameter $\tau_{y\infty}$ is equal to τ_{y0}. The crack direction parameter α has been chosen to agree with the crack trajectories observed in blanking experiments.

Table 2.2 — *Material properties used in the tensile test geometry.*

Shear modulus G	70.3 GPa
Bulk modulus K	136.5 GPa
Initial flow stress τ_{y0}	443 MPa
Hardening parameter h	1690 MPa
Damage parameter C	1.9 -
Damage parameter A	3.0 -
Direction parameter α	0.7 -

Fig. 2.16 shows two different discretisations: (a) a coarse mesh with a large crack segment size and (b) a fine mesh with a small crack segment size. As the force-displacement curves show, there is little difference between the results obtained with the two discretisations before the onset of fracture. The only noticeable difference consists in the bumps which occur at each remeshing step, due to diffusion, and which are larger for the coarse discretisation. However, during crack propagation larger differences appear (note the big jumps in the coarse discretisation), which are the consequence of the the combined effect of large transfer errors (coarse mesh) and large geometric changes (large crack segments). The larger transfer errors result from the large stress gradients around the crack tip, which are not captured properly by a coarse discretisation. In spite of the expected quantitative differences, no computational problems arise from the coarse discretisation.

2.4.2 Compact tension test

The experiments performed by Dawicke et al. [39] on 2024T3-Al have been used as a benchmark for our model. A CT specimen was used with dimensions (in *mm*) a = 61, w = 152.4 (a/w = 0.4) and a thickness of 2.3 mm, see Fig. 2.17 (a). The hardening parameters h, η, $\tau_{y\infty}$ have been determined by fitting the experimental data reported in Ref. [39]. The material parameter α has been determined from the mixed mode simulations performed on the Arcan test shown in the next example. Table 2.4.2 summarises the parameters used in this simulation. The damage average (Eq. 2.24) is computed on a half circle of radius R $= 0.5$ mm. The crack direction has been computed at distances 0.5-1-1.5-2 mm.

The forces exerted by the two loading pins on the specimen holes have been modelled by prescribing the displacements at the top and bottom nodes of the holes respectively. Fig. 2.17 shows the geometry of the CT specimen (a), the initial (b) and the final mesh (c). Note that, in order to verify whether the proposed model correctly predicts the expected straight path, no use has been made of the symmetry of

(a)

(b)
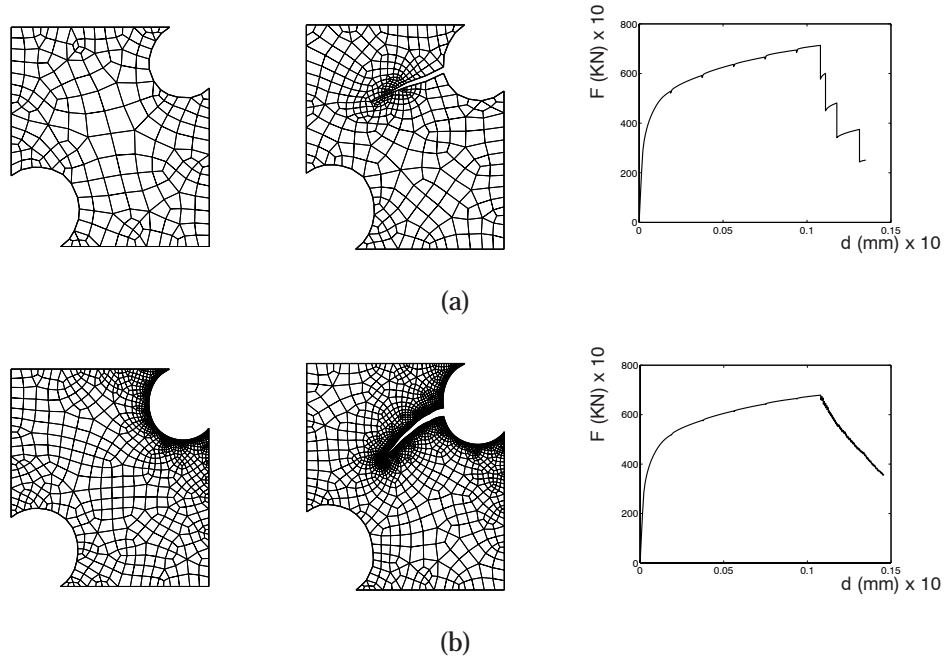
Figure 2.16 — *Robustness of the crack propagation algorithm: (a) coarse mesh with large crack segments; (b) fine mesh with small crack segments.*

Table 2.3 — *Material properties of 2024T3-Aluminium as used in the CT simulation.*

Shear modulus G	27.5 GPa
Bulk modulus K	59.5 GPa
Initial flow stress τ_{y0}	345 MPa
Hardening parameter h	127.6 MPa
Hardening parameter η	27.4 -
Hardening parameter $\tau_{y\infty}$	465 MPa
Damage parameter C	0.05 -
Damage parameter A	3 -
Direction parameter α	0.7 -

the problem. The simulation indeed leads to a nearly straight path, as can be seen from the final mesh shown in Fig. 2.17 (c).

Fig. 2.18 shows the obtained agreement between the simulated and experimental force-displacement and force-crack length curves. Since a fine mesh with a small crack segment length (1 mm) has been used, the resulting force-displacement curve is quite smooth (see Fig. 2.18 (a)).

Fig. 2.19 illustrates the evolution of the equivalent plastic strain. Initially con-
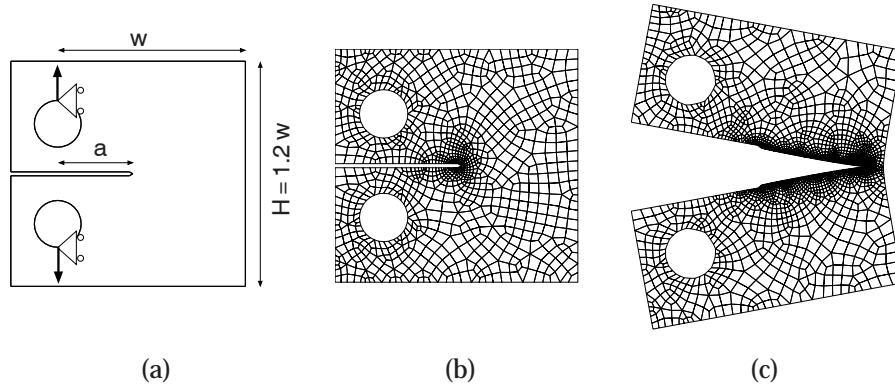
Figure 2.17 — *CT test: (a) dimensions and boundary conditions; (b) initial mesh; (c) final mesh.*
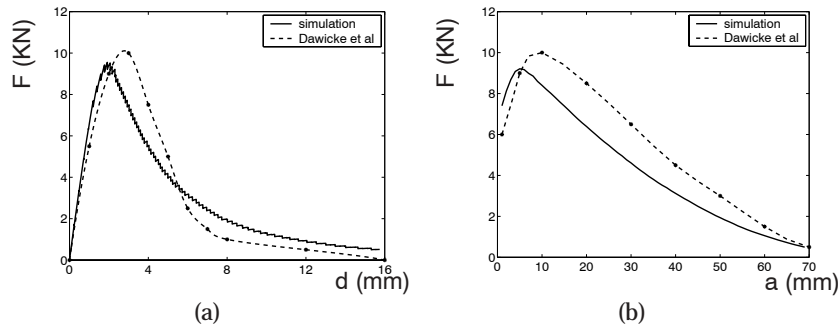
Figure 2.18 — *CT test: (a) force-displacement; (b) force-crack length.*

fined to the crack tip and holes, the plastic region advances with the crack and eventually merges with the compressive region at the right side of the specimen. A hinge is formed, around which the specimen starts to rotate (see Fig. 2.19 (c)). Note the large spread of the plastic regions around the pin holes, which is due to the poor modelling of the loading pins in the holes. However, this nonphysical plastic deformation has little effect on the force-displacement curves, which are dominated by the crack propagation and the relative rotation of the upper and lower parts of the specimen. Fig. 2.20 represents the evolution of the damage variable as given by Eq. (2.15). The shape of the damage zone roughly coincides with the plastic region under tension. Again, it is noticed that damage spreads only marginally in front of the crack tip, which would make predictions of the crack direction based on damage

only particularly troublesome.

(a)   (b)   (c)   (d)
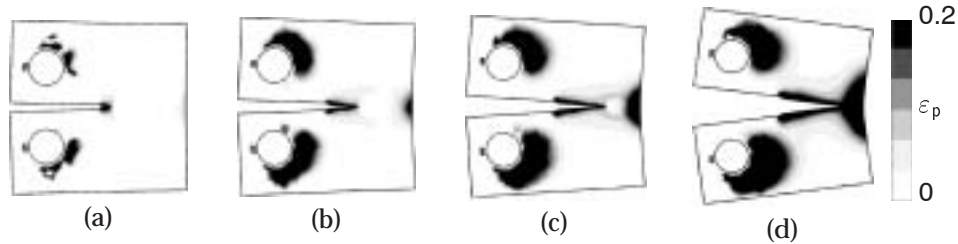
Figure 2.19 — *Evolution of the equivalent plastic strain: (a) crack 10 mm; (b) crack 30 mm; (c) crack 50 mm; (d) crack 70 mm.*

(a)   (b)   (c)   (d)
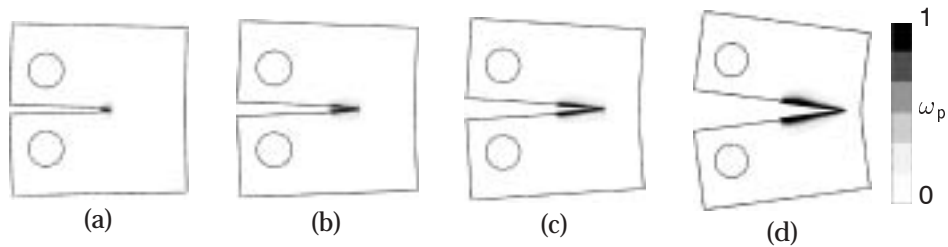
Figure 2.20 — *Evolution of Oyane's damage: (a) crack 10 mm; (b) crack 30 mm; (c) crack 50 mm; (d) crack 70 mm.*

2.4.3   Arcan test

The proposed crack direction criterion, presented in Section 2.2.3, has been validated on the basis of a comparison between simulations and the experiments performed by Amstutz et al. [3, 4] using a modified Arcan specimen. The Arcan test [7] allows by means of a special fixture the loading of a test specimen at different angles β, and thus performing mixed mode fracture experiments. Fig. 2.21 shows the geometry of the Arcan specimen and clamps used by Amstutz et al., where the main dimensions (in *mm*) have been indicated with values H = 38.1, w = 38.1, r = 15.34, l = 6.3 mm (pre-crack); the thickness of the specimen equals 2.3 mm. A plane strain assumption is made in this direction. The material and the specimen thickness are the same as in the previous example (2024T3-Al, 2.3 mm), as well as the radius R for the damage average and the crack direction parameters (Fig. 2.8).
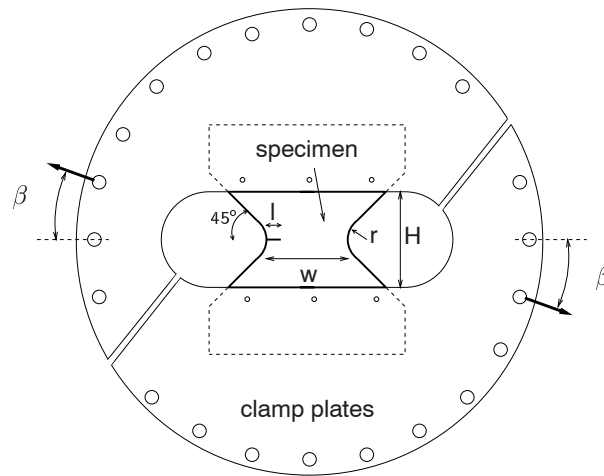
Figure 2.21 — *Sketch of Arcan setup.*

The initial mesh used in the simulation and the boundary conditions are shown in Fig. 2.22. The mesh consists of a part which models the specimen, as well as a part which represents the loading clamps. Instead of the bolts used in the experiments, the two parts are here assumed to be perfectly bonded on the bolt line. Likewise, the external radius of the loading clamps is taken equal to the radius of the loading bolts (see Fig. 2.22) and the loading force is modelled by a single nodal force at the appropriate position.

Fig. 2.23 shows the cracked meshes for different loading angles. Mode-I crack growth is predicted for $\beta = 90^o - 30^o$ (Fig. 2.23, (b) to (e)); and mode-II for $\beta = 15^o$, $\beta = 0^o$, (Fig. 2.23 (f)). Simulations and experiments agree very well, as is illustrated in Fig. 2.24, which shows the final crack paths obtained in the simulations and the experimental paths reported by Amstutz et al. [3, 4]. Except in pure mode-I ($\beta = 90^o$), mode-I crack propagation is accompanied by a pronounced positive slope, which is maximum at the onset of fracture and diminishes gradually. In mode-II, however, cracks propagate in a straight fashion, with a gentle negative slope. The transition from tensile (mode-I) to shear (mode-II) crack growth occurs at an angle β between 30° and 15°. Computations have shown that the correct description of the boundary conditions, including the loading clamps, plays an important role in the final outcome. In the simulation of mode-II crack propagation ($\beta = 0^o$, 15°), the crack faces tend to touch each other or even to penetrate. Avoiding penetration requires a self-contact algorithm which was not available in the present framework. Therefore, the simulations shown here were done without self-contact, but the penetration is eliminated in each remeshing step.

The experimental and simulated force-crack length curves have been represented
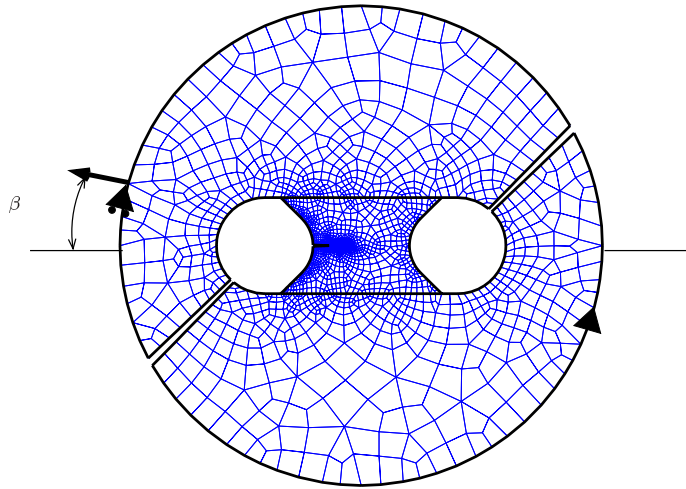
Figure 2.22 — *Initial mesh and boundary conditions for the Arcan simulations.*

in Fig. 2.25, for $\beta = 90^o$, 45°, 0°. The agreement is excellent for $\beta = 45^o$, but there are still discrepancies in the other cases, which might require a better tuning of the material properties.

Fig. 2.26 and Fig. 2.27 illustrate the evolution of damage under tensile ($\beta = 90^o$) and shear loading ($\beta = 15^o$). Damage growth and crack propagation occur simultaneously. Unlike in shear, in tension damage hardly spreads in front of the crack tip.

2.5   Conclusions

In this chapter, a finite element tool for the modelling of quasi-static ductile crack propagation has been developed, with special attention to the numerical stability of the algorithmic steps which must be taken in crack growth simulations.

In order to limit the complexity of the modelling, an uncoupled damage approach has been used. As a result, localisation and mesh sensitivity due to softening are not an issue and no regularisation method is needed. The damage merely serves as a crack initiation and propagation criterion. The main drawback of this approach is that the local material degradation process from which the crack originates is not captured in detail, resulting in an overprediction of the stresses in the vicinity of the crack tip. Use of these types of models is justified provided that the fracture process zone and length scale effects are small.

Numerically, full remeshing enables to trace the geometry of a discretised crack and avoids large element distortions. This technique is however not exempt from

$\beta = 90°$ (mode-I) $\beta = 75°$

$\beta = 60°$ $\beta = 45°$

$\beta = 30°$ $\beta = 15°$

$\beta = 0°$ (mode-II)
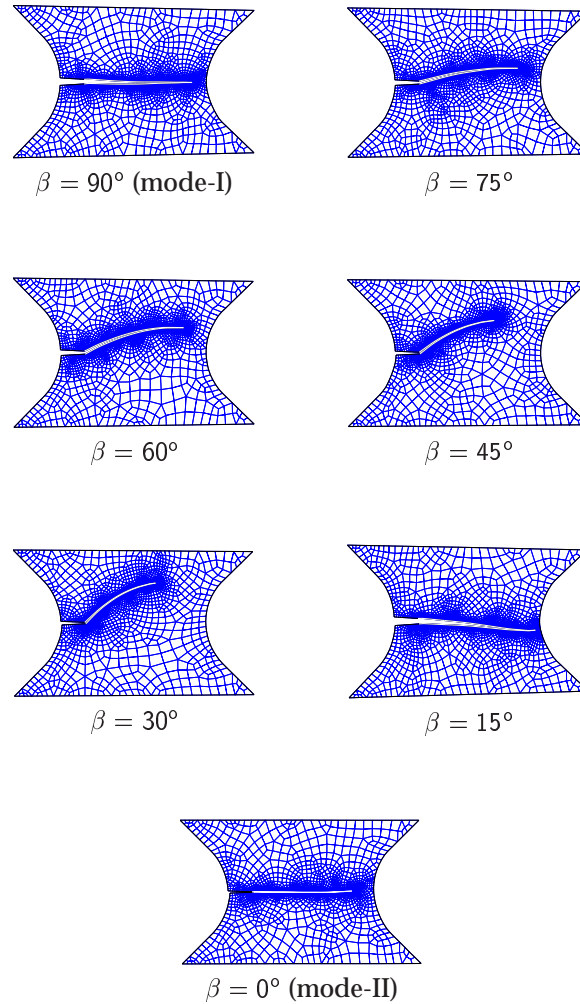
Figure 2.23 — *Finite element mesh and crack trajectory for different loading angles.*

numerical difficulties. Transfer errors together with large stress redistributions during the crack propagation can have a detrimental effect on the stability of the computations. It has been demonstrated that by separating and resolving these two instability sources, the robustness of the crack propagation algorithm can be improved considerably, enabling it to deal with coarse meshes and coarse crack discretisations. Transfer errors are addressed by restoring a consistent set of variables, followed by
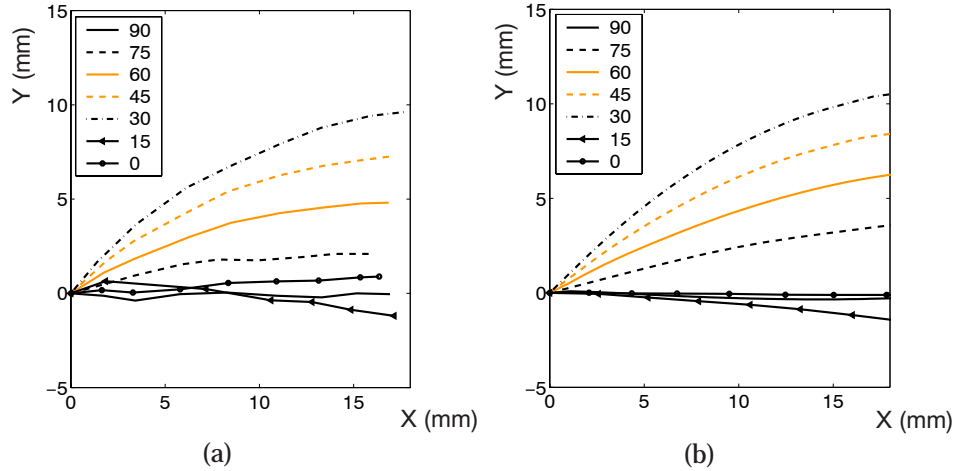
Figure 2.24 — *Crack paths: (a) experiments by Amstutz et al. [3, 4]; (b) simulations.*

an elastic equilibrium step and the recovery of the loading-unloading conditions. Secondly, a relaxation step is performed, in which the crack opens gradually.

It has been argued that a crack direction criterion based on the damage field around the crack tip does not agree with available experiments. Therefore, an additional crack direction criterion has been proposed, which has the advantage of being applicable to mixed-mode loading conditions, still capturing the experimentally observed tensile to shear crack growth transition in ductile fracture.

A number of simulations have been carried out, that helped to illustrate the main issues dealt with in this chapter, i.e. robustness of the computations, numerical modelling of discrete fracture, ductile damage, crack direction, etc.
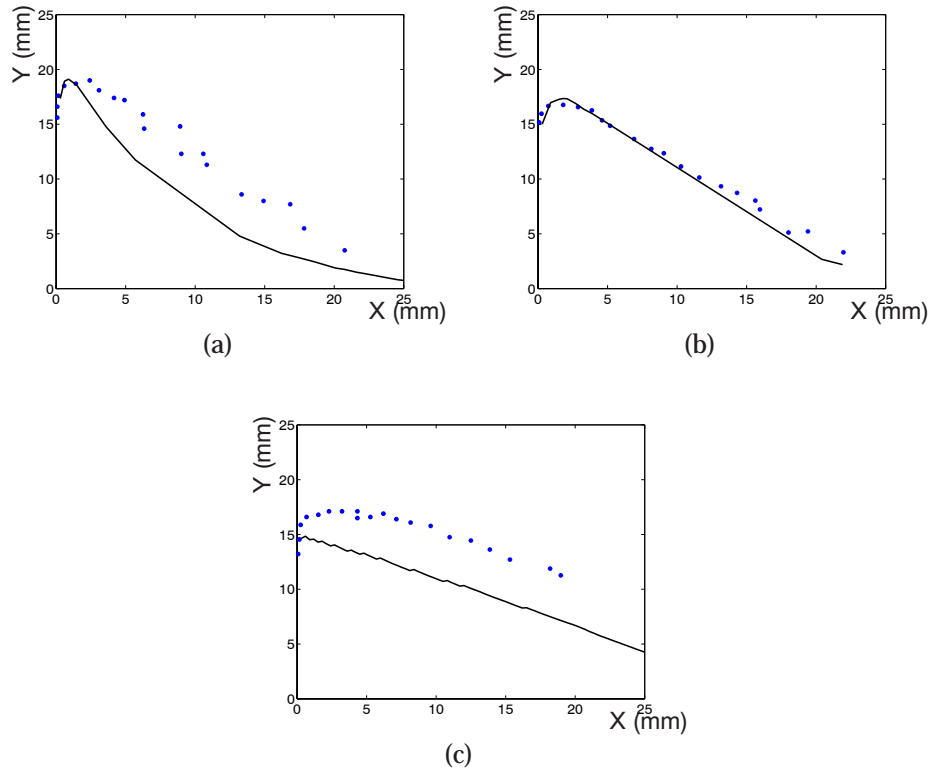
Figure 2.25 — *Force-crack length, experiments [3, 4] and simulations; (a) $\beta = 90^{\circ}$ (mode-I), (b) $\beta = 45^{\circ}$, (c) $\beta = 0^{\circ}$ (mode-II).*
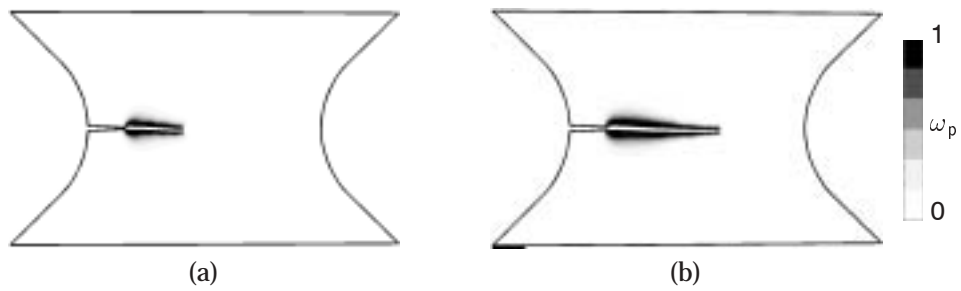
Figure 2.26 — *Tensile loading ($\beta = 90^{\circ}$). Damage evolution: (a) crack 90 mm, (b) crack 180 mm.*
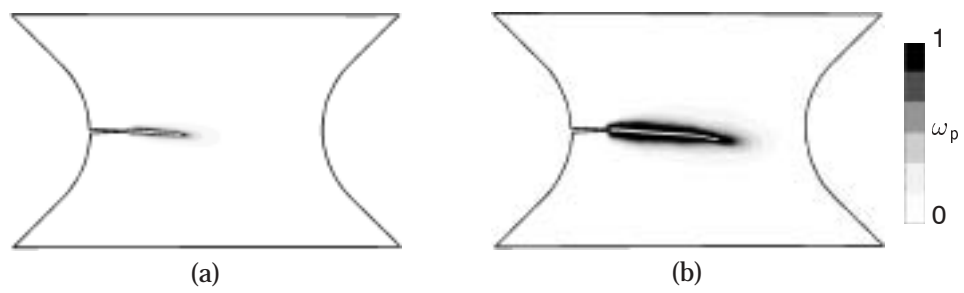
Figure 2.27 — *Shear loading ($\beta = 15°$). Damage evolution: (a) crack 90 mm, (b) crack 180 mm.*

<div align="right">

Chapter 3

</div>

<div align="right">

Discrete modelling of ductile fracture driven by nonlocal softening plasticity [2]

</div>

Abstract: A combined approach towards ductile damage and fracture is presented, in the sense that a continuous material degradation is coupled with a discrete crack description, for large deformations. Material degradation is modelled by a gradient enhanced damage-hyperelastoplasticity model. It is assumed that failure occurs due to plastic straining, which is particularly relevant for shear dominated problems, where the effect of the hydrostatic stress in triggering failure is less important. The gradient enhancement eliminates pathological localisation effects which would normally result from the damage influence. Discrete cracks appear in the final stage of local material failure, when the damage has become critical. The rate and the direction of crack propagation depend on the evolution of the damage field variable, which in turn depends on the type of loading. In a large strain finite element framework, remeshing allows to incorporate the changing crack geometry and prevents severe element distortion. Attention is focused on the robustness of the computations, where the transfer of variables, which is needed after each remeshing plays a crucial role. Numerical examples are shown and comparisons are made with published experimental results.

3.1 Introduction

Ductile fracture is governed by microscopic processes such as void nucleation, void growth and coalescence, which ultimately lead to crack initiation and propagation. Macroscopically, these processes become manifest in overall material softening, which leads to strain localisation and eventually to the formation of discrete cracks. At this macroscopic scale, traditionally two different approaches have been followed in the modelling of fracture: continuous and discontinuous (Fig. 2.1).

---

[2]This chapter is based on [85].

Continuous approaches describe the degradation processes which lead to the formation of new crack surface, either in a phenomenological way, as in continuum damage mechanics [65, 74], or in a micromechanical setting [56, 81, 89, 108, 130]. One or several variables – often called damage variables – are used to capture the essential features of the damage process. These variables generally have a weakening effect on the yield stress (and sometimes on the elastic properties) and therefore result in a strain-softening response.

Regularisation techniques must be used to overcome the pathological localisation and, in a finite element context, mesh dependence associated with softening materials, resulting in gradient models, integral-type nonlocal models, rate-dependent and micro-polar models (see for instance [41] for a review). These enhanced formulations supply the continuum model with an internal length scale, for which partial physical interpretations have been suggested (e.g. average size of or distance between the largest inhomogeneities, voids, distributed cracks, etc.) and can be well adapted to a (numerical) finite strain setting [50]. Gradient models are especially interesting to model ductile failure, since they can account for nonlocal micro-void interactions [106]. Gradient models can be classified into implicit and explicit models, depending on whether the nonlocal variable is an explicit functional of its local counterpart or not [11, 99]. Explicit gradient models were first applied in the context of elasticity and plasticity to account for length scale effects (see [49] for an overview) and were later applied to damage and softening elastoplasticity [35, 42]. Implicit gradient models are strongly nonlocal, like integral models [14, 69, 131], with the advantage that they are simpler to implement and more efficient. They have been used in brittle [97]; and ductile damage, for small [45] and large strains [8, 53].

A *discontinuous* approach is typically used in fracture mechanics, where the focus is on modelling discrete cracks. The mechanical properties of the material next to the crack are assumed to remain intact, i.e. there is no material softening. Additional assumptions are made for initiation and propagation criteria (e.g. critical energy release rate, crack tip opening displacement) as well as for crack growth direction criteria (e.g. maximum circumferential stress). In a finite element framework the proper modelling of discrete cracks of any arbitrary geometry requires either remeshing [133] or embedding techniques such as XFEM [15], which allow to insert discontinuities in an existing mesh. Remeshing adapts the mesh topology to the crack geometry, whereas XFEM (based on the Partition of Unity concept) enriches the interpolation functions with displacement jumps. Most techniques to model cracks are either unable to properly account for the displacement jump across the crack, e.g. smeared cracks [13], or simplify the fracture process zone to a zero-width band constrained to a predefined crack path, e.g. cohesive zone [12, 44].

To model the entire fracture process, from material degradation, via crack initiation, to crack propagation, both continuous softening and discontinuous models should ideally be used in a *combined continuous-discontinuous* model. The transition between the continuous and discontinuous models is made at complete, local failure of the continuous material (see Fig. 2.1). The precise location of crack initiation is therefore the outcome of the damage evolution process and no initial crack needs

to be defined. The interplay between the discrete crack(s) and the surrounding degrading material governs the crack growth behaviour and cracks can be seen as the limit result of strain localisation. A finite sized process zone develops in a natural fashion ahead of the crack and the influence of initially present damage can be included in a straightforward manner. Since the continuous part of the description will generally exhibit strain softening, a regularisation method must be used. A few attempts have been made to model cracks using gradient damage, either by employing a variable internal length parameter [52] or by the removal of failed elements [96], but these methods respectively rely on a continuum description and result in a crude representation of the crack. More recently, XFEM has been applied to model discrete cracks in a regularised softening continuum [121, 136]. Yet, XFEM loses part of its appeal in a large strain framework, since remeshing is nevertheless needed to avoid large element distortions.

The main motivation of this chapter is to provide a combined continuous-discontinuous framework for the modelling of ductile fracture. Ductile damage is modelled by a strongly nonlocal gradient hyperelastoplasticity model [53], the main features of which are that: (i) it accounts for long range microstructural interactions (strongly nonlocal); (ii) it does not suffer from pathological mesh dependence; (iii) it can deal with large strains and rotations; (iv) and does converge to a discrete crack upon complete failure. It is emphasised that the damage field which is used to model the plastic degradation process influences the local yield stress and thus causes strain softening. This is unlike frameworks which use the damage field merely as an indicator for fracture, e.g. Chapter 2, [28, 82]. Upon material failure, a discrete crack is introduced, for which a new mesh is created. Remeshing is simultaneously used to eliminate large element distortions. The combined approach proposed in this chapter is intended to be used whenever the size of the fracture process zone cannot be neglected and macroscopic cracks are initiated in locations which are not known a priori.

The structure of this chapter is as follows. In Section 3.2 the material model is described. The numerical aspects are discussed in Section 3.3, where the emphasis lies on the robustness of the computations and in particular the correct treatment of transfer errors and the creation of new crack surface, which are crucial for the stability of the computations. In Section 3.4 a few applications are shown.

3.2 Constitutive modelling

3.2.1 Continuum model

Ductile damage is modelled here by means of a gradient enhanced hyperelastoplastic model proposed by Geers et al. [53], which extends an earlier small strain model [45] to a large strain setting. In this model, isotropic damage is introduced as a multiplicative degradation of the yield stress. It is based on the J_2 hyperelastoplasticity framework proposed by Simo and Miehe [119]. For the sake of completeness, the

governing model equations are briefly discussed. The interested reader is referred to Ref. [53] for a detailed description.

The deformation gradient F is split into an elastic part F_e and a plastic part F_p according to

$$F = F_e \cdot F_p .$$ (3.1)

The hyperelastic relationship between stress and elastic deformation reads

$$\tau = \frac{K}{2} \left(J^2 - 1 \right) I + G \, \bar{b}_e^d ,$$ (3.2)

where τ is the Kirchhoff stress tensor, J is the volume change ratio ($J = \det(F)$) and $\bar{b}_e^d$ is the deviatoric part of the isochoric elastic left Cauchy-Green tensor. K and G are the bulk modulus and the shear modulus respectively. Plastic flow is assumed to be isochoric. The flow rule is given by

$$\left[\overset{\triangledown}{b}_e \right]^d = -3 \, \dot{\varepsilon}_p \, \frac{\tau^d}{\tau_{eq}} ,$$ (3.3)

where $\overset{\triangledown}{b}_e$ is the objective Lie derivative of the elastic left Cauchy-Green tensor and the superscript $(\cdot)^d$ denotes the deviatoric part of a second order tensor; $\dot{\varepsilon}_p$ is the effective plastic strain rate

$$\dot{\varepsilon}_p = \sqrt{\frac{1}{6} \left[\overset{\triangledown}{b}_e \right]^d : \left[\overset{\triangledown}{b}_e \right]^d} .$$ (3.4)

and τ_{eq} is the equivalent von Mises stress

$$\tau_{eq} = \sqrt{\frac{3}{2} \tau^d : \tau^d} .$$ (3.5)

An isotropic ductile damage variable ω_p ($0 \leq \omega_p \leq 1$) is introduced as a softening factor of the virgin (effective) strain-hardening curve $\hat{\tau}_y(\varepsilon_p)$, leading to a combined hardening-softening yield stress which reads

$$\tau_y = (1 - \omega_p) \, \hat{\tau}_y ,$$ (3.6)

or in rate form

$$\dot{\tau}_y = (1 - \omega_p) \dot{\hat{\tau}}_y - \hat{\tau}_y \dot{\omega}_p .$$ (3.7)

In the computations of Section 3.4, linear hardening has been assumed for the undamaged material, i.e. $\dot{\hat{\tau}}_y = h \dot{\varepsilon}_p$, with h a positive constant.

Plastic flow fulfils the standard Kuhn-Tucker loading-unloading conditions

$$\dot{\varepsilon}_p \geq 0 \,, \qquad \phi \leq 0 \,, \qquad \dot{\varepsilon}_p \phi = 0 \,. \tag{3.8}$$

where the yield function is defined as $\phi \equiv \tau_{eq} - \tau_y$.

The damage variable ω_p is defined such that $\omega_p = 0$ represents the undamaged state, whereas $\omega_p = 1$ stands for complete failure, at which point the yield surface collapses to a singular point of zero yield stress. Upon loading, the material may undergo four different stages: i) elastic behaviour, ii) strain hardening, iii) strain softening, iv) failure and formation of a discrete crack (see Fig. 3.1, in which these stages are indicated by E, H, S and D). This is a substantial difference with elastoplastic-fracture models, where the transition form strain-hardening to a discrete crack is introduced in an uncoupled, discrete manner (Chapter 2, [28, 82]), without prior softening. The final hardening-softening response of the model is the combined effect of the usual hardening of the material and the softening influence of damage.
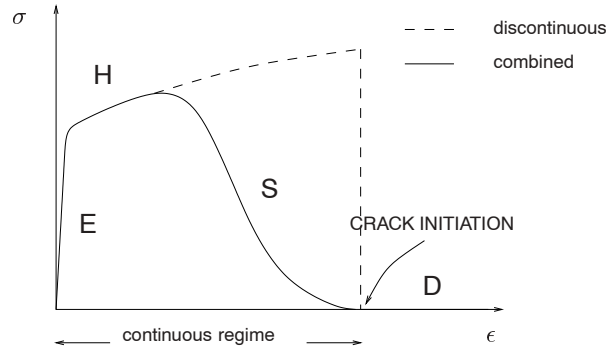
Figure 3.1 — *Different stages of behaviour (stress-strain). (E) elastic, (H) hardening, (S) softening and (D) discrete crack.*

Damage evolution is described here by a phenomenological law, driven by a history variable κ, which in general depends on some equivalent (scalar) measure of stress or strain. In rate form, the damage evolution equation reads

$$\dot{\omega}_p = h_\omega(\omega_p)\, \dot{\kappa} \,. \tag{3.9}$$

In the applications section of this chapter (Section 3.4), a nonlinear damage evolution law has been used (see Fig. 3.2), which reads:

$$h_\omega(\omega_p) = \frac{3}{\tanh(3)(\kappa_c - \kappa_i)} \left(1 - \tanh^2(3)(2\,\omega_p - 1)^2\right) \,. \tag{3.10}$$

Eq. (3.10) results in a slow initial and final damage growth, which can be computationally more robust, since it does not show any discontinuities in the damage growth (Fig. 3.2).
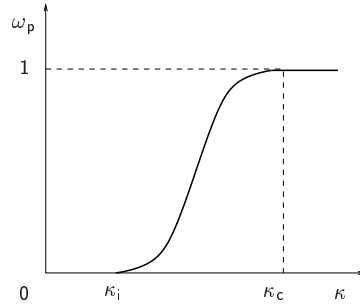
Figure 3.2 — *Nonlinear damage evolution law.*

To avoid pathological localisation effects due to material softening, the damage driving variable κ is computed from a nonlocal variable $\bar{z}$ via a separate set of Kuhn-Tucker loading-unloading conditions

$$\dot{\kappa} \geq 0, \qquad \bar{z} - \kappa \leq 0, \qquad \dot{\kappa}\,(\bar{z} - \kappa) = 0 \,, \tag{3.11}$$

and an initial value $\kappa = \kappa_i$. The nonlocal variable $\bar{z}$ is obtained from the local variable z by solving a Helmholtz type Partial Differential Equation (PDE)

$$\bar{z} - \ell^2 \, \nabla^2 \bar{z} \;=\; z \,. \tag{3.12}$$

In this equation ℓ is the internal length parameter, which –indirectly– sets the width of the localisation band. The physical interpretation of ℓ can be related to void interactions.

We assume that the local variable is equal the equivalent plastic strain:

$$z \;=\; \varepsilon_p \,. \tag{3.13}$$

This is a reasonable assumption for problems in which damage growth is mainly driven by shear strains. For problems with a high stress triaxiality, an influence of the hydrostatic stress may be expected, for which the present formulation can be extended (see [83]). Here, however, our attention will be focused on the first class of problems.

It has been demonstrated in Ref. [99] that the above implicit definition of $\bar{z}$ is truly nonlocal, in the sense that the behaviour at a point can be written as a weighted average over its neighbourhood. This is an important requirement when modelling cracks (see Peerlings et al. [100]). Unlike nonlocal models of the integral type, however, the use of Eq. (3.12) does not lead to integro-differential equations, but simply to an additional elliptic PDE which must be solved simultaneously with the equilibrium equation.

The second order PDE (3.12) is complemented by the Neumann boundary condition

$$\vec{\nabla}\bar{z} \cdot \vec{n} \ = \ 0 \tag{3.14}$$

on the boundary Γ of the current domain, including the generated crack faces; $\vec{n}$ is the normal to Γ. Both governing PDEs, i.e. the equilibrium equation

$$\vec{\nabla} \cdot \boldsymbol{\sigma} \ = \ \vec{0} \tag{3.15}$$

and the additional nonlocality equation (3.12), are expressed with respect to the current (Eulerian) configuration. This is more convenient than a material description in view of the required remeshing and transfer, as will be seen later in this chapter.

3.2.2 Crack modelling

The material softening which is associated with the damage modelling as discussed in the previous section results in local material failure in a natural way. At some stage of the damage process (when $\omega_p = \omega_{crit} = 1$) the degraded yield stress τ_y vanishes and the material cannot sustain stress anymore. At this point either a crack is initiated or an existing crack extends. From this moment on the maximum damage will generally occur near the tip of this crack and therefore lead to growth of the crack when it becomes critical (i.e. equal to one). Crack growth thus is the natural consequence of the degrading constitutive response of the material and hence no separate criteria are needed to determine the direction and the rate of crack growth. This integrated approach towards damage and fracture reflects more closely the underlying physical process of ductile fracture (i.e. initiation, growth and coalescence of voids and microcracks) compared to e.g. a fracture mechanics description. An essential requirement, however, is an accurate model for the damage process upon arbitrary loading paths.

3.3 Aspects of the finite element implementation

The finite element implementation of the nonlocal damage-plasticity model used here has been described in detail by Geers et al. [53].

The governing PDEs of the continuum problem, the equilibrium equation (3.15) and the nonlocal averaging equation (3.12), are cast in a weak form and discretised by finite element shape functions. Note that these equations are coupled and must thus be solved simultaneously.

The numerical implementation presented by Geers et al. [53] uses an Updated Lagrangian description. Stresses are updated by a radial return mapping, based on an implicit backward-Euler rule. A consistent algorithmic tangent operator is obtained by linearisation of the discrete time equations. The linear system is solved repeatedly within a standard Newton-Raphson procedure until convergence. Upon

convergence the time (and loads) can be incremented and the iterative procedure repeats itself. For details on the algorithms used, see Reference [53]. Here we detail only aspects of the present implementation which are not treated in [53], i.e. the integration of the damage evolution law and hardening relation (Section 3.3.1), difference arising in the tangents (Section 3.3.2), the treatment of crack initiation and crack propagation (Section 3.3.3) as well as remeshing and state variable transfer (Section 3.3.4).

3.3.1   Integration of damage evolution and stress update

Unlike in Ref. [53], the evolution of the yield stress τ_y and the damage variable ω_p are here written in a rate form. This form of the evolution equations is more convenient from a numerical perspective, as will be explained in Section 3.3.4.

A backward Euler integration rule is employed for the integration of the damage evolution law Eq. (3.9):

$$\omega_p \ = \ \omega_p^t \ + h_\omega(\omega_p) \, \Delta\kappa \ , \tag{3.16}$$

where ω_p denotes the new damage variable at the end of the present time increment and ω_p^t the known value at the beginning of the increment. The value of ω_p given by this rule must obviously be limited to $\omega_p = 1$, preventing it to exceed this critical level. Note that Eq. (3.16) must be solved iteratively (at integration point level), for example by a Newton-Raphson algorithm.

The rate form of the combined hardening-softening evolution law, Eq. (3.7), is also integrated using a Backward Euler rule, yielding

$$\tau_y \ = \ \tau_y^t + (1 \, - \, \omega_p) \, h \, \Delta\varepsilon_p \, - \, \hat{\tau}_y \, \Delta\omega_p \ . \tag{3.17}$$

Upon elimination of $\hat{\tau}_y$, this expression (3.17) can be rewritten as

$$\tau_y \ = \ \tau_y^t \frac{(1 \, - \, \omega_p)}{(1 \, - \, \omega_p^t)} \ + \ \frac{(1 \, - \, \omega_p)^2}{(1 \, - \, \omega_p^t)} \, h \, \Delta\varepsilon_p \ . \tag{3.18}$$

Enforcing the consistency condition now provides the increment of the effective plastic strain $\Delta\varepsilon_p = \Delta z$ according to the radial return (see [53])

$$\tau_y \ + \ 3 \, G \, J^{-2/3} \Delta\varepsilon_p \ = \ {}^\star\tau_{eq} \ , \tag{3.19}$$

where ${}^\star\tau_{eq}$ is the equivalent von-Mises stress corresponding to the trial Kirchhoff stress tensor ${}^\star\tau$, for which the incremental deformation is entirely elastic. Substitution of Eq. (3.18) in Eq. (3.19) and reordering yields

$$\Delta\varepsilon_p \ = \ \frac{{}^\star\phi}{\frac{(1 \, - \, \omega_p)^2}{(1 \, - \, \omega_p^t)} \, h \, + \, 3 \, G \, J^{-2/3}} \ , \tag{3.20}$$

where the trial value of the yield function $^\star\phi$ is defined as

$$^\star\phi \;=\; ^\star\tau_{eq} \;-\; \tau_y^t \,\frac{(1-\omega_p)}{(1-\omega_p^t)}\;.\tag{3.21}$$

To prevent unphysical hardening in the post-failure regime, i.e. when ω_p reaches one (to be detected at a value close to one, e.g. $\omega_{crit} = 0.99$, in order to prevent a poorly-conditioned stiffness matrix), the yield stress is no longer updated, thus $\tau_y = \tau_y^t$. In this regime the material flows in an ideally plastic manner at a constant, negligible flow stress. This means that

$$\Delta\varepsilon_p \;=\; \frac{^\star\phi}{3\,G\,J^{-2/3}}\;.\tag{3.22}$$

Furthermore, the local damage driving variable is no longer updated, i.e. $z = z^t$, and hence differs from ε_p, which still can increase. As a result, the convergence of the solution is not affected by the large variations of ε_p which may occur during this postfailure regime. A nice feature of the radial-return algorithm used for the stress updated is that the return projection always leads to a solution on the updated yield surface, even close to failure when the yield surface is small.

3.3.2 Consistent tangent operators.

The tangent operators used in the global Newton-Raphson iterations differ somewhat of those obtained in [53] as a consequence of the rate form of the hardening law and the damage evolution law. The modifications are reported below.

The variation of the damage variable (3.16) reads

$$\delta\omega_p \;=\; \frac{\partial h_\omega}{\partial\omega_p}\,\delta\omega_p\,\Delta\kappa \;+\; h_\omega\,\frac{\partial\kappa}{\partial\bar{z}}\,\delta\bar{z}\;,\tag{3.23}$$

or, after rearranging,

$$\delta\omega_p \;=\; c_\omega\,\delta\bar{z} \quad\text{with}\quad c_\omega \;=\; \frac{h_\omega\,\frac{\partial\kappa}{\partial\bar{z}}}{1 - \frac{\partial h_\omega}{\partial\omega_p}\,\Delta\kappa}\;.\tag{3.24}$$

The stress tensor has to be linearised in terms of the displacement variation $\delta\vec{u}$ and the variation of the nonlocal field $\delta\bar{z}$. The equation which relates the variation of stress $\delta\tau$ to $\delta\vec{u}$ and $\delta\bar{z}$, given in [53], is retained and reads

$$\delta\tau \;=\; {}^4\mathbf{C}_{ep} : \mathbf{L}_\delta^T - c_5\,{}^\star\tau^d\,\delta\bar{z}\;,\tag{3.25}$$

where $\mathbf{L}_\delta^T = \left(\vec{\nabla}\delta\vec{x}\right)$. However, the constants c_5 and c_1 have to be reformulated as

$$
\begin{aligned}
c_5 &\;=\; \frac{\tau_y^t + 2\,h\,\Delta\varepsilon_p(1-\omega_p)}{c_1\,(1-\omega_p^t)\,{}^\star\tau_{eq}}\,c_\omega \\[2mm]
c_1 &\;=\; 3 + \frac{(1-\omega_p)^2}{(1-\omega_p^t)}\,\frac{h\,J^{2/3}}{G}
\end{aligned}
\tag{3.26}
$$

with c_ω given by Eq. 3.24. The variation of the local variable z is given by [53]

$$\delta z \,=\, \boldsymbol{H} : \boldsymbol{L}_\delta^T \,+\, c_6 \delta \bar{z}\,, \tag{3.27}$$

with c_6 computed using c_5 (3.26) as indicated in [53]. Upon insertion of definitions (3.25) and (3.27), the algorithm described in Ref. [53] can also be used for the present modelling.

3.3.3   Prediction of crack initiation and propagation

The initiation and propagation of cracks is evaluated at the end of every time increment. In order to capture the exact moment when cracks initiate, the loading steps should not be too large. In practice, cracks usually initiate at the domain boundary. For this reason, the trigger for crack initiation is based on the critical nature of the damage values at the boundary nodes, which are obtained by extrapolation from the Gauss points. When the nodal damage value ω_p becomes larger than the critical value ω_{crit}, a crack is inserted in the geometry of the problem and the new domain is fully remeshed. Crack propagation is treated likewise, i.e. a new crack segment is added when the existing crack tip damage value reaches ω_{crit}. This initiation-propagation method is quite reliable, because the damage gradients in the vicinity of the crack tip tend to be rather mild for the problems of interest.

The crack direction, defined by the angle Θ_{dir}, is given by the direction of the maximum damage in front of the crack tip. Numerically Θ_{dir} is computed as the median of the maximum angles Θ_i at different distances d_i from the crack tip, obtained by evaluating ω_p at a number of discrete sample points (see Chapter 2, [28, 82]). The same remarks made in Section 2.3 about the distances d_i apply here.
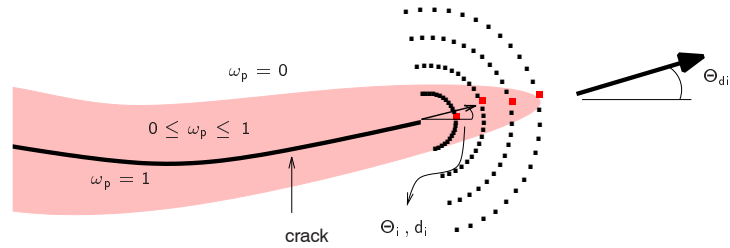
Figure 3.3 — *Crack direction algorithm.*

This method ensures that the crack is extended in the direction which is most affected by damage. On the other hand, it avoids abrupt changes in the crack orientation due to local (numerical) variations.

It should be emphasised that, contrary to what happens for elastoplastic models without a damage influence, stresses have already been reduced to almost zero at the crack tip and no large stress redistributions are therefore required upon crack growth. This does not imply, however, that the formation of a discrete crack can be neglected altogether, as is done in continuous approaches to fracture. Not introducing a crack when $\omega_p = \omega_{crit}$ leads to excessive straining, since the material across the damage zone remains kinematically connected (at almost zero stress levels), and consequently to an unrealistic lateral extension of the damage field. Whereas this was already noted and considered to be undesirable for small strains [52], it is even more troublesome for large strains, where large element distortions may result in poor convergence. This is illustrated in Fig. 3.4, which shows a benchmark problem on a double-notched plain strain specimen, to be discussed later in Section 3.4.1, where crack growth has been prevented. Fig. 3.4 (a) shows the state where a crack would normally be initiated. By preventing the crack to appear, a plateau with damage ω_{crit} and a very low stress level develops, leading to the complete collapse of the notch boundaries, see Fig. 3.4 (b).

(a)   (b)
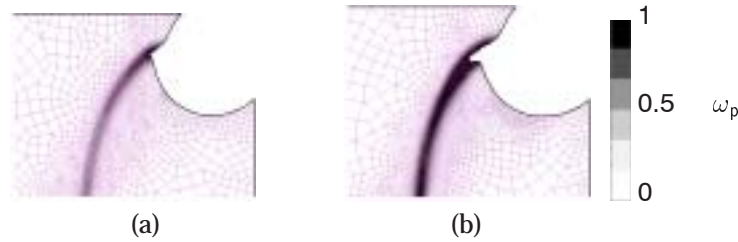
Figure 3.4 — *Extensive damage development and geometrical distortion when crack growth is prevented (continuous approach).*

3.3.4   Robust crack propagation algorithm

At each increment of crack growth, which has a fixed size, a new mesh is generated. The history dependence of the constitutive model requires information on the deformation and damage history of the material to be transferred to the new mesh before the simulation can continue. At this point the robustness of the simulation may be compromised by two factors: (i) inaccuracies and inconsistencies due to the transfer of state variables and (ii) unbalance due to the creation of new free surface and the resulting change of boundary conditions (vanishing surface tractions). If no special measures are taken, these disturbances occur at exactly the same time in the computation. As a consequence, computations easily break down, even for small crack increments and fine meshes. A similar lack of numerical stability was observed for

the uncoupled damage approach which was followed in (Chapter 2, [82]). There, it was effectively removed by uncoupling the two sources of unbalance -transfer and crack growth- while dealing with them separately. It should be mentioned that the present, fully coupled, damage framework is less sensitive to these sources of unbalance during the crack opening phase, because stresses across the crack have already been relaxed due to the damage influence. As a result, the stress redistributions which occur when a new crack increment is inserted are much smaller compared to an uncoupled approach. Nevertheless, the strategy proposed in Chapter 2 [82] is adopted here as well, since it ensures a high level of robustness of the computations. The individual elements of the resulting algorithm are explained in detail below.

Remeshing

Full remeshing is done to accommodate cracks with arbitrary paths in a finite element mesh, and to simultaneously eliminate large element distortions. Although in principle only the region adjacent to the crack tip needs to be remeshed (local remeshing), in a large strain framework the use of full remeshing keeps the mesh in an overall better shape, resulting in a better convergence rate and higher accuracy. However, too frequent remeshing also leads to a loss of accuracy due to transfer errors. Quadrilateral elements are used, which unlike triangle elements perform well under nearly isochoric conditions (e.g. in fully developed plasticity). A powerful standard quadrilateral mesher is employed, which is capable to deal with complex domains that may result from the presence of cracks [30]. The mesher also allows to define regions with a required higher element density, e.g. at the crack tip.

The domain which is to be meshed is defined by the boundary segments of the existing mesh and the newly predicted crack segment. A mesh which conforms to the newly introduced crack segment is created, but the faces of the new crack segment initially remain connected. This ensures a proper transfer of state variables prior to the update of the geometry of the problem itself (i.e. opening of the new crack segment; see also Chapter 2 [82]).

Transfer of state variables

Since the material model at hand (gradient enhanced hyperelastoplasticity) is history dependent, state variables must be transferred from the old to the new mesh. Most of these variables are available at the Gauss points of the previous mesh, which have to be mapped to the Gauss points of the newly created mesh. The transfer operator adopted has been described by Perić et al. ([101], Section 3.1). It uses subsequent interpolation and extrapolation operations to estimate the values of the relevant fields in the new Gauss points (see also Chapter 2 [82]).

Apart from Gauss-point data, data stored at the nodes of the finite element mesh generally need to be transferred as well. In the present situation, this would imply the transfer of the displacements and the nonlocal variable $\bar{z}$. However, transfer of

the displacements is not necessary in the present implementation because an updated Lagrangian formulation is used. This means that remeshing is done in the deformed configuration and only the incremental nodal displacements with respect to this configuration, $\Delta \underset{\sim}{u}$, are relevant for the sequel of the computations. These incremental displacements are – by definition – equal to zero in the remeshed state and thus do not need to be transferred, see also Chapter 2 [82].

Transfer of the nonlocal nodal variables $\underline{z}$ can also be avoided by reconstructing them from the transferred local variables z' [1] in the Gauss points, by solving the discretised form of the linear PDE which relates $\underline{z}$ and z', (3.12). The solution of this global problem merely adds one iteration to the computations for every remeshing step. It ensures that the local and nonlocal effective plastic strain fields are consistent right from the start of the new increment and thus eliminates a possible source of numerical instabilities. With the nodal values $\underline{z}$ now known, the integration point values of $\bar{z}$ and hence the history variable κ can be updated using the element shape functions.

The determination of new Gauss point data from discrete values at the old Gauss points inevitably introduces a transfer error. In particular, the transfer operators which we use here – and most other transfer operator proposed in literature – shows an artificial diffusion, particularly for relatively coarse meshes. As a consequence of these errors, a set of transferred variables generally no longer satisfies the constitutive equations which internally relate these variables. If not corrected, these violations of the constitutive equations, which are further denoted as inconsistencies, may easily induce a poor convergence or even divergence of subsequent loading increments [24, 71, 101]. Inconsistencies, which originate from the fact that nonlinear relations among variables are not carried over by the – linear – transfer operator (see Chapter 2 [82]), may easily be avoided by transferring a minimal set of independent state variables and reconstructing the remaining (dependent) fields via the constitutive relations.

Restoring equilibrium

Apart from inconsistencies in the local state variables, transfer will generally also lead to loss of equilibrium, which can be regarded as a global inconsistency. To remove the unbalance introduced by the transfer, an equilibrium step is performed in which there is no change in the external loading, nor in the boundary conditions. In order to guarantee convergence in this step, an elastic response is assumed, i.e. ε_p and ω_p are kept constant. This is justified since it is not a physical step, but merely a way to remove artificial, numerical, unbalances.

The elastic iterations result in slight readjustments in the nodal positions $\underset{\sim}{x}$ and the nonlocal variables $\underline{z}$. Note that even though the (weak form of) averaging equation (3.12) was initially satisfied, $\bar{z}$ may vary slightly due to the displacement readjustments, which cause slight changes in the gradient operator. However, since (3.12)

---

[1]Transferred quantities are denoted in the following by a prime (')

is solved simultaneously with equilibrium in the balancing step, it is still satisfied at the end of this step and the solution is consistent also in this respect.

Since stresses are not bounded by a yield surface during the elastic step, it may happen that upon convergence the stress state lies outside the yield surface given by the transferred yield stress, i.e. $\tau_{eq} > \tau_y'$. The plastic state is restored by setting

$$\tau_y = \max(\tau_{eq}, \tau_y') . \tag{3.28}$$

Unlike the approach chosen in Chapter 2 [82] for the uncoupled damage modelling, z and ω_p are not corrected for potential slight inconsistencies. In the present case, retrieving a completely consistent state would require solving a global problem, because the damage, which depends on $\bar{z}$, and the plastic strain $z = \varepsilon_p$ are coupled by the partial differential equation (3.12). The impact of the inconsistencies which may arise in the hardening/softening law is here greatly reduced by the fact that this law has been formulated in a rate form, for which the transferred state variables merely act as an initial condition.

Crack opening

Once a consistent equilibrium state has been restored on the geometry with the new crack segment still closed, this crack segment can be opened. This is done by duplicating the nodes along the new crack segment, attributing one node to each crack face (Chapter 2 [82]). The nodal forces which are acting on both sides of the new crack segment (which were self-equilibrating when the crack segment was closed) now become external forces. Likewise, a residue appears on the discrete set of averaging equations (i.e. $\underline{f}_{\bar{z},\mathrm{int}}^{(i)} \neq \underline{0}$). In order to restore equilibrium with the new boundary conditions, these forces must be eliminated. Note that these forces are very small since the new segment is introduced in a highly damaged region where only low residual stresses remain. As a result, their removal can usually be done in one step and a new equilibrium state is found after a few equilibrium iterations only. Nevertheless, if for some reason (e.g. a too large crack segment) this iteration process diverges, a nodal-relaxation procedure is automatically applied, whereby the initial unbalance is removed gradually in successive substeps (Chapter 2 [82]).

Contrary to uncoupled damaging elastoplastic materials (e.g. Chapter 2 [82]), where the transition from a continuum to a discrete crack is abrupt, with large stress redistributions and a significant amount of energy release, the transition of damage to a crack is here much smoother. The stress redistribution and energy dissipation take place mainly during the damage evolution. This is illustrated in Fig. 3.5, which shows results of the simulation of a shear test on an Arcan specimen, similar to those discussed further in Section 3.4.2. Figs. 3.5 (a) and (b) show the damage and stress state respectively before the opening of the newly inserted crack segment. Figs. 3.5 (c) and (d) represent the situation after the opening of this crack segment. Note that there is no significant change in either damage or stress fields. This contrasts with an uncoupled approach, as followed in Chapter 2 [82], where large stress redistributions are observed in a similar situation.
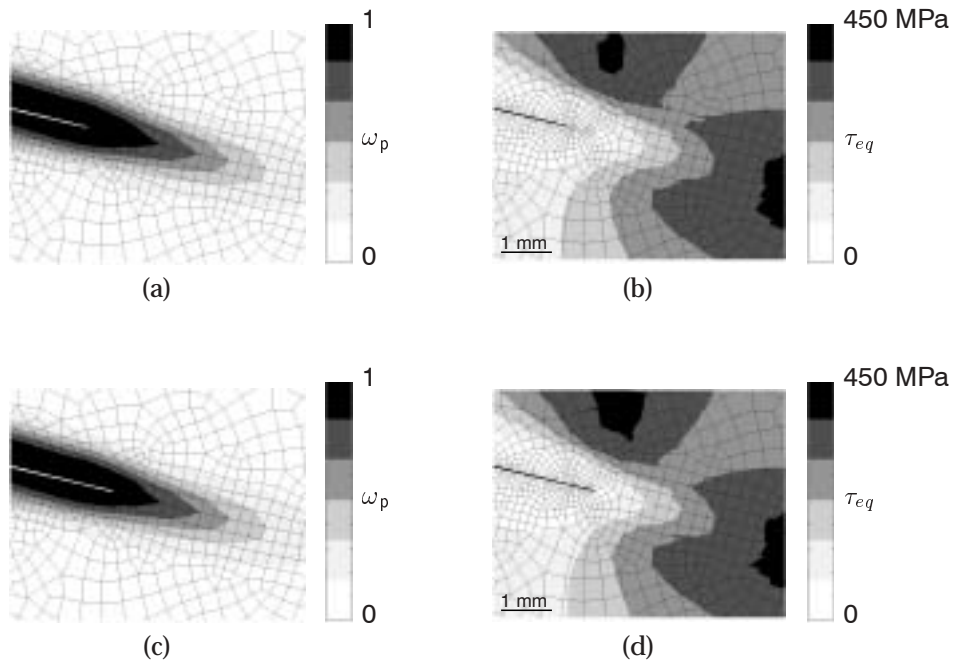
Figure 3.5 — *Small damage and stress redistributions during crack opening. (a) Damage ω_p before crack opening; (b) von-Mises stress τ_{eq} before crack opening; (c) damage after crack opening; (d) von-Mises stress after crack opening.*

3.4 Applications

In this section, a number of simulations are presented, and comparisons are made with published experimental data. The damage model which is used, i.e. that of Section 3.2, assumes that damage growth is governed solely by the effective plastic strain. This model typically focuses on shear failure. It is too restrictive for tensile fracture, which is governed by predominantly spherical void growth and is therefore significantly influenced by the presence of hydrostatic stresses. An extension of the damage theory, which captures this effect, is presently under construction and will be reported in future work. Here we concentrate on situations which are dominated by shear straining, with little void growth, for which the present damage model provides meaningful results.

All examples shown are displacement-driven. Plane strain elements have been used. Bilinear interpolation functions have been used for both the displacement $\underline{u}$ and the nonlocal strain field $\bar{z}$ (see Fig. 3.6). To prevent locking in the plastic regime, selective reduced integration is used, i.e. full, four-point Gauss integration for the shear part of the stress and reduced, one-point integration for the volumetric part.
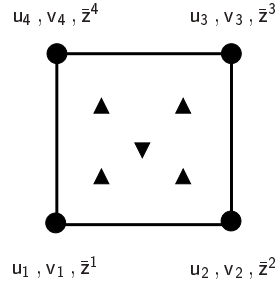
Figure 3.6 — *4u-4$\bar{z}$ element with selective integration.*

3.4.1 Tensile test on a double notched specimen

In order to assess the model's performance, a number of simulations have been carried out of a tensile test on a double notched specimen. The geometry and boundary conditions have been defined in Chapter 2 [82] (Fig. 2.15). The material properties have been summarised in Table 3.1. These values are similar to those reported in [55] for X30Cr13 steel; the internal length ℓ is an estimate of the typical scale of the microstructure, e.g. the grain size. Unless otherwise specified, the default parameters of the computations shown are: Eq. (3.10) for the damage evolution, a crack propagation increment of 0.2 mm and $\omega_{crit} = 0.99$. The crack direction was computed using a semi-circular fan (Fig. 3.3), with intervals of 0.25, 0.5, 0.750 and 1 mm.

Table 3.1 — *Material properties used in the tensile test.*

Shear modulus G	70.3 GPa
Bulk modulus K	136.5 GPa
Initial flow stress $\hat{\tau}_y^0$	443 MPa
Hardening parameter h	300 MPa
Damage parameter κ_i	0
Damage parameter κ_c	1
Internal length ℓ	0.1 mm

The tensile loading causes the development of a plastic shear band between the two notches and gives rise to damage initiation at the notches. Strains start to localise, enforcing the nucleation of two cracks which run towards the centre of the specimen. Fig. 3.7 shows the evolution of the mesh, the damage variable ω_p and the von-Mises stress τ_{eq} at different stages of crack growth. Because of the material softening, stresses are not only low in the crack wake, for compatibility with the boundary conditions, but also at the crack tips. The maximum values are found

away from the crack tips.

(a)   (b)   (c)
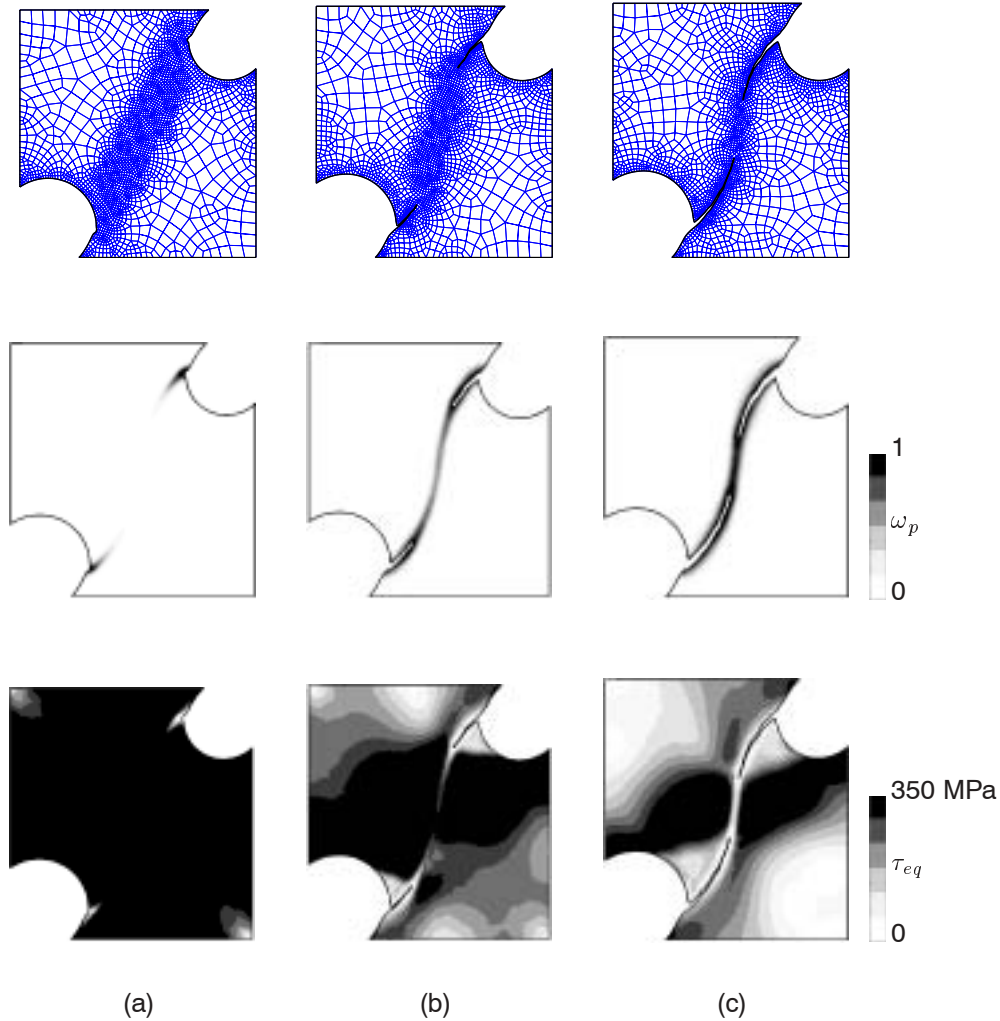
Figure 3.7 — *Crack propagation in the tensile test on a double notched specimen (initially 2700 elements). Mesh and state variables ω_p, τ_{eq}.*

Fig. 3.8 shows the force-displacement curve obtained in this analysis. The points at which the snapshots of Fig. 3.7 were taken are indicated in the diagram. A smooth transition from the continuous damage phase to the cracked phase takes place. The global softening response is the combined effect of the material softening and the geometrical softening due to crack growth. The transfer of variables and the discrete

geometric changes during crack propagation have no sharp discontinuous effect on the force-displacement curve. This is in contrast with an uncoupled approach, e.g. Chapter 2 [82], in which considerable force jumps can be observed at each increment of crack growth, particularly for coarse meshes, as a consequence of stress redistributions.
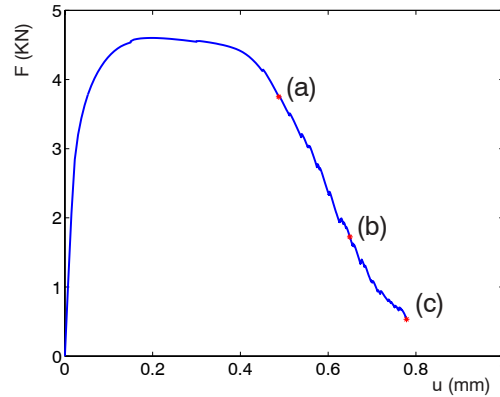
Figure 3.8 — *Force-displacement curve. Smooth transition from the continuous damage to the discrete crack.*

In order to examine the sensitivity of the crack growth algorithm to numerical parameters, the analysis has been repeated for several values of these parameters. Fig. 3.9 shows the load-displacement curves (Fig. 3.9 (a)) and final crack shapes (Fig. 3.9 (b)) obtained with different mesh densities, indicated by the number of elements in the initial mesh. These diagrams show a convergence of results as the finite element mesh is refined. This mesh objectivity is characteristic for the nonlocal constitutive model used.

The influence of the cut-off damage value ω_{crit} in the model should also vanish for values close to 1. Fig. 3.10 shows that there is almost no difference in the force-displacement curve and the crack path.

Small internal lengths lead to more localisation and hence to a more brittle response. This is illustrated in Fig. 3.11, which shows the force-displacement curves for three internal lengths ($\ell = 1 - 3$ mm).

3.4.2   Arcan test

In order to be able to compare the behaviour of the damage-fracture modelling with experiments, simulations have been done of the experiments performed by Amstutz et al. [3, 4] using modified Arcan specimens made of an Aluminium alloy 2024T3. The geometry and boundary conditions have been described in Figs. 2.21 and 2.22.

The material parameters are listed in Table 3.2. These values correspond to those

(a)   (b)
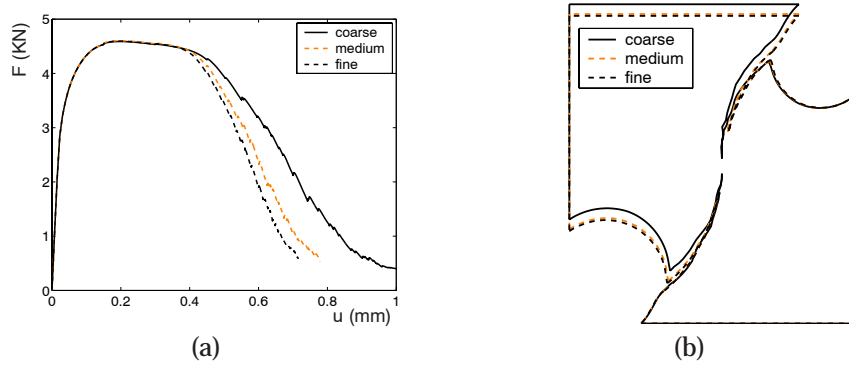
Figure 3.9 — *Sensitivity to mesh coarseness. Force-displacement (a) and final crack paths (b). The initial meshes consist of 1500 (coarse), 2700 (medium) and 4400 (fine) elements respectively.*

(a)   (b)
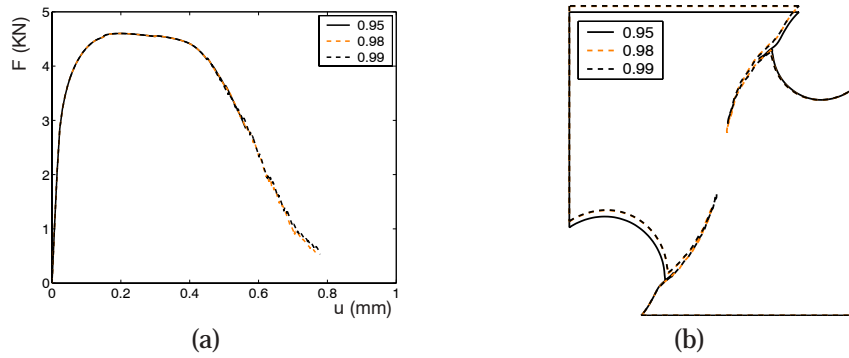
Figure 3.10 — *Sensitivity to ω_{crit}. Force-displacement (a) and final crack paths (b).*

Table 3.2 — *Material parameters used for the Arcan test simulations.*

Shear modulus G	27.5 GPa
Bulk modulus K	59.5 GPa
Initial flow stress $\hat{\tau}_y^0$	345 MPa
Linear hardening parameter h	2000 GPa
Damage parameter κ_i	0
Damage parameter κ_c	0.4
Internal length ℓ	0.3 mm
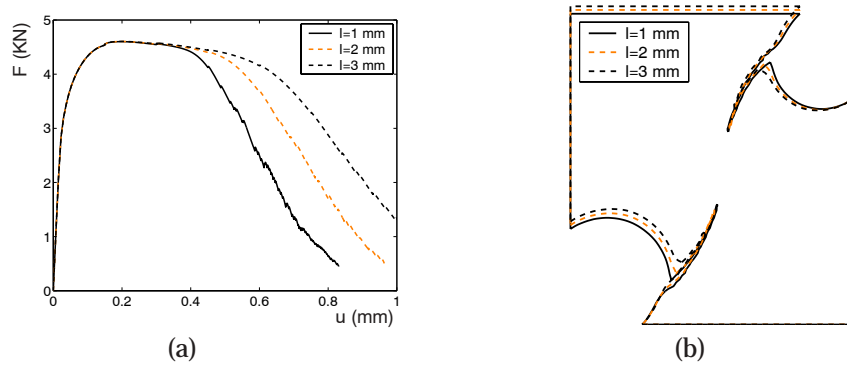
Figure 3.11 — *Sensitivity to internal length ℓ. Force-displacement (a) and final crack paths (b).*

reported in [125]. Nevertheless, the hardening and damage evolution parameters have been determined in order to fit the experimentally determined force-crack length curves. Linear hardening and nonlinear damage according to Eq. 3.10 have been assumed. ω_{crit} has been taken equal to 0.99, the crack increment length is 1 mm. The direction is computed in a semi-circle fan (Fig. 3.3), at distances of 0.5, 1, 1.5 and 2 mm.

Experiments on ductile metals have shown that predominantly mode-I fracture occurs for loading angles between $\beta = 90^o$ (pure tension) and $\beta = 30^o$, with crack paths either straight ($\beta = 90^o$) or bending upwards. For an even larger shear component, $\beta = 15^o$ and $\beta = 0^o$ (simple shear), mode-II fracture occurs, and the cracks propagate downwards along a straight path. It is worth mentioning that this transition from mode-I to mode-II fracture only occurs in ductile fracture. Brittle fracture always happens in mode-I, even under pure shear loading. Since the present damage modelling is applicable only to shear dominated modes, i.e. mode-II fracture, attention is concentrated on the $\beta = 0^o$ and $\beta = 15^o$ cases.

For the considered loading cases, the simulated and experimental crack paths show the same trend as in the experiments (Fig. 3.12): propagation along a straight path. In the $\beta = 15^o$ case, this path has a downwards slope of -5°, with no visible kinking. In the experiments, after a kink early in the growth process, this angle was approximately -7° [3, 4]. The kink near the start of the crack is believed to be due to a transition from mode-I dominated growth to mode-II, which is not captured by the present model. In the pure shear case ($\beta = 0^o$), the simulation predicts crack propagation at an angle of 0°, which is consistent with the assumption of purely mode-II crack growth. The experimental cracks, nevertheless, deviate slightly from the horizontal line. These small discrepancies are probably due to the influence of the boundary conditions, which are not exactly the same in the experiments and simulations. In the experiments the load is transmitted from the plates to the Arcan specimen through bolts, hence allowing for some rotation of the plates; while in the

simulations the plates and the specimen are perfectly bonded.

In the simulation of purely mode-II crack propagation ($\beta = 0^o$), the crack faces tend to touch each other or even to penetrate. Avoiding penetration requires a self-contact algorithm, which was not available in the present framework. However, computations done using a similar model (Chapter 5 [84]), in an operator-split implementation, showed that the influence of contact between the crack faces is only limited and hardly influences the crack growth direction. Therefore, the simulations shown here were done without self-contact, but the penetration is eliminated in each remeshing step.
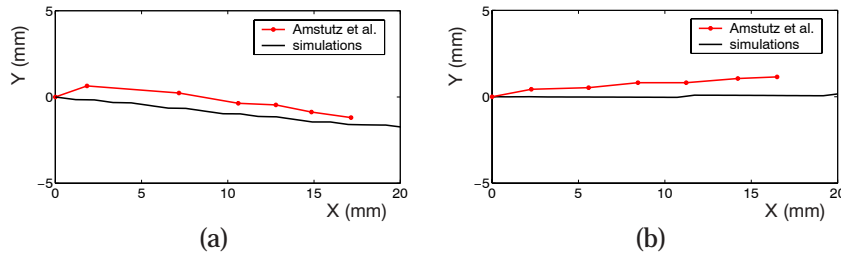
Figure 3.12 — *Predicted and measured crack paths under shear: (a) $\beta = 15^o$, (b) $\beta = 0^o$.*

Fig. 3.13 shows the applied force versus crack length as measure by Amstutz et al. [3, 4] and as obtained in the two simulations.
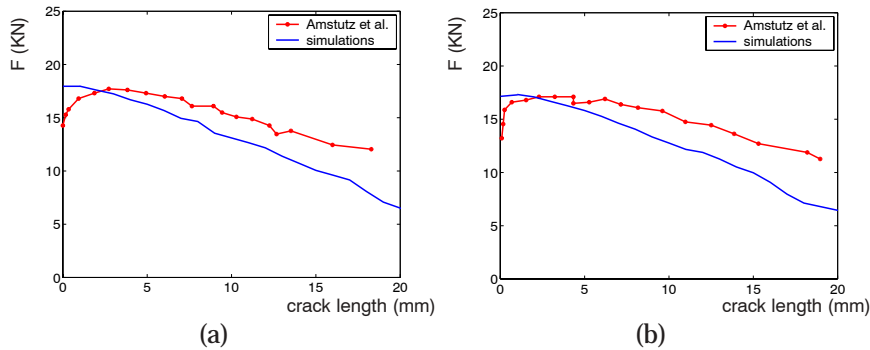
Figure 3.13 — *Force-crack length of shear test on Arcan specimen: experiments versus simulations. (a) $\beta = 15^o$, (b) $\beta = 0^o$.*

Fig. 3.14 shows the evolution of the mesh, the damage variable ω_p and the equivalent stress τ_{eq} for the $\beta = 15^o$ case. It can be seen that the damage strongly localises along the direction of the future crack. A phenomenon that is observed in these simulations is that the maximum damage value is not located at the notch tip, but in its
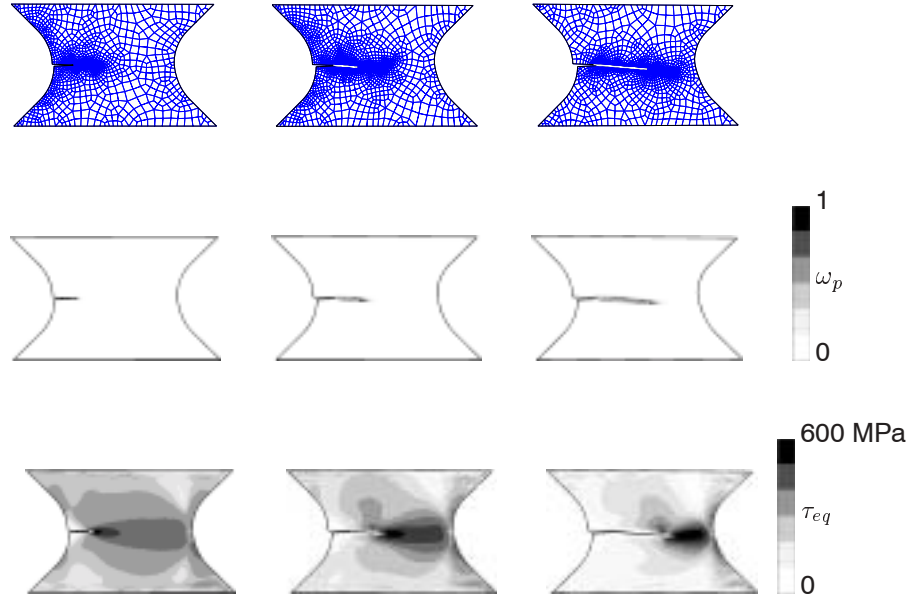
Figure 3.14 — *Crack propagation of Arcan test under shear ($\beta = 15^0$). Mesh and state variables ω_p, τ_{eq}.*

vicinity, at a certain distance (Fig. 3.15). Similar findings were reported by Simone et al. [121] in a brittle damage context, and were attributed to the adopted nonlocal formulation. Indeed, Fig. 3.15 shows that the maximum of the local variable z is at the notch tip, but the nonlocal variable $\bar{z}$ has its maximum away from the crack tip. Since cracks generally initiate at the notch edge and grow into the material, in the simulations ω_p is allowed to spread from its maximum inside, forming a plateau with $\omega_p = \omega_{crit}$, until it reaches the closest boundary, at which point a crack is inserted. This shift phenomenon disappears once the crack starts to propagate (see e.g. Fig. 3.16) and is more pronounced for larger length scales, i.e. stronger nonlocality.

To investigate the effect of damage as the precursor to fracture, the stress and damage field in the wake of the crack and in the fracture process zone ahead of the tip are further scrutinised, where a comparison is made with an uncoupled variant, in which there is no softening prior to crack initiation and crack growth. The uncoupled model has been obtained from the present combined model by eliminating the damage influence from the yield stress, i.e. by setting $\tau_y = \hat{\tau}_y$. However, the damage and nonlocal variables are still computed, by solving the equilibrium and averaging equations in an uncoupled manner. A similar uncoupled approach, albeit local, was
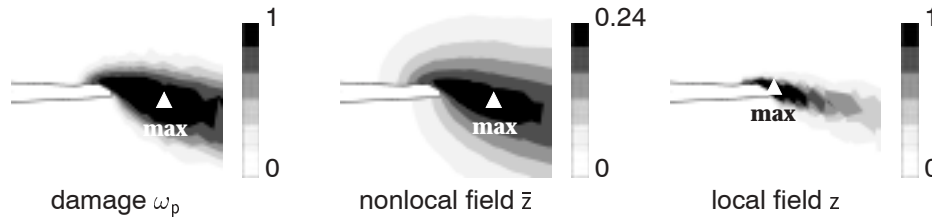
Figure 3.15 — *Shift of the maximum of the variables as a result of the nonlocal variables.*

followed in Chapter 2 [82]. In this uncoupled approach, damage serves only as a discrete crack initiation and propagation criterion. Fig. 3.16 shows the damage and stress state in the vicinity of the crack for the coupled damage model (left) and for the uncoupled model (right). It can be observed that the damage fields are similar, although the distribution in the coupled model is somewhat more localised. Differences are more clear in the stress field, in the process zone and in the crack wake. In the coupled model, the crack wake and process zone are highly damaged, and the equivalent stress is therefore low. In the uncoupled model, which does not experience the damage influence in the continuum elastoplastic phase, the low equivalent stress in the crack wake results from the presence of the traction-free crack faces. On the contrary, the equivalent stress reaches its maximum in the fracture process zone, at the crack tip. This is better illustrated by means of the stress profiles at a certain stage of the crack propagation, along the crack axis (Fig. 3.17) and across it (Fig. 3.18), which correspond to the cross-sections indicated in Fig. 3.16. Along the crack axis ('a-a') (Fig. 3.17), the stresses predicted by the coupled model grow from zero at the crack tip to a maximum at a distance of 5 mm, where the damage vanishes, after which it reaches the same stress level as in the uncoupled model. In the uncoupled model, the yield stress at the crack tip is not degraded by the damage variable and the stress level therefore remains high. Adjacent to the crack, Fig. 3.18, the largest differences in stresses between the coupled and uncoupled model are found in an area of 1 mm at each side of the crack. In front of the crack tip the influence of the damage in the degradation of the yield stress is already visible (Fig. 3.18 'b-b' left). In the section at the crack tip ('c-c') the maximum stress level appears at the crack tip in the uncoupled model, whereas a minimum value can be found in the coupled model. In the section in the crack wake ('d-d') the same effects occur.

The effect of damage on the constitutive response of the continuum, which distinguishes the coupled from the uncoupled approach, becomes apparent in the force-clamp displacement curves, depicted in Fig. 3.19. In the coupled model, the force decrease is caused by two factors: geometric softening, due to the loss of load-carrying area and material softening, due to the damage growth. In the uncoupled model, there is only geometric softening. The pronounced jumps in the uncoupled model are due the build-up and release of stresses at the discretely moving crack tip. In
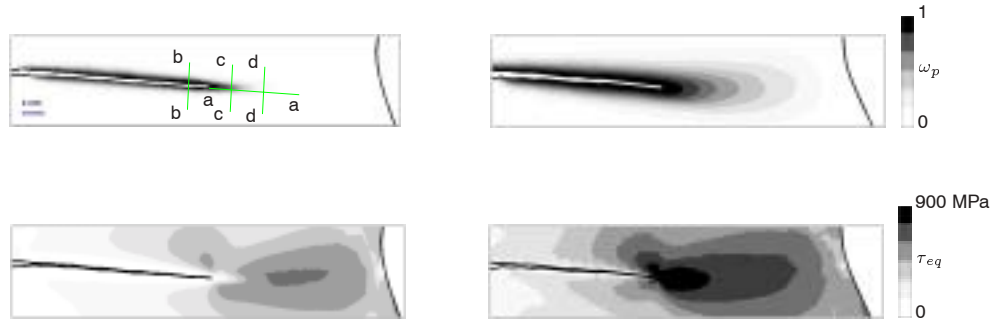
Figure 3.16 — *Coupled (left) versus uncoupled approach (right), crack length 20 mm. Damage ω_p and von-Mises stress τ_{eq}.*
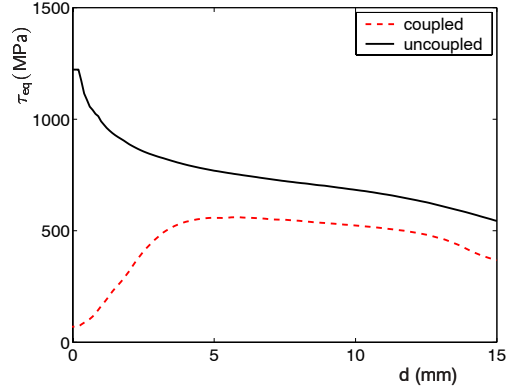
Figure 3.17 — *Stress profiles along the crack axis ('a-a').*

the coupled approach, stresses are nearly completely relaxed by the damage influence before a new crack segment is inserted and no such stress jumps are therefore observed. The force-displacement curve of the continuous model without any crack growth has also been plotted. This model is obtained by removing the crack modelling from the numerical framework. As a result, stresses can only decrease because of damage. However, part of the curve is meaningless, since the damaged area extends over an unrealistically wide zone towards the right of the specimen.

3.5   Conclusions and future work

A combined continuous damage-discontinuous crack model for the simulation of ductile fracture has been presented, which enables to simulate the entire fracture

Section 'b-b' (in front of tip)

Section 'c-c' (tip)

Section 'd-d' (crack wake)
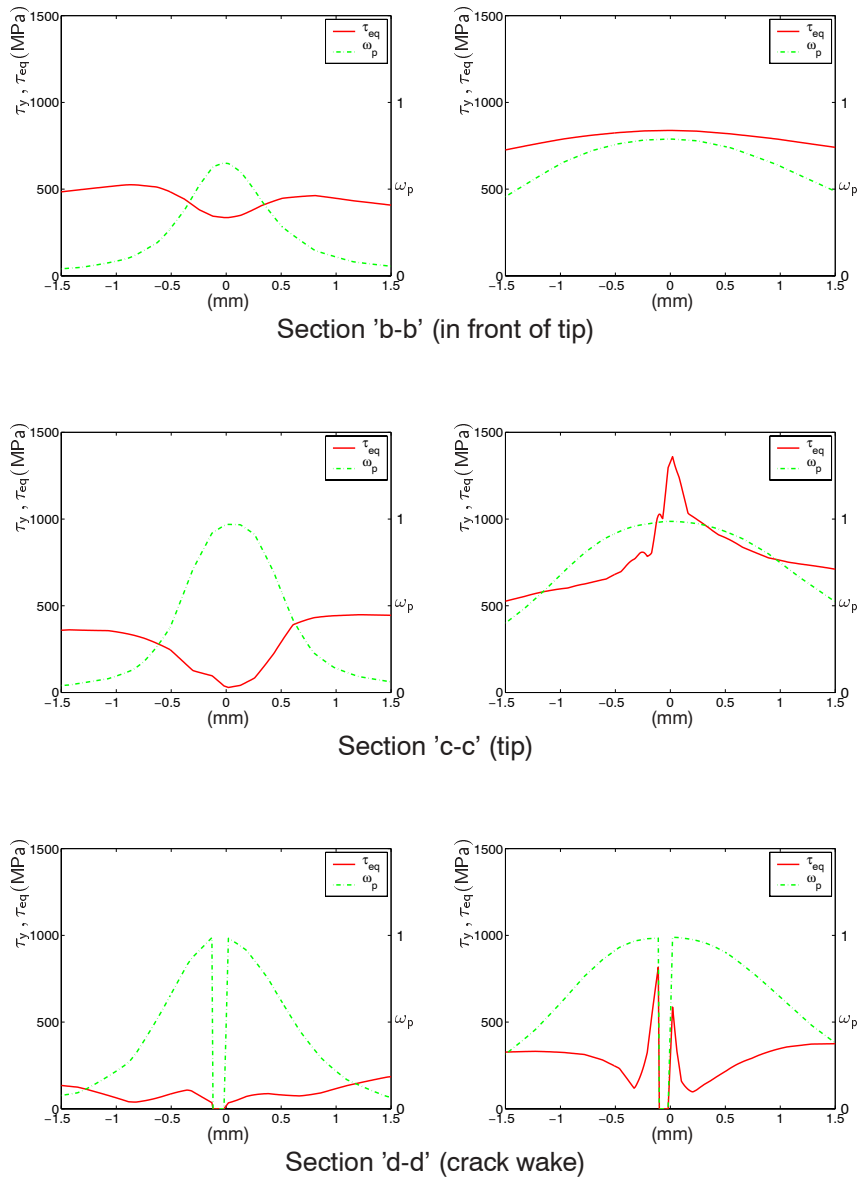
Figure 3.18 — *Coupled (left) versus uncoupled approach (right). Damage (ω_p), yield stress (τ_y) and von-Mises stress (τ_{eq}) fields.*
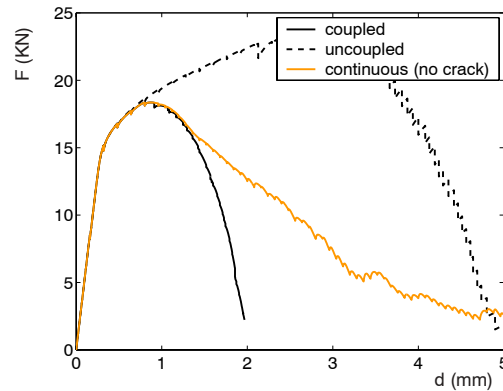
Figure 3.19 — *Force versus displacement ($\beta = 15°$). Uncoupled, coupled and continuous (only damage, no cracks) approaches.*

process, from crack initiation to propagation. The gradient damage model which is thereby used acts as localisation limiter and can be seen as a bridge between the microscopic and the continuum level, accounting for the microscopical nonlocal interactions.

The following conclusions can be drawn:

- Macroscopic softening is accompanied with localising strains, where further plastic straining decreases the finite width of the localisation zone until a discrete crack is approached in the limit. Therefore, the transition from continuous damage to a discrete crack is smooth, which for ductile fracture is more realistic than the sudden changes assumed in elastoplastic fracture mechanics or when using an uncoupled damage model and the widespread damage obtained with a continuous damage model.

- Since J_2 (deviatoric) plasticity and an effective plastic strain driven damage evolution law have been used, the model is mainly suitable for shear failure, and can therefore be applied to metal forming processes such as blanking in which shear strains are dominant. For more general applications a dependence on the hydrostatic stress should be included in the failure mechanism.

- Although ductile damage affects mainly the inelastic material properties in the present modelling, there is evidence that it also affects the elastic properties, which is disregarded in this model. Its relative importance remains to be seen.

- The crack direction and rate of crack propagation depend on the evolution of the localisation in space and time, respectively. Therefore, the validity of the damage evolution law should be assessed with the experimentally measured crack paths. Although the trend of the crack propagation has been captured,

more experiments are needed in order to have more reliable data to compare with.

- The benefits of remeshing in this ductile fracture context are twofold. First, it allows to trace the crack geometry, and secondly it keeps elements from distorting too much. The disadvantage is that transfer of state variables from one mesh to the other introduces errors, which cause inconsistencies among state variables and have a detrimental effect on the convergence of the computations. The robustness of the crack propagation algorithm can be considerably improved by separating the numerical transfer unbalance from the unbalance due to the creation of new traction-free surface. Additional improvements in the robustness could be achieved with a better transfer operator, which would minimise the diffusion errors.

- During crack propagation, localisation takes place mainly in front of the crack tip (in the FPZ), therefore a finer mesh is used there. However, the location of crack initiation is not known a priori and in the present framework one needs an 'a priori' knowledge on where this happens in order to have finer mesh there. A more reliable approach would be to use an adaptive remeshing technique, either based on an error norm or a phenomenological criterion.

From the above conclusions, the following issues need to be addressed: dependence of the damage evolution on the hydrostatic stress; damage influence in the elastic response; and mesh adaptivity.

Chapter 4

A nonlocal triaxiality-dependent ductile damage model for finite strain plasticity [3]

Abstract: In this chapter a nonlocal plasticity-damage framework is developed which allows to describe the evolution of ductile damage in a continuum sense. Focus is on two main aspects of the ductile damage model, which constitute an improvement of recently developed theories. First, the degradation of both the elastic and plastic response is accounted for, using the concept of effective stress and strain equivalence between the homogenised and the hyperelastoplastic matrix material. Second, the role of the stress triaxiality in triggering ductile failure is taken into account by using a triaxiality-dependent local damage-driving variable, whose nonlocal counterpart acts as a localisation limiter. The resulting coupled problem, i.e. equilibrium and nonlocal averaging, is implemented in an implicit, fully coupled form, for which consistent tangent operators are derived. Details of the numerical implementation and remeshing issues are given. To illustrate the response of the model, simulations of tensile tests on notched and unnotched bars are compared with the results of previous models and with published experimental data.

4.1 Introduction

It is well established that void nucleation, void growth and void coalescence are the microscopic mechanisms drivers for ductile failure. From a continuum mechanics point of view, these mechanisms cause a degradation of the yield stress (strain-softening) and of the elastic properties [74]. Microscopically based models can describe the decrease of the yield strength as a result of void development, often using the void volume fraction as a measure of the degradation [56, 129]. On the other hand, phenomenological models, which are often based on continuum damage mechanics, introduce one or more variables to degrade the elastic material properties

---

[3]This Chapter is based on [83].

and/or the yield stress using the notion of effective stress (or strain) [73]. Softening plasticity theories can also be considered to be a member of this class, e.g. [40] In both classes of models, the evolution of damage (void volume fraction) depends on the amount of plastic straining and on the hydrostatic stress. The influence of hydrostatic stress reflects the fact that voids are nucleated more easily and grow faster in the presence of a tensile hydrostatic stress state. Indeed, there is ample experimental evidence of the effect of triaxiality (ratio between hydrostatic and shear stress) on the strength and ductility of metals [62, 79] and the effect has been explained by several analytical and numerical models [19, 73, 93, 108].

The evolution of damage causes strain-softening in the continuum theories used to describe it, which is known to lead to pathological localisation and strongly mesh dependent results in a finite element setting. To overcome this difficulty, the continuum modelling must be supplied with an internal length scale, such as provided by nonlocal [14, 131], gradient [40, 97] and Cosserat models [37], or with an internal time scale in the form of a strain rate dependent behaviour [122]. The internal length is related to the average void spacing or the average spacing of inclusions in the material. Of the above alternatives, gradient models are relatively simple to implement numerically, as has been shown in recent years for both small-strain and large-strain plasticity [53, 88, 123].

The purpose of this chapter is to develop a large-strain ductile damage formulation which captures the influence of hydrostatic stress on damage growth and which uses a gradient enhancement as a localisation limiter. This gradient enhancement is similar to the form used in [50] and in earlier gradient enhanced damage elastoplasticity models [45, 53], where the nonlocal enrichment was inspired by earlier work on quasibrittle damage [97]. However, the formulations developed in [45, 50, 53] were insensitive to the hydrostatic stress and are therefore expected to give reasonable results in problems which are dominated by shear deformation, see for instance [23] for such an application. Triaxiality-dependent ductile damage formulations reported in the literature, on the other hand, often neglect the occurrence of pathological localisation and the need for a regularisation method. Notable exceptions are the models proposed by Leblond et al. [69] and Tvergaard & Needleman [131], which both use an integral form of nonlocality. In the present chapter we aim to combine the gradient enhancement which underlies the ductile damage models of Refs. [45, 50, 53] (and which proved to be successful in regularising localisation of deformation) with a physically more realistic pressure-dependent ductile damage description. The influence of damage is introduced using the effective stress concept [65, 74]. On top of the desired yield stress degradation, a degradation of the local elastic stiffness is thereby introduced. The influence of this elastic degradation on the overall mechanical response will be examined, as well as the effect of hydrostatic stress on damage growth in the proposed model.

The structure of this chapter is as follows. The model's governing equations are outlined in Section 4.2. The time discretisation of these equations is dealt with in Section 4.3. Details of the numerical implementation are given in Section 4.4. In particular attention is paid to the derivation of the consistent tangent operators and

to the issue of remeshing, which is used to prevent large element distortions in the simulations. Section 4.5 shows simple analyses of the homogeneous response of the model, as well as more complex analyses of tensile tests on notched and unnotched specimens. The influence of the triaxiality on the ductility is clearly shown using different notch radii. Conclusions are finally drawn in Section 4.6.

4.2 Gradient enhanced large strain damage-elastoplasticity model

In this section, the equations which govern the triaxiality-dependent gradient-enhanced plasticity-damage model are presented. The notion of effective stress [65] is recalled in Section 4.2.1. The behaviour of the matrix material is modelled via a hyperelastoplastic material [117] (Section 4.2.2). Assuming strain equivalence, the governing equations of the homogenised material are obtained in Section 4.2.3. The gradient enhancement is introduced in Section 4.2.4. A triaxiality-dependent local damage driving variable is proposed in Section 4.2.5.

4.2.1 Effective stress and elasto-plasticity

In continuum models which are used for design purposes, one usually wishes to consider the aggregate of matrix material and microvoids or microcracks as a homogeneous continuum. Continuum damage mechanics relies on the principle of strain equivalence [73, 118], which states that the homogenised, damaged material responds to a given stress τ in the same way as the (undamaged) matrix material responds to the effective stress

$$\hat{\tau} \;=\; \frac{\tau}{(1 - \omega_p)}\,, \tag{4.1}$$

where the damage variable ω_p in this relation (4.1) characterises the fraction of cross-sectional area which is taken up by voids and cracks; $\omega_p = 0$ represents an undamaged state, and $\omega_p = 1$ complete failure, as would for instance occur in a macroscopic crack. This principle can be used to derive effective constitutive equations for the damaged material based on the equations which govern the undamaged material response, simply by replacing the stress tensor τ in these equations by the effective stress tensor $\hat{\tau}$ according to (4.1).

4.2.2 Elastoplastic matrix material behaviour

Following Geers [50], the matrix material is assumed to behave according to a large strain elastoplasticity model, which is a simplified, yet exact, representation of earlier work of Simo [117]. Salient features of this constitutive model are that it allows to retain the structure of the classical small strain return-mapping algorithms, that the

flow rule is derived from the principle of maximum plastic dissipation and that it leads to a symmetric tangent.

The deformation gradient is split in an elastic and a plastic part, according to the multiplicative decomposition

$$\boldsymbol{F} \;=\; \boldsymbol{F}_e \cdot \boldsymbol{F}_p \,. \tag{4.2}$$

The elastic response is expressed in terms of the elastic right Cauchy-Green tensor $\boldsymbol{b}_e \equiv \boldsymbol{F}_e \cdot \boldsymbol{F}_e^T$, and can be derived from a free energy potential. For convenience the following hyperelastic generalisation of linear elasticity is adopted here (see [50, 117] for comments on the hyperelastic nature)

$$\hat{\boldsymbol{\tau}} \;=\; \tfrac{1}{2} \, {}^{4}\!\boldsymbol{H} : \ln \boldsymbol{b}_e \,, \tag{4.3}$$

where $\hat{\boldsymbol{\tau}}$ is the effective Kirchhoff stress tensor

$${}^{4}\!\boldsymbol{H} \;=\; K \, \boldsymbol{I} \otimes \boldsymbol{I} + 2G \left({}^{4}\!\boldsymbol{I}^{s} - \tfrac{1}{3} \boldsymbol{I} \otimes \boldsymbol{I} \right), \tag{4.4}$$

and K and G denote the bulk and shear modulus respectively.

Plastic yielding is assumed to follow the J_2 (von Mises) criterion, i.e the yield surface is given by

$$\hat{\phi}(\hat{\boldsymbol{\tau}}, \hat{\tau}_y) \;\equiv\; \hat{\tau}_{eq} \,-\, \hat{\tau}_y \;\leqslant\; 0 \,, \tag{4.5}$$

where

$$\hat{\tau}_{eq} \;\equiv\; \sqrt{\frac{3}{2} \hat{\boldsymbol{\tau}}^d : \hat{\boldsymbol{\tau}}^d} \tag{4.6}$$

and $\hat{\tau}_y$ is the current yield stress of the matrix. The evolution equation for the effective plastic strain ε_p and the flow rule follow from the principle of maximum dissipation as [117]

$$\dot{\varepsilon}_p \;=\; -\dot{\gamma} \, \frac{\partial \hat{\phi}}{\partial \hat{\tau}_y} \;=\; \dot{\gamma} \tag{4.7}$$

$$\overset{\nabla}{\boldsymbol{b}}_e \;=\; -2\dot{\gamma} \, \frac{\partial \hat{\phi}}{\partial \hat{\boldsymbol{\tau}}} \cdot \boldsymbol{b}_e \;=\; -3\dot{\gamma} \, \frac{\hat{\boldsymbol{\tau}}^d}{\hat{\tau}_{eq}} \cdot \boldsymbol{b}_e \,, \tag{4.8}$$

where $\overset{\nabla}{\boldsymbol{b}}_e$ is the Lie derivative of $\boldsymbol{b}_e$ and $\dot{\gamma}$ is a plastic multiplier which must satisfy the loading-unloading conditions

$$\dot{\gamma} \;\geq\; 0, \qquad \hat{\phi} \;\leq\; 0, \qquad \dot{\gamma}\,\hat{\phi} \;=\; 0 \tag{4.9}$$

and, in case of plastic loading, the consistency condition

$$\dot{\hat{\phi}} \;=\; 0 \,. \tag{4.10}$$

Note that the flow rule (4.8) is expressed in terms of $\boldsymbol{b}_e$, which reflects its representation in the current configuration. If desired, however, this flow rule can be rewritten

in the reference configuration, involving the plastic right Cauchy-Green deformation tensor C_p.

Assuming isotropic hardening, the evolution of the yield stress $\hat{\tau}_y$ can be expressed in rate form as

$$\dot{\hat{\tau}}_y \;=\; h_\varepsilon \dot{\varepsilon}_p \,, \tag{4.11}$$

where the current hardening modulus h_ε may be a function of ε_p. The initial yield stress $\hat{\tau}_y^o$ is used as an initial value upon integration of this relation.

4.2.3 Coupled damage-elastoplasticity model

A coupled damage-elastoplasticity model can be obtained by substituting Eq. (4.1) in the elastoplastic matrix material model as presented in Section 4.2.2. Damage will then affect both the elastic and the plastic properties of the homogenised material.

The elastic response is obtained from Eqs. (4.1) and (4.3) as

$$\boldsymbol{\tau} \;=\; (1 - \omega_p)\tfrac{1}{2}{}^4\!\boldsymbol{H} : \ln\boldsymbol{b}_e \,. \tag{4.12}$$

The flow rule can also be rewritten in terms of the homogenised stress tensor. However, for the numerical implementation of the model it turns out to be advantageous to retain expression (4.8) in terms of the effective stress. Note that the plastic flow rule used here and in [50] is isochoric. This contrasts with the family of models based on Gurson's yield criterion and therefore introduces a certain degree of approximation. In reality, plastic flow of porous materials may have a dilatational component as a result of the volume increase of the pores. In most practical situations, however, this plastic dilatation is small compared with the shear part of the deformation and so neglecting it seems a reasonable assumption. Likewise, the influence of the hydrostatic stress is not implicitly incorporated in the yield criterion. However, as we will see below, the hydrostatic stress component does enter the yield criterion via the evolution of damage, so that the overall response is nevertheless sensitive to it.

Note that substitution of (4.1) in the yield criterion according to (4.5) has the same effect as defining a damaged yield stress as done in [45, 50, 53], i.e.

$$\tau_y \;=\; (1 - \omega_p)\hat{\tau}_y. \tag{4.13}$$

4.2.4 Damage evolution and gradient enhancement

Now that we have established the influence of damage on the elastoplastic part of the constitutive model, only the evolution of damage under the influence of stress and strain remains to be specified. In the earlier modelling proposed by Geers et al. [50, 53], damage evolution depended only on plastic strain. However, as argued in the introduction, this coupling may be too restrictive if one wishes to describe problems in which significant hydrostatic stresses exist. For this reason, a connection

to a generalised damage driving force, denoted by z, is made here. If this variable is set equal to $z = \varepsilon_p$, the evolution relations used in [50, 53] are retrieved. A different definition, which accounts for the influence of hydrostatic stress, is proposed below in Section 4.2.5.

The dependence of ω_p on z is controlled by a history variable κ. The damage rate is related to the time derivative of κ via the evolution equation

$$\dot{\omega}_p \,=\, h_\omega\, \dot{\kappa}\,. \tag{4.14}$$

In the remainder of this chapter we use for h_ω the piecewise constant form

$$h_\omega \,=\, \left\{ \begin{array}{ll} \frac{1}{\kappa_c - \kappa_i} & \quad \text{if} \quad \kappa_i \leq \kappa \leq \kappa_c \\ 0 & \quad \text{otherwise} \end{array} \right. \tag{4.15}$$

in which the parameters κ_i and κ_c control the onset of damage growth and complete failure respectively. In addition to these parameters, an initial value for ω_p must be specified, which is here naturally taken to be zero.

The history variable κ is related to a nonlocal variable $\bar{z}$ via the Kuhn-Tucker conditions

$$\dot{\kappa} \geq 0, \qquad \bar{z} - \kappa \leq 0, \qquad \dot{\kappa}\,(\bar{z} - \kappa) = 0 \tag{4.16}$$

and the initial value $\kappa_{(t=0)} = \kappa_i$.

The nonlocal field variable $\bar{z}$ and its local counterpart z are related through the nonlocal Helmholtz equation [45, 50, 53, 97], which is here defined in the deformed (Eulerian) configuration as

$$\bar{z} - \ell^2\, \nabla^2 \bar{z} \,=\, z\,, \tag{4.17}$$

where ∇^2 is the laplacian (with respect the current configuration) and ℓ is an internal length parameter, whose physical interpretation can be related to void interactions. Note that ℓ and ∇^2 can also be defined with respect the reference (material) configuration – see Reference [53] for a discussion on the differences between the Eulerian and Lagrangian nonlocality. A homogeneous Neumann boundary condition

$$\vec{\nabla}\bar{z} \cdot \vec{n} \,=\, 0 \tag{4.18}$$

is assumed everywhere on the current boundary Γ with outward normal $\vec{n}$. The boundary value problem given by Eqs. (4.17) and (4.18) ensures that damage will localise in a finite volume, set by the length parameter ℓ, and that a finite amount of energy is thus dissipated in the damage process. This boundary value problem must be solved simultaneously with the equilibrium equations; see Refs. [45, 50, 53, 97, 99] for more background on this type of regularisation.

4.2.5 A phenomenological local damage driving variable

It is known that ductile damage grows with increasing plastic strain and is promoted by a high stress triaxiality. These influences are reflected by the following

phenomenological equations for the local damage driving variable

$$
\begin{aligned}
\mathsf{z}_{(t=0)} &= 0 \\
\dot{\mathsf{z}} &= h_{\mathsf{z}} \dot{\varepsilon}_p \\
h_{\mathsf{z}} &= \left\langle 1 + A\, \frac{\tau_h}{\tau_{eq}} \right\rangle \varepsilon_p^B
\end{aligned}
\tag{4.19}
$$

with A and B constants and $<>$ the so-called Macaulay brackets: $\langle x \rangle = \frac{1}{2}(x + |x|)$. Equation (4.19) is based on Goijaerts's [55] generalisation of Oyane's model for porous elastoplastic materials [93] . This particular form was shown by Goijaerts to be capable of predicting the onset of ductile failure for a range of triaxiality ratios $\frac{\tau_h}{\tau_{eq}}$. Note that $\frac{\tau_h}{\tau_{eq}} = \frac{\hat{\tau}_h}{\hat{\tau}_{eq}}$, i.e. the homogenised and effective triaxiality coincide. Higher values of $\frac{\tau_h}{\tau_{eq}}$ clearly lead to a faster growth of z in (4.15) and therefore of the damage variable ω_p. The Macaulay brackets limit this influence in the compressive range and thus prevent a decrease of z.

4.3 Time discretisation

In finite element simulations, the constitutive equations of the previous section need to be integrated numerically. For this purpose, it is convenient to formulate the elastoplastic part of the constitutive model in terms of effective quantities. The integration of this part can then be done with exactly the same return mapping algorithm proposed by Simo [117] and the influence of damage can be applied by multiplying the resulting effective stress by $(1 - \omega_p)$. Below we briefly outline the return mapping for J_2 plasticity (see [117] or [50] for details) and then concentrate on the integration of the damage influence.

4.3.1 J_2 plasticity: Radial return

The return-mapping algorithm for the present J_2 plasticity model reduces to a classic radial return [137]. The implementation is done in a tensorial form as in [50], whereby the spectrally decomposed form as used in [117] is avoided. This is possible because of the underlying isotropy assumption, whereby the hyperelastic linear relation adopted in (4.3) yields commuting stress and strain tensors.

The return mapping in the effective stress space is expressed as

$$
\hat{\boldsymbol{\tau}} = {}^{\star}\hat{\boldsymbol{\tau}} - 2G\Delta\gamma\hat{\boldsymbol{N}} ,
\tag{4.20}
$$

where the effective trial stress ${}^{\star}\hat{\boldsymbol{\tau}}$ is computed from

$$
{}^{\star}\hat{\boldsymbol{\tau}} = \tfrac{1}{2}\,{}^{4}\boldsymbol{H} : \ln {}^{\star}\boldsymbol{b}_e \quad \text{with} \quad {}^{\star}\boldsymbol{b}_e = \boldsymbol{f} \cdot \boldsymbol{b}_e^t \cdot \boldsymbol{f}^T
\tag{4.21}
$$

and the normal to the yield surface $\hat{N}$ is given by

$$\hat{N} \ \equiv\ \frac{3}{2}\,\frac{\hat{\boldsymbol{\tau}}^d}{\hat{\tau}_{eq}} \ =\ \frac{3}{2}\,\frac{{}^{\star}\hat{\boldsymbol{\tau}}^d}{{}^{\star}\hat{\tau}_{eq}} \ \equiv\ {}^{\star}\hat{N}\,. \tag{4.22}$$

Trial values are denoted by a left superscript ${}^{\star}(\cdot)$ and the values of the previous increment by a right superscript $(\cdot)^t$; f is the deformation gradient relative the to the beginning of the time step (t). Equations (4.20-4.22) and the equivalent stress definition (4.6) allow to express the equivalent effective stress $\hat{\tau}_{eq}$ as a function of $\Delta\gamma$

$$\hat{\tau}_{eq} \ =\ {}^{\star}\hat{\tau}_{eq}\ -\ 3G\Delta\gamma\,. \tag{4.23}$$

Numerical integration of the matrix hardening relation (4.11) with an Euler backward rule gives

$$\hat{\tau}_y \ =\ \hat{\tau}_y^t + h_\varepsilon(\varepsilon_p)\Delta\gamma \quad\text{with}\quad \varepsilon_p \ =\ \varepsilon_p^t + \Delta\gamma\,. \tag{4.24}$$

The increment of the plastic multiplier, $\Delta\gamma$, is obtained by enforcing the yield condition $\hat{\phi} = 0$, resulting in

$$\hat{\phi} \ =\ {}^{\star}\hat{\phi} - [3\,G\,\Delta\gamma - h_\varepsilon(\varepsilon_p)]\Delta\gamma \ =\ 0\,, \tag{4.25}$$

with ${}^{\star}\hat{\phi} = {}^{\star}\hat{\tau}_{eq} - \hat{\tau}_y^t$.

In general, this equation has to be solved iteratively. However, in the linear hardening case, i.e. if h_ε is a constant denoted by H, $\Delta\gamma$ is given in closed form by

$$\Delta\gamma \ =\ \frac{{}^{\star}\hat{\phi}}{H + 3\,G}\,. \tag{4.26}$$

Observe that since the return mapping is expressed entirely in the effective stress space (because damage affects the elasticity as well), damage does not appear in the above expression of $\Delta\gamma$, contrary to the algorithm developed in [50] (where damage only affects plasticity).

4.3.2 Integration of the damage evolution equations

Analogically to the hardening relation, Equation (4.19), which drives the softening part of the response, is integrated numerically using the Euler backward rule

$$z \ =\ z_t + h_z(\boldsymbol{\tau},\varepsilon_p)\Delta\gamma\,. \tag{4.27}$$

The nonlocal variable $\bar{z}$ is then obtained by solving the coupled boundary value problem defined by equilibrium and the nonlocal averaging equation (4.17). Once $\bar{z}$ is obtained, κ can be readily updated via $\kappa = \max(\bar{z}\,,\kappa^t)$. The damage variable ω_p is obtained once more using an implicit Euler integration for Eq. (4.15), resulting in

$$\omega_p \ =\ \begin{cases} 0 & \text{if}\quad \kappa \le \kappa_i \\ \omega_p^t + \frac{\Delta\kappa}{\kappa_c - \kappa_i} & \text{if}\quad \kappa_i < \kappa < \kappa_c \\ 1 & \text{if}\quad \kappa \ge \kappa_c\,. \end{cases} \tag{4.28}$$

4.4 Finite element implementation

The finite element implementation of the triaxiality-dependent damage-plasticity modelling developed in the previous sections can be done largely analogically to that of the triaxiality-independent model of Ref. [50]. The main difference is that instead of the effective plastic strain, a generalised driving variable z is used in Eq. (4.17). This and the dependence of this variable on the triaxiality requires some modifications of the finite element implementation, which are detailed below for the two governing partial differential equations, i.e. equilibrium and Eq. (4.17), in Sections 4.4.1 and 4.4.2 respectively. Both equations are first casted in a weak form and subsequently linearised in order to facilitate a full Newton-Raphson solution strategy. The finite element discretisation of the linearised problems is given in Section 4.4.3. Finally, some comments are made on remeshing and the transfer of variables. The former is necessary in order to keep the elements well shaped throughout the computations and the latter to ensure continuity of the deformation and damage development across the different meshes.

4.4.1 Equilibrium equation

Following the weighted residuals approach, the weak form of the equilibrium equation on the current, deformed configuration Ω can be derived in the usual way as

$$\int_\Omega (\vec{\nabla}\vec{w})^T : \boldsymbol{\tau}\, \frac{1}{J}\, d\Omega \;=\; \int_\Gamma \vec{w}\cdot\vec{p}\, d\Gamma\,, \tag{4.29}$$

where $\vec{w}$ is a test function which must satisfy the usual requirements, J is the volume change ratio, Γ is the boundary to Ω and $\vec{p}$ the traction vector acting on this boundary. Body forces have been neglected. The linearised form of (4.29) is given by

$$\int_\Omega (\vec{\nabla}\vec{w})^T : \left[-{}^4\boldsymbol{I}^{RT}\cdot\boldsymbol{\tau} : \boldsymbol{L}_\delta^T \;+\; \delta\boldsymbol{\tau} \right] \frac{1}{J}\, d\Omega$$
$$= \int_\Gamma \vec{w}\cdot\vec{p}\, d\Gamma - \int_\Omega (\vec{\nabla}\vec{w})^T : \boldsymbol{\tau}\, \frac{1}{J}\, d\Omega\,, \tag{4.30}$$

where $\boldsymbol{L}_\delta^T$ denotes the spatial gradient of the infinitesimal displacements, i.e. $\boldsymbol{L}_\delta^T = \vec{\nabla}\delta\vec{u}$.

Linearisation of Eq. (4.1) yields for the stress variation $\delta\boldsymbol{\tau}$

$$\delta\boldsymbol{\tau} \;=\; -\delta\omega_p\hat{\boldsymbol{\tau}} \;+\; (1-\omega_p)\delta\hat{\boldsymbol{\tau}}\,, \tag{4.31}$$

with $\delta\hat{\boldsymbol{\tau}}$ the infinitesimal stress variation due to the undamaged elastoplastic response of the effective medium. This effective stress variation is linked to the variation $\delta\ln{}^\star\boldsymbol{b}_e$ by its tangent operator, which is largely identical to [50] for elastoplastic

behaviour (except for coefficient b_1, which accounts for the implicit integration of the rate form of the hardening relation):

$$\delta\hat{\boldsymbol{\tau}} = {}^4\boldsymbol{C}_{ep} : \delta\ln{}^{\star}\boldsymbol{b}_e \,, \tag{4.32}$$

with

$$
\begin{aligned}
{}^4\boldsymbol{C}_{ep} &= \left[b_0\, \boldsymbol{I}{\otimes}\boldsymbol{I} + (1 - 3b_0){}^4\boldsymbol{I}^s + 2(b_0 - b_1){}^{\star}\boldsymbol{N}{\otimes}{}^{\star}\boldsymbol{N} \right] : \tfrac{1}{2}{}^4\boldsymbol{H} \\
&= \left(\frac{K}{2} - \frac{G}{3} + b_0 G \right)\, \boldsymbol{I}{\otimes}\boldsymbol{I} + (1 - 3b_0)G\, {}^4\boldsymbol{I}^s + 2G(b_0 - b_1)\, {}^{\star}\boldsymbol{N}{\otimes}{}^{\star}\boldsymbol{N} \,,
\end{aligned}
\tag{4.33}
$$

where

$$b_0 = \frac{\Delta\gamma\, G}{{}^{\star}\tau_{eq}} \quad \text{and} \quad b_1 = \frac{G c_1}{c_1^2 + \frac{\partial h_\varepsilon}{\partial\varepsilon_p}} \quad \text{with} \quad c_1 = 3G + h_\varepsilon \,. \tag{4.34}$$

The variation $\delta\ln{}^{\star}\boldsymbol{b}_e$ is expressed in terms of the displacement variations $\boldsymbol{L}_\delta^T$ as

$$\delta\ln{}^{\star}\boldsymbol{b}_e = \frac{\partial\ln{}^{\star}\boldsymbol{b}_e}{\partial{}^{\star}\boldsymbol{b}_e} : \frac{\partial{}^{\star}\boldsymbol{b}_e}{\partial\boldsymbol{L}_\delta^T} : \boldsymbol{L}_\delta^T \,. \tag{4.35}$$

The first right-hand side term in (4.31) can be written as

$$-\delta\omega_p\hat{\boldsymbol{\tau}} = \boldsymbol{C}_d\delta\bar{\mathsf{z}} \,, \tag{4.36}$$

with $\boldsymbol{C}_d$ defined as

$$\boldsymbol{C}_d = -\frac{\partial\omega_p}{\partial\kappa}\frac{\partial\kappa}{\partial\bar{\mathsf{z}}}\hat{\boldsymbol{\tau}} \,. \tag{4.37}$$

Substitution of Eqs. (4.31-4.37) in Eq. (4.30) gives

$$
\begin{aligned}
&\int_\Omega (\vec{\nabla}\vec{w})^T : \left[-{}^4\boldsymbol{I}^{RT}\cdot\hat{\boldsymbol{\tau}} + {}^4\boldsymbol{C}_{ep} : \frac{\partial\ln{}^{\star}\boldsymbol{b}_e}{\partial{}^{\star}\boldsymbol{b}_e} : \frac{\partial{}^{\star}\boldsymbol{b}_e}{\partial\boldsymbol{L}_\delta} \right] : \boldsymbol{L}_\delta^T\frac{(1-\omega_p)}{J}\, d\Omega + \\
&\int_\Omega (\vec{\nabla}\vec{w})^T : \boldsymbol{C}_d\,\delta\bar{\mathsf{z}}\frac{1}{J}\, d\Omega = \int_\Gamma \vec{w}\cdot\vec{p}\,d\Gamma - \int_\Omega (\vec{\nabla}\vec{w})^T : \hat{\boldsymbol{\tau}}\frac{(1-\omega_p)}{J}\, d\Omega \,,
\end{aligned}
\tag{4.38}
$$

where τ has been replaced by $(1 - \omega_p)\hat{\boldsymbol{\tau}}$.

A drawback of this model, with respect to [50], is that the left hand side of Eq. (4.38), which will yield two partitions of the stiffness submatrices (see below in Eq. (4.46)) becomes zero at failure ($\omega_p = 1$).

4.4.2 Averaging equation

The weak form of the averaging equation (Eq. (4.17)) is given by [50]

$$\int_\Omega \left(w_{\bar{\mathsf{z}}}\,\bar{\mathsf{z}} + \ell^2\,\vec{\nabla}w_{\bar{\mathsf{z}}}\cdot\vec{\nabla}\bar{\mathsf{z}} - w_{\bar{\mathsf{z}}}\,\mathsf{z} \right) d\Omega = 0 \,, \tag{4.39}$$

where use has been made of the divergence theorem and of boundary condition (4.18) and in which $w_{\bar{z}}$ is a scalar test function. Its linearised form can be derived along the same lines as in [50] and reads

$$
\int_{\Omega} \left[\left(w_{\bar{z}}\,\bar{z} + \ell^2\,\vec{\nabla}w_{\bar{z}} \cdot \vec{\nabla}\bar{z} - w_{\bar{z}}\,z \right) \boldsymbol{I} - \ell^2\vec{\nabla}w_{\bar{z}}\otimes\vec{\nabla}\bar{z} : 2\,{}^{4}\boldsymbol{I}^{s} \right] : \boldsymbol{L}_{\delta}^{T}\,d\Omega
$$
$$
- \int_{\Omega} w_{\bar{z}}\,\delta z\,d\Omega + \int_{\Omega} \left[w_{\bar{z}}\,\delta\bar{z} + \ell^2\,\vec{\nabla}w_{\bar{z}} \cdot \vec{\nabla}\delta\bar{z} \right] d\Omega \;=\; \qquad (4.40)
$$
$$
- \int_{\Omega} \left[w_{\bar{z}}\,\bar{z} + \ell^2\,\vec{\nabla}w_{\bar{z}} \cdot \vec{\nabla}\bar{z} \;-\; w_{\bar{z}}\,z \right] d\Omega \,.
$$

The variation δz depends on the type of evolution law. For Goijaerts's model, it is given by

$$
\delta z \;=\; \delta(h_z\Delta\varepsilon_p) \;=\; \boldsymbol{M}_{ep} : \frac{\partial \ln{}^{\star}\boldsymbol{b}_e}{\partial {}^{\star}\boldsymbol{b}_e} : \frac{\partial {}^{\star}\boldsymbol{b}_e}{\partial \boldsymbol{L}_{\delta}^{T}} : \boldsymbol{L}_{\delta}^{T} \,, \qquad (4.41)
$$

with $\boldsymbol{M}_{ep}$ given by

$$
\boldsymbol{M}_{ep} \;=\; f_1 b_1{}^{\star}\boldsymbol{N} \;+\; f_2\boldsymbol{I} \,, \qquad (4.42)
$$

where f_1 and f_2 read

$$
f_1 \;=\; h_z \;+\; \Delta\gamma \left(\left\langle 1 + A\,\frac{\hat{\tau}_h}{\hat{\tau}_{eq}} \right\rangle B\,\varepsilon_p^{B-1} \;-\; \left\langle 1 + A\,\frac{\hat{\tau}_h}{\hat{\tau}_{eq}} \right\rangle' A\,\frac{\hat{\tau}_h}{\hat{\tau}_{eq}^2}\varepsilon_p^{B}h_{\varepsilon} \right)
$$
$$
f_2 \;=\; \left\langle 1 + A\,\frac{\hat{\tau}_h}{\hat{\tau}_{eq}} \right\rangle' \frac{\Delta\gamma}{3}\,A\frac{\varepsilon_p^{B}}{\hat{\tau}_{eq}} \qquad\qquad (4.43)
$$

and $\langle\cdot\rangle'$ denotes the derivative of $\langle\cdot\rangle$, i.e. the Heaviside function. Since there is no dependence of δz on its nonlocal counterpart $\delta\bar{z}$, damage does not appear in any of the terms involved (as was the case in [50]). The final expression is obtained after substitution of Eqs. (4.41-4.43) in Eq. (4.40)

$$
\int_{\Omega} \left[\left(w_{\bar{z}}\,\bar{z} + \ell^2\,\vec{\nabla}w_{\bar{z}} \cdot \vec{\nabla}\bar{z} - w_{\bar{z}}\,z \right) \boldsymbol{I} - \ell^2\vec{\nabla}w_{\bar{z}}\otimes\vec{\nabla}\bar{z} : 2\,{}^{4}\boldsymbol{I}^{s} \right] : \boldsymbol{L}_{\delta}^{T}\,d\Omega
$$
$$
- \int_{\Omega} w_{\bar{z}}\,\boldsymbol{M}_{ep} : \frac{\partial \ln{}^{\star}\boldsymbol{b}_e}{\partial {}^{\star}\boldsymbol{b}_e} : \frac{\partial {}^{\star}\boldsymbol{b}_e}{\partial \boldsymbol{L}_{\delta}^{T}} : \boldsymbol{L}_{\delta}^{T}\,d\Omega + \int_{\Omega} \left[w_{\bar{z}}\,\delta\bar{z} + \ell^2\,\vec{\nabla}w_{\bar{z}} \cdot \vec{\nabla}\delta\bar{z} \right] d\Omega \;=\; \quad (4.44)
$$
$$
- \int_{\Omega} \left[w_{\bar{z}}\,\bar{z} + \ell^2\,\vec{\nabla}w_{\bar{z}} \cdot \vec{\nabla}\bar{z} \;-\; w_{\bar{z}}\,z \right] d\Omega \,.
$$

4.4.3   Finite element discretisation

Using a Galerkin finite element discretisation, the linearised system of Eqs. (4.38) and (4.44) is transformed into a set of linear algebraic equations. In the present chapter a quadratic serendipity finite element discretisation is used for the displacement field $\vec{u}$ and a bilinear discretisation for the nonlocal variable $\bar{z}$. The discretisations of

the weighting functions $\vec{w}$ and w correspond to those of $\vec{u}$ and $\bar{z}$ respectively. Substituting these interpolated fields and condensing the tensor products in Eqs. (4.38) and (4.44) into a matrix form results in the linear system

$$\underline{K}^{(i)}\,\delta\underline{a} \;=\; \underset{\sim}{f}_{\text{ext}} - \underset{\sim}{f}_{\text{int}}^{(i)}\,, \tag{4.45}$$

where $\delta\underline{a}$ contains the nodal values of the displacement variations $\delta\underline{u}$ an the variations $\delta\bar{\underline{z}}$. The stiffness matrix $\underline{K}^{(i)}$ contains four sub-matrices and the column of internal forces $\underset{\sim}{f}_{\text{int}}^{(i)}$ two subcolumns associated with the nodal degrees of freedom $\delta\underline{u}$ and $\delta\bar{\underline{z}}$:

$$\underline{K}^{(i)} \;=\; \begin{bmatrix} \underline{K}_{uu}^{(i)} & \underline{K}_{u\bar{z}}^{(i)} \\ \underline{K}_{\bar{z}u}^{(i)} & \underline{K}_{\bar{z}\bar{z}}^{(i)} \end{bmatrix} \quad \delta\underline{a} = \begin{bmatrix} \delta\underline{u} \\ \delta\bar{\underline{z}} \end{bmatrix} \quad \underset{\sim}{f}_{\text{ext}} = \begin{bmatrix} \underset{\sim}{f}_{u,\text{ext}} \\ \underline{0} \end{bmatrix} \quad \underset{\sim}{f}_{\text{int}}^{(i)} = \begin{bmatrix} \underset{\sim}{f}_{u,\text{int}}^{(i)} \\ \underset{\sim}{f}_{\bar{z},\text{int}}^{(i)} \end{bmatrix} \tag{4.46}$$

$\underline{K}_{uu}^{(i)}$, $\underline{K}_{u\bar{z}}^{(i)}$, $\underset{\sim}{f}_{u,\text{ext}}$ and $\underset{\sim}{f}_{u,\text{int}}^{(i)}$ are the result of discretising (4.38), whereas $\underline{K}_{\bar{z}u}^{(i)}$, $\underline{K}_{\bar{z}\bar{z}}^{(i)}$ and $\underset{\sim}{f}_{\bar{z},\text{int}}^{(i)}$ follow from (4.44). The interested reader is referred to [50] for more details on the discretisation of the system.

Four integration points per element have been used; assuming reduced integration for the discretised form of Eq. (4.38), which precludes plastic locking.

4.4.4 Remeshing

Modelling realistic applications with a large strain softening material requires some degree of adaptivity of the finite element discretisation in order to prevent the elements from becoming excessively distorted and to capture the large strain gradients that appear in the localisation regions. The need for adaptivity is higher in the stages close to failure, when the strains and the strain gradients are more pronounced. Note that the used gradient enhancement, by controlling the evolution of the width of localisation bands, correctly captures a progressive localisation.

In the applications below, full remeshing is done regularly in order to provide the desired adaptivity. Remeshing is usually based on a certain criterion reflecting the element size and/or the shape quality. Some other criteria try to keep an element size factor within a certain tolerance; others are based on error estimators, which have been extended to nonlocal problems in recent years [36]. However, since formulating such rigorous criteria for the class of material models which we consider here is far from straightforward, and since remeshing is not the main interest in this chapter, a more pragmatic approach is adopted here, in which the desired element sizes are set a priori and remeshing is done after a fixed number of time steps. This strategy remains reasonable near failure, where remeshing will occur more frequently, since the time steps tend to be smaller to ensure convergence. Fig. 4.1 shows the beneficial influence of remeshing for a computation on an unnotched bar, which will be discussed in more detail in the next section. The left figure shows the mesh at the end of the computation upon remeshing during loading; the right figure has been obtained

by disabling remeshing during the analysis. This clearly leads to heavily distorted elements and a poor description of the problem geometry, and consequently to an inaccurate analysis.
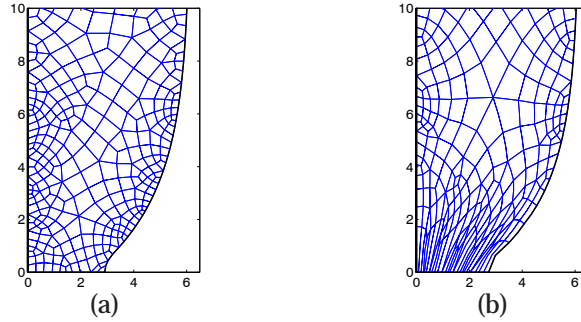

Figure 4.1 — *Final mesh at neck. (a) With remeshing, (b) without remeshing.*

An important issue to deal with upon remeshing, is the accuracy and robustness of the computations during the necessary transfer of state variables across meshes. Transfer causes diffusion errors and thereby loss of equilibrium and inconsistencies among state variables. The accuracy of the transferred state variables depends on the type of transfer operator and the choice of state variables which are transferred (see the discussions in Chapter 2 [82] and Chapter 3 [85]). Here, we have chosen to transfer the set $\{\tau, z, \tau_y, \omega_p\}$ and to reconstruct the other variables by enforcing the constitutive equations, which ensures a consistent transfer scheme.

To guarantee the robustness of the computations, an elastic equilibrium step is done after the transfer of variables. Since stresses are not bounded during this elastic step, the yield stress must be corrected upon convergence so that the loading-unloading conditions are met again. More details on these issues are given in Chapter 3 [85].

4.5   Applications

The performance of the triaxiality-dependent ductile damage model and its numerical implementation is illustrated below by a number of applications. First, we study the influence of hydrostatic pressure and elastic degradation under uniform straining. Simulations of more practical cases are presented towards the end of this section.

4.5.1   Evaluation of the constitutive response

To assess the relative influence of damage on the elastic and plastic behaviour, the case of uniaxial tension is first considered by directly evaluating the constitutive

response on a single element. The strain-hardening rate is given by

$$h_\varepsilon \;=\; h + \alpha \left(\tau_{y\infty} - \tau_{y0}\right) e^{-\alpha\,\varepsilon_p}\,. \tag{4.47}$$

The material parameters used in this analysis were taken from [50], except for the parameters A and B of Goijaerts's model which can be found in [55]. These values have been represented in Table 4.1.

Table 4.1 — *Material properties used in the uniform tension analyses and for the unnotched specimen (Sections 4.5.1 to 4.5.4).*

Shear modulus G	80.19 GPa
Bulk modulus K	164.21 GPa
Initial flow stress τ_{y0}	0.45 GPa
Residual flow stress $\tau_{y\infty}$	0.715 GPa
Linear hardening coefficient h	0.129 GPa
Saturation exponent α	16.93
Damage initiation threshold κ_i	0.05
Critical value of history parameter κ_c	1.5
Intrinsic length ℓ	1.0 mm
Damage parameter A	3.9
Damage parameter B	0.63

Fig. 4.2 represents the axial stress-strain curves of the models with elastoplastic damage and with only plastic damage, i.e. with and without degradation of the elastic properties. It can be seen that there is very little difference between both models (Fig. 4.2 (a)). Only when the hardening is increased to an unrealistically high value, i.e. $h = E/10$, the difference between the two models become noticeable towards the end of the failure process. This trend can be understood by realising that for a given stress the two models show the same amount of plastic strain, and the difference in total strain is thus due to the different amounts of elastic strain due to the different effective stiffnesses. For realistic material parameters, however, the elastic strain is much smaller than the plastic strain and hardly no effect is therefore found. A high h/E ratio increases the relative contribution of elastic strain to the total strain and therefore makes the effect of elastic degradation more visible. This suggests that for reasonable values of the material parameters and for continuous loading the effect of damage on the elastic stiffness can be safely neglected. One should realise however, that in more practical, inhomogeneous situations a considerable part of the structure may be unloading and that the marked unloading differences may have a more pronounced effect on the overall response.
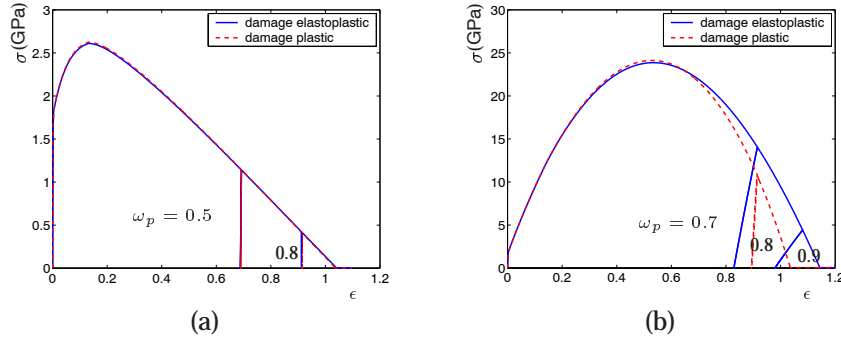
Figure 4.2 — *Plastic damage versus elastoplastic damage model (Goijaerts's evolution law): True stress (σ) - logarithmic strain (ϵ) in a tensile test. (a) Reference properties (according to Table 4.1), (b) excessive hardening ($h = E/10$).*

4.5.2 Behaviour in tension and compression

Evolution law (4.19) for the damage driving variable z has been constructed such that damage will grow in tension and under small compressive triaxiality states, i.e. for $\left|\frac{\tau_h}{\tau_{eq}}\right| < \frac{1}{A}$. For larger compressive hydrostatic stresses, i.e. $\left|\frac{\tau_h}{\tau_{eq}}\right| > \frac{1}{A}$, damage will not grow, and the material will thus continue to harden. Recovery of existing damage because of void closure [65, 102] is not modelled here.

The different behaviour between tension and compression is shown in Fig. 4.3 (solid curve), again for uniform deformation. The specimen is first stretched in tension, causing a certain degree of damage, after which it is loaded in compression, promoting strain hardening. The dashed curve in Fig. 4.3 represents a pressure-insensitive model, similar to the one used in [50], which is obtained by setting $A = 0$. In this case damage growth also takes place in compression and the stress response thus continues to soften in the compressive part of the loading.

4.5.3 Effect of hydrostatic stress

The ductility of a damaging metallic material can be strongly influenced by the action of an external pressure. A compressive hydrostatic pressure can postpone failure (increase in ductility), or even prevent it, if high enough. On the other hand, a tensile hydrostatic pressure will accelerate failure (decreasing ductility). This is a known effect which is sometimes used in industrial applications, e.g. in fine blanking. For example, in [55] a tensile test was performed on a steel bar immersed in oil, through which an external pressure was exerted. As a result, the specimen could accommodate more plastic straining before failure occurred. The damage driving relation (4.19) captures this effect.

In order to illustrate this, the tensile test discussed above is carried out in the
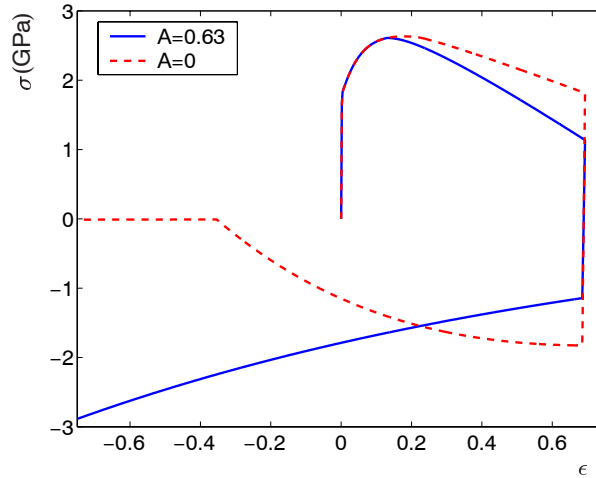
Figure 4.3 — *Behaviour in tension and compression for the triaxiality-dependent model ($A = 0.63$) and a triaxiality-independent variant ($A = 0$). True stress (σ) - logarithmic strain (ϵ).*

presence of an externally applied pressure or hydrostatic tension, for which different values are considered. The resulting stress-strain curves for different hydrostatic stress levels, negative and positive, are shown in Fig. 4.4. A positive (compressive) hydrostatic stress reduces the amount of softening (damage) as compared to the zero-pressure case, whereas a negative hydrostatic stress (tension) accelerates failure. For a high pressure the damage is eliminated completely and no softening is thus observed.

4.5.4   Unnotched tensile specimen

A well-known benchmark simulation consists of an axisymmetric cylindrical bar which is pulled while its ends are fixed transversally, hence resulting in necking at the middle section [50, 117], see Fig. 4.5 (a). The material properties used in this analysis are those of Table 4.1.

The specimen has a diameter $d = 12.8$ mm and a length $l = 53.3$ mm (Fig. 4.5 (a)). Because of the symmetries only one quarter of a cross section along the axis is modelled. The simulations are displacement driven, with u (Fig. 4.5 (a)) denoting the vertical imposed displacement on the specimen end (half of the total elongation). The initial mesh has been plotted in Fig. 4.5 (b), and the meshes at the onset of failure ($\omega_p = 1$) in Fig. 4.5 (c) and Fig. 4.5 (d), for the triaxiality-dependent model and the triaxiality-independent model ($A = 0$) respectively. The need for remeshing is emphasised in order to maintain a good element shape during the deformation process, especially in the neck. Note that the triaxiality-dependent specimen stretches and
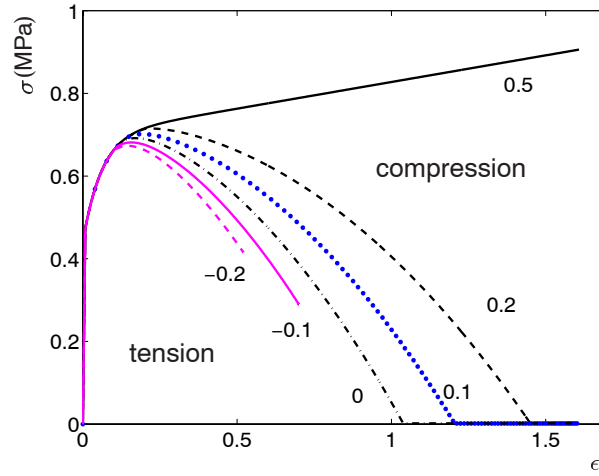
Figure 4.4 — *Influence of an externally applied pressure on the ductility. True nett stress (σ) - logarithmic strain (ϵ) in a tensile test.*

necks less than the triaxiality-independent specimen, because the hydrostatic tensile stress which arises when the neck develops results in faster damage growth and thus in earlier failure (see Fig. 4.6).

The evolution of damage for the cases $A = 3.9$ (triaxiality-dependent) and $A = 0$ (triaxiality-independent) is shown in Fig. 4.7. In both cases damage concentrates at the centre of the specimen (see [50]). Yet this effect is more pronounced for the triaxiality-dependent model, since it is sensitive to the high hydrostatic stress at the centre. This agrees with experimental observations which show that the ductile failure of unnotched bars starts at the centre [130]. Observe that when failure occurs in the pressure-sensitive model, the outer part of the neck has not failed yet and a residual strength thus still exists. Note also that in both analyses damage localises in a region which comprises several elements as a result of the gradient enhancement.

The overall response can be seen in the force-displacement curves of Fig. 4.8, which shows the results of the triaxiality-dependent model and an elastoplastic model (obtained by setting the threshold κ_i to a very high value). Since the results of the plastic and elastoplastic damage models are almost identical, only the latter are shown. It is evident that the damage model behaves less ductile than the elastoplastic material, which has no failure criterion and therefore fails only when the diameter at the neck becomes zero, see also [50].

The influence of the triaxiality-dependency parameter A in the damage growth relation (Eq. (4.19)) on the global response is shown in Fig. 4.9. The ductility is higher for smaller values of A, since the effect of the stress triaxiality on damage growth is smaller and the damage therefore grows slower.
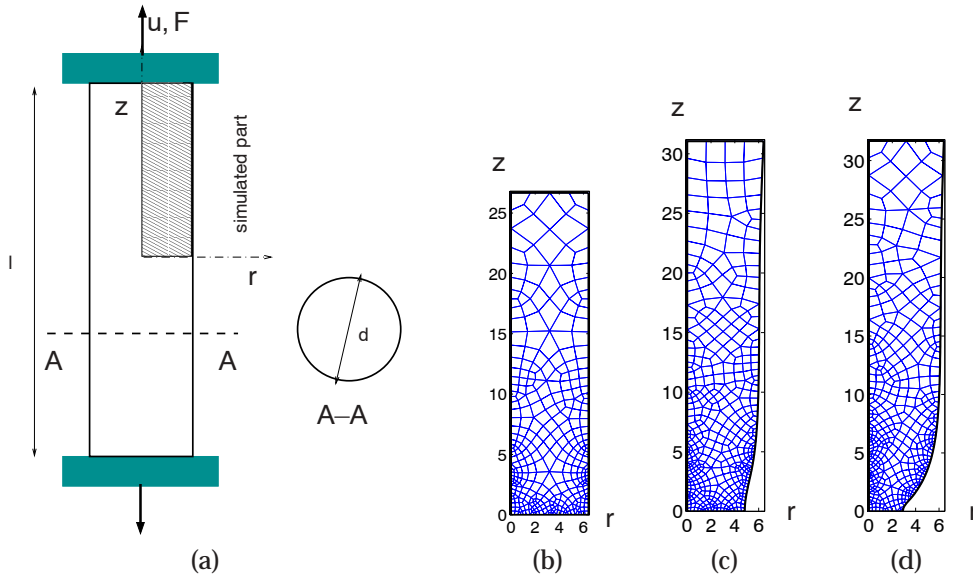
Figure 4.5 — *(a) Dimensions and boundary conditions, (b) initial mesh, final mesh for (c) triaxiality-dependent model and (d) triaxiality-independent model.*

4.5.5 Notched specimens

A relatively simple way to experimentally study the influence of the hydrostatic stress is by varying the notch radius of cylindrical notched tensile bars. Here we simulate the experiments performed by Hopperstad et al. [62] on notched axisymmetric specimens of the structural steel Weldox 460 E in a Split Hopkinson Device. The experiments confirmed that the ductility of the material depends on the degree of triaxiality, i.e. on the notch radius. Although the experiments were dynamic, the influence of the loading rate was moderate and hence quasi-static analyses, as we have performed, are justified.

The material parameters used in our analysis are given in Table 4.2. The elastic properties, i.e. Young's modulus and Poisson's ratio, were taken from the work of Børvik et al. in [26]. The hardening parameters were obtained from the same authors in [25], where a better agreement between simulations and experiments is found. The critical damage parameter κ_c and the internal length parameter were taken in a realistic range, thereby capturing the experimental trend. It has been assumed that damage growth starts after a threshold value $\kappa_i = 0.05$ of $\bar{z}$ is reached. The damage parameters A and B were taken from [55] for steel. The strain-hardening curve used in [26] has also been adopted here, i.e.

$$h_\varepsilon \;=\; n\,D\,\varepsilon_p^{n-1}\,. \tag{4.48}$$

The geometry and dimensions of the notched and smooth bars are shown in Fig.

$$\epsilon_o = 12\% \qquad \epsilon_o = 16\% \qquad \epsilon_o = 20\% \qquad \epsilon_o = 22\%$$
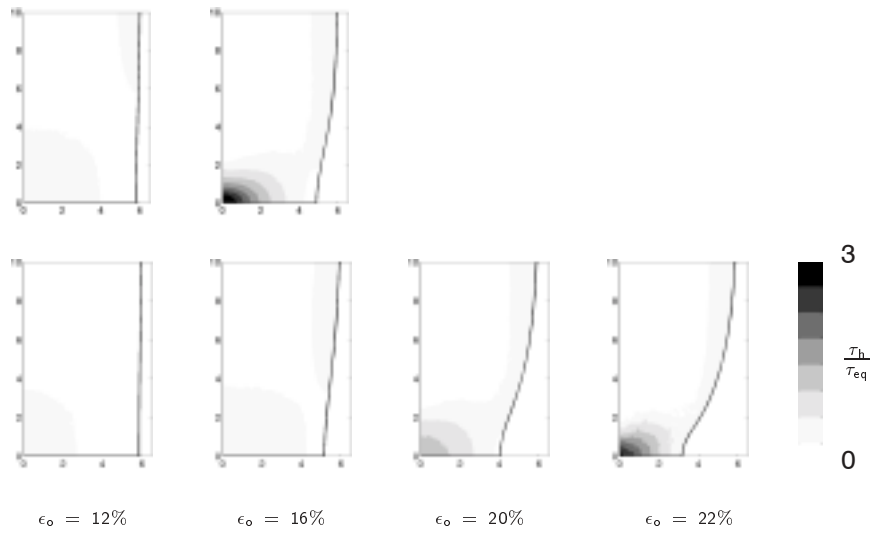
Figure 4.6 — *Triaxiality evolution ($\frac{\tau_h}{\tau_{eq}}$). (above) triaxiality-dependent (Goijaerts) model; (below) triaxiality-independent model ($A = 0$). ϵ_o denotes the elongation (engineering strain).*

$$\epsilon_o = 12\% \qquad \epsilon_o = 16\% \qquad \epsilon_o = 20\% \qquad \epsilon_o = 22\%$$
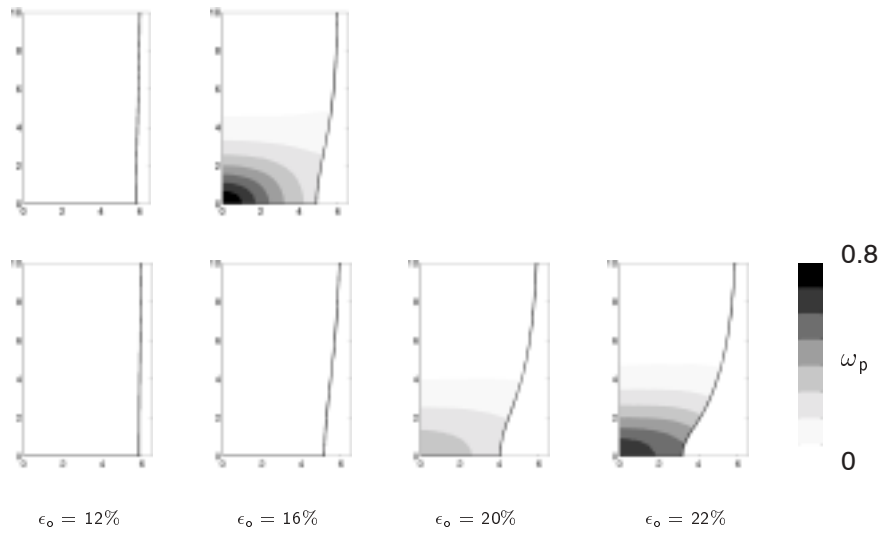
Figure 4.7 — *Damage evolution (ω_p). (above) triaxiality-dependent model; (below) triaxiality-independent model ($A = 0$). ϵ_o denotes the elongation (engineering strain).*
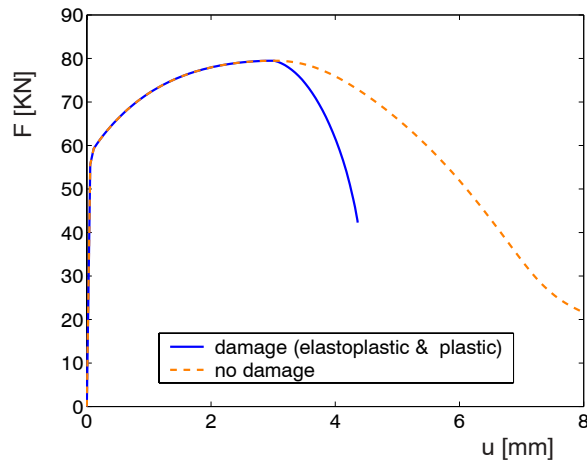
Figure 4.8 — *Force-displacement curves. Damage (plastic and elastoplastic) model versus elastoplastic model.*
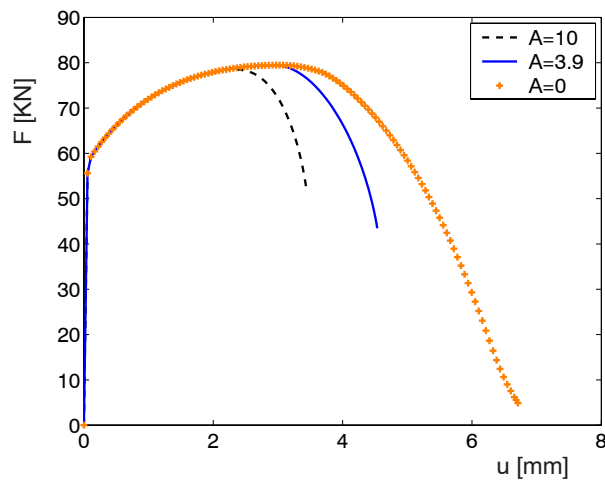
Figure 4.9 — *Force-displacement curves. Influence of pressure sensitivity A.*

4.10, with dimensions in *mm*. The notched specimens have radii (R) of 0.4, 0.8 and 2 mm. One quarter of the cross-section of each bar is modelled because of symmetry and axi-symmetry. The initial meshes used in the simulations have been plotted in Fig. 4.11. Finer elements are used at the notch, where higher strains will concentrate, whereas coarser elements are placed at the top. Fig. 4.12 shows the final meshes at the onset of failure ($\omega_p = 1$). Remeshing regularly has kept the meshes well shaped.

Table 4.2 — *Material parameters for notched axisymmetric cylindrical bars [25].*

Shear modulus G	75.19 GPa
Bulk modulus K	196.1 GPa
Initial flow stress τ_{y0}	0.49 GPa
Hardening parameter D	0.807 GPa
Hardening exponent n	0.73 -
Damage initiation threshold κ_i	0.05
Critical value of history parameter κ_c	5
Internal length ℓ	0.2 mm
Damage parameter A	3.9
Damage parameter B	0.63

Note that the shape of the neck in the smooth specimen is different from that in the other specimens.
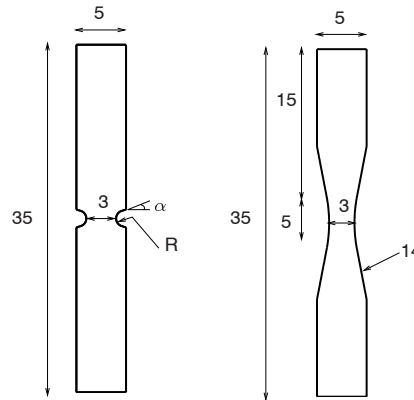
Figure 4.10 — *Geometry and dimensions of notched (left) and smooth specimens (right). $\alpha = 17.5^o$ for all radii, except for R $= 2$ mm, where $\alpha = 0^o$ [25].*

The force-elongation curves obtained in the simulations have been plotted in Fig. 4.13 (a), together with the experimental data reported in Refs. [62] and [26] (Fig. 4.13 (b)). The two sets of curves show the same trend, i.e. specimens with smaller notch radii are stronger (higher peak force) and more brittle (less elongation at failure) than those with larger notch radii. The measured forces are nevertheless higher than the simulated strengths. Improvements are expected if the material parameters used from [26] and [25] are corrected, since these estimates did not account for the influence of damage. This quantitative correction, however, is beyond the scope of this analysis, since more local details on the experimental measurements would therefore be required.
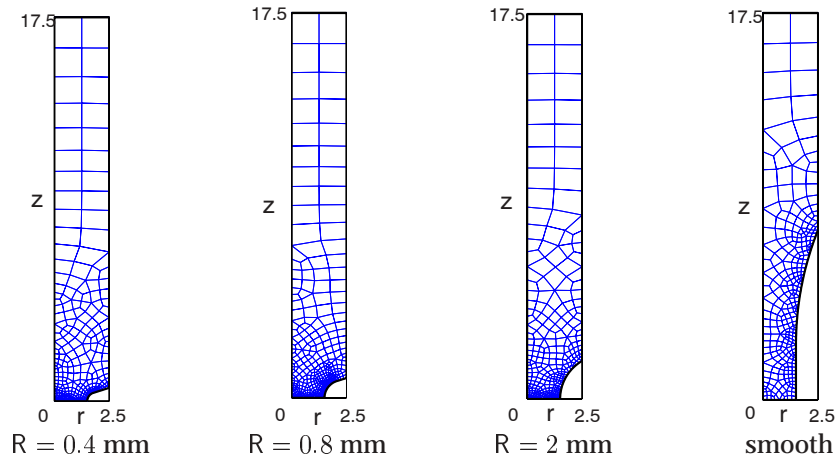
Figure 4.11 — *Initial mesh for each of the four geometries.*
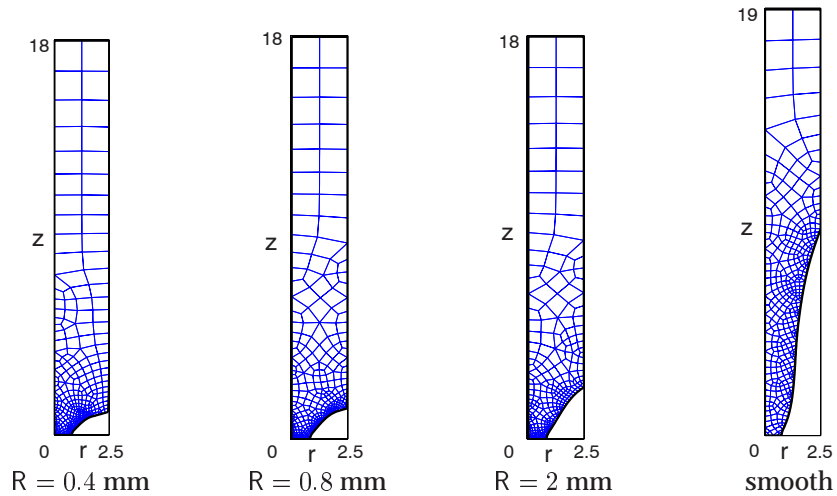
Figure 4.12 — *Final mesh for each of the four geometries.*

The role that the triaxiality plays in the evolution of ductile failure can be seen in Fig. 4.14, where the force-elongation curve of the triaxiality-dependent damage evolution has been plotted together with the triaxiality-independent evolution ($A = 0$) and the plasticity model without any damage for the smooth and the R $= 0.4$ specimens. As we have seen above, the lack of triaxiality in the failure criterion artificially increases the material ductility. This is even more true if no damage influence
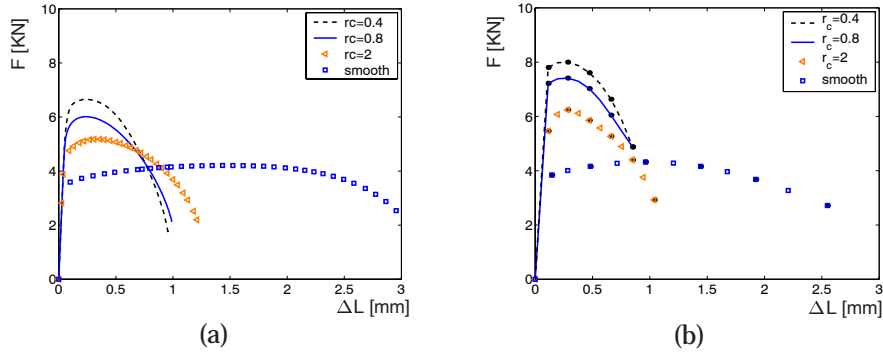
Figure 4.13 — *Force-elongation curves. (a) Simulations, (b) experiments. Hopperstad et al. [62] and Børvik et al. [26].*

is included at all. In the latter case, the necking continues right until the smallest diameter of the specimen equals zero and the specimen therefore cannot sustain any load. The analyses in which damage is taken into account, and particularly the case where the damage growth depends on the stress triaxiality, have ended at an earlier stage, because the damage variable reached the critical value $\omega_p = 1$ somewhere in the specimen and failure (or at least crack initiation) was thus predicted. Note that the differences between the case of necking with or without damage are merely local in the necking area, leading to completely different fracture surfaces. This is of course not revealed in the global curves shown in Fig. 4.14.
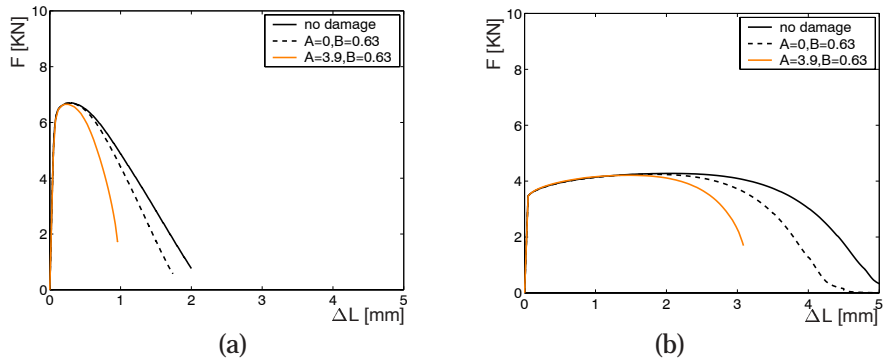
Figure 4.14 — *Force-elongation curves for (a) small notch (R = 0.4) and (b) smooth specimens. Three cases are considered: No damage; triaxiality insensitive damage, i.e. $A = 0$, and triaxiality sensitive damage (Goijaerts).*

Experimental data shows that failure of the specimens with small notch radii may fail from the notch edge or at the centre [2]. We will now examine in detail if the damage formulation captures these two different failure mechanisms for the specimen with the smallest notch radius.

Fig. 4.15 shows the evolution of damage, equivalent plastic strain and hydrostatic stress versus the elongation of the specimen for the small notch specimen ($R = 0.4$), using the triaxiality dependent model. Initially, the model predicts higher damage at the neck edge, which is later overtaken by the faster damage growth at the centre, where eventually the specimen will fail. This is because at the beginning the higher plastic strain at the edge is more dominant than the higher triaxiality at the centre. But, as damage grows the specimen necks, which increases the triaxiality, especially at the centre. This is a self accelerating process, i.e. an increase in damage reduces the shear stress component (J_2 plasticity), which increases the triaxiality, and hence damage increases again, leading to a rapid hydrostatic stress growth. The hydrostatic stress, although it grows, remains relatively low. It can be concluded that for the small notch specimen, failure of the specimen depends on a competition between the high triaxiality at the centre and the high plastic strains at the specimen edge. Depending on type of material, i.e. damage evolution, failure will occur in one place or the other.

Fig. 4.16 shows that by adapting the damage parameters (i.e. the material), the outcome of this competition can be changed. In the analysis represented in this figure, the parameter B of the damage evolution was set to $B = 4$. The plastic strain-induced damage growth at the edge then leads to failure before the hydrostatic stress at the center. This triaxiality-dependent model is thus able to capture the transition from failure at the centre to failure at the edge.

4.6   Conclusion

The main objective of this chapter was to extend the gradient-enhanced damage-plasticity framework developed by Geers et al. [50] towards more realistic damage growth relations which take into account the influence of hydrostatic stress on ductile damage. The simulation results shown in Section 4.5 demonstrate that the resulting model is indeed able to pick up experimentally observed effects. Most notably, the new, triaxiality-dependent modelling allows to capture the correct crack initiation in notched an unnotched bars. Industrially relevant applications in which the effect of triaxiality is even more pronounced will be reported in future work.

In the process of formulating the new coupled damage-elastoplasticity model, the effective stress concept together with the principle of strain equivalence lead to a damage-induced reduction of the local elastic stiffness as well as the yield stress. This is different from the plastic degradation model used in [50], in which only the yield stress is degraded. However, our analyses show that differences in the responses of the two models can only be distinguished for unrealistic parameter sets. For realistic values the elastic strains are always small compared with the elastic strain and the

overall difference in terms of the resulting stiffness remains insignificant. In terms of numerical implementation, the two formulations have a comparable structure and simplicity – although the one presented here has the advantage of not affecting the return-mapping of the underlying plasticity theory.

The present extension of the gradient-enhancement formulation introduced by Geers in [50] has been shown to also work properly with a triaxiality-dependent damage driving variable. Mesh-insensitive results are obtained as long as elements in the fracture process zone are smaller than the internal length scale ℓ introduced by the nonlocality. An adaptive mesher has been used to ensure this. As to the value of the length scale, and the physical motivation of the nonlocality, some quantification questions remain. The nonlocality must clearly be the result of void interaction and ℓ must thus be of the order of the typical void spacing. However, a rigorous quantitative link between the voided microstructure of the material and the nonlocality introduced by Eq. (4.17) has not yet been established. It is believed that developing a link and further understanding the interplay of voids, and the surrounding matrix material is still a challenging area of research, with many potential applications.
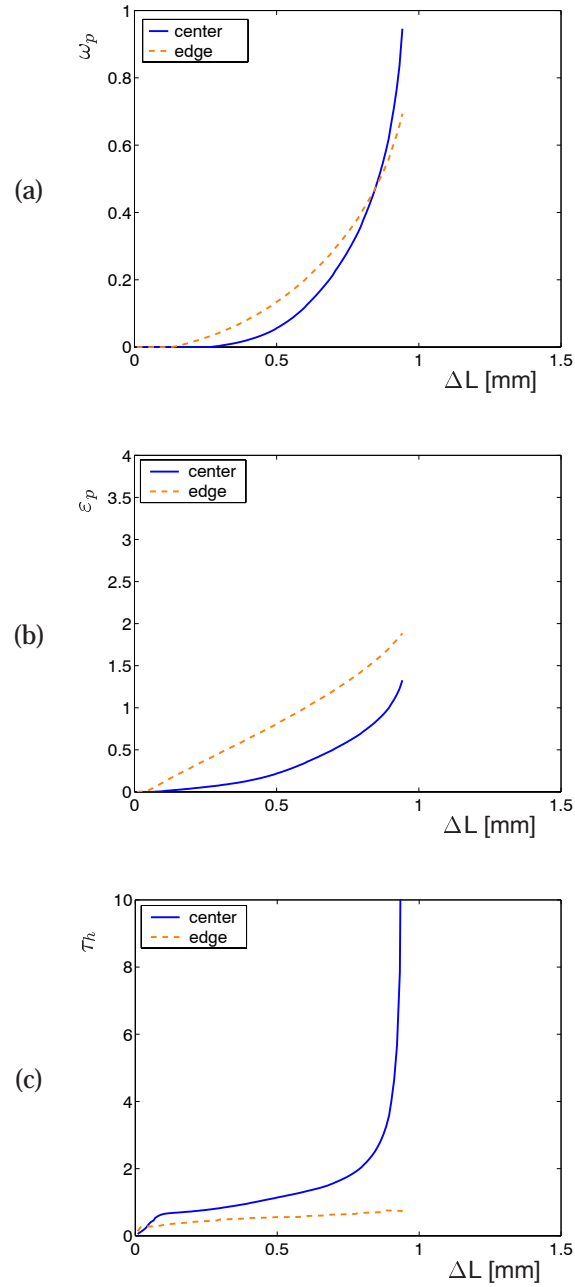
Figure 4.15 — *Small notch specimen (R = 0.4): Evolution of state variables at the notch centre and edge for different elongations, using the triaxiality-dependent model (Goijaerts). (a) Damage ω_p, (b) effective plastic strain ε_p, (c) hydrostatic stress τ_h.*
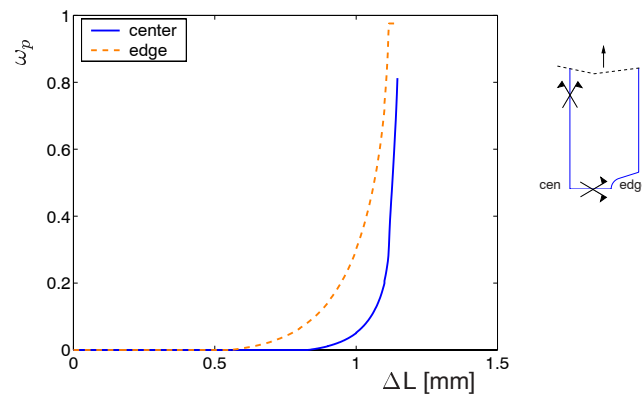
Figure 4.16 — *Influence of the damage evolution parameters in the location of failure, $B = 4$. Small notch specimen ($R = 0.4$). Evolution of damage variable at the notch centre and edge versus elongation, for triaxiality-dependent model ($A = 0.63$).*

Chapter 5

An integrated continuous-discontinuous approach towards damage engineering in metal forming processes [4]

Abstract: This chapter addresses the simulation of ductile damage and fracture in metal forming processes. A combined continuous-discontinuous approach has been used, which accounts for the interaction between macroscopic cracks and the surrounding softening material. Softening originates from the degradation processes taking place at a microscopic level, and is modelled using continuum damage mechanics concepts. To avoid pathological localisation and mesh dependence and to incorporate length scale effects due to microstructure evolution, the damage growth is driven by a nonlocal variable via a second order partial differential equation. The two governing equations, i.e. equilibrium and nonlocal averaging, are solved in an operator-split manner. This allows one to use a commercial finite element software to solve the equilibrium problem, including contact between the tools and work piece. The nonlocal averaging equation is solved on a fixed configuration, through a special purpose code which interacts with the commercial code. A remeshing strategy has been devised that allows: (i) to capture the localisation zone, (ii) prevent large element distortions and (iii) accommodate the crack propagation. To illustrate the capabilities of the modelling tool obtained by combining these continuum mechanics concepts and computational techniques, process simulations of blanking, fine blanking and score-forming are presented.

---

[4]This chapter is based on [84].

5.1 Introduction

Many products are manufactured by processes which involve material separation, e.g. blanking and machining. The material is separated by triggering macroscopic cracks. When and where cracks originate, and which trajectory they follow thus determines the shape and quality of the final product. Computational tools which can predict the formation and evolution of cracks are valuable in optimising such processes, since they may result in considerable cost and time savings. Controlling the development of damage and cracks in this way is sometimes termed damage engineering.

Before the appearance of a macroscopically observable crack, ductile materials manifest a gradual loss of their load-carrying capacity (strain-softening), caused by the nucleation and growth of voids at inclusions in the material matrix. This leads to localisation and eventually to failure, accompanied by fully developed cracks. From a continuum mechanics point of view, crack propagation and material degradation have traditionally been studied separately. The first has been the subject of fracture mechanics [5], whereas the second is mostly based either on microscopical considerations [56, 129], or phenomenological descriptions as continuum damage mechanics [65, 74].

To model the complete evolution, from the initiation of damage to crack propagation, a continuous regularised softening model and a strategy to model cracks must be combined in a coupled continuous-discontinuous approach. In this combined approach, crack growth is the ultimate consequence of the degradation and softening in a process zone ahead of the crack.

A complication in the continuum part of the description is that the strain-softening occurring in local variants of these models may lead to pathological localisation and strongly mesh dependent numerical results. To avoid these effects, regularising techniques must be applied, i.e. gradient enhanced models, nonlocal theories, rate dependent or micropolar continua [41]. Here we use an implicit gradient model, which is strongly nonlocal, and can be implemented with relative ease as a localisation limiter in finite element implementations of ductile damage [50]. The nonlocality provides an internal length to the model, which links the macroscopic and microscopic levels.

Several numerical techniques are available to model discrete cracks in a finite element mesh, e.g. remeshing [133], partition of unity methods [15], embedded discontinuity techniques [120], element erosion, etc. Although remeshing is quite expensive, it has a number of additional advantages in a large strain setting with localised deformations: (i) it allows to control element distortion, which is crucial in metal forming; and (ii) mesh refinement can be applied to capture the large strain gradients in localising regions and nearby cracks.

This work aims to enable the application of the combined approach developed in Chapter 3 [85] to the modelling of ductile fracture in metal forming processes. During localisation, mesh independent results are guaranteed by means of an implicit gradient enhancement, in line with [45, 50, 53]. The two factors which drive ductile

damage, i.e. triaxiality and plastic strain, are both taken into account in determining the growth of a damage variable. The effect of damage on the elastic properties and on the yield behaviour is introduced by making use of the effective stress concept. The two governing partial differential equations, i.e. equilibrium and the averaging equation associated with the gradient enhancement, are solved in an operator-split manner, as it was first done in [23]: a fixed-damage equilibrium step, followed by a damage evolution step at a fixed (converged) configuration. This is in contrast with Chapter 3 and [45, 53, 85], where a monolithic strategy was followed. The present operator-split algorithm is only conditionally stable, but is easier to implement, particularly in combination with existing forming codes. Indeed, in this chapter we use a commercial software (i.e. MSC.MARC) for the equilibrium problem, including contact. The averaging equation is solved by a special purpose code on the basis of the plastic deformation and stress fields delivered by the commercial finite element software. This code returns the updated (damaged) material properties to the commercial code. Remeshing and transfer of state variables are also dealt with outside the standard finite element software. To capture the localisation process, a simple mesh adaptivity criterion is proposed which is based on the damage growth. The resulting remeshing strategy can simultaneously accommodate the geometry of advancing cracks and limits element distortion. The simulation tool which is thus obtained is applied to blanking, fine-blanking and score forming processes, which all involve contact with the tools, softening, large localised deformations and fracture.

The structure of this chapter is as follows. In Section 5.2 the material model is briefly described. Starting from the elastoplastic undamaged material, the damaged response is obtaining by making use of the concept of effective stress and the principle of strain equivalence. The local and nonlocal damage driving variables are introduced in Section 5.2.1. The operator-split treatment of the coupled problem and its finite element implementation are discussed in Section 5.3. The crack initiation-propagation strategy is presented in Section 5.4. In this Section, particular attention is given to the damage rate based mesh adaptivity criterion. Simulations of blanking, fine blanking and score forming process are shown in Section 5.5, and conclusions are drawn in Section 5.6.

5.2 Gradient damage extension of an existing hypoelasto-plasticity model

Using an isotropic continuum mechanics framework, the degradation of the mechanical material properties is here represented by a single scalar damage variable ω_p ($0 \leq \omega_p \leq 1$) [65, 73], where $\omega_p = 0$ and $\omega_p = 1$ represent the undamaged and fully damaged states respectively. If this damage variable is interpreted as the area occupied by voids and cracks divided by the total area of an elementary surface, the stress acting on the undamaged part of this cross-section can be characterised by the

effective stress tensor $\hat{\sigma}$, defined in terms of the overall stress tensor σ as [73]

$$\hat{\sigma} \ = \ \frac{\sigma}{(1 - \omega_p)} \, . \tag{5.1}$$

Effective quantities and material properties, i.e. properties of the nett material volume, without cracks or voids, are denoted by $(\hat{\cdot})$. The effect of damage on the constitutive response of a material can now be incorporated by replacing the stress tensor in the standard constitutive model by its value of the undamaged material, $\hat{\sigma}$, i.e. through expression (5.1). The effect of this operation on an elastoplasticity model is a reduction of the apparent yield stress as well as of the elastic (unloading) stiffness due to the damage influence (Chapter 4 [83]).

To describe the behaviour of the effective material matrix, a standard J_2 hypoelastoplasticity model as implemented in MSC.MARC [70, 87] has been used. The governing equations of the matrix model have been summarised in Table 5.1. In this

Table 5.1 — *Matrix material: hypoelastoplastic model (MSC.MARC).*

i	Additive split of the rate of deformation tensor
	$\boldsymbol{D} = \boldsymbol{D_e} + \boldsymbol{D_p}$
ii	Hypoelastic response
	$\overset{\circ}{\hat{\boldsymbol{\sigma}}} \ = \ {}^4\hat{\boldsymbol{C}}_{\boldsymbol{e}} : \boldsymbol{D_e} \ = \ {}^4\hat{\boldsymbol{C}}_{\boldsymbol{e}} : (\boldsymbol{D} - \boldsymbol{D}_p)$
iii	Yield function
	$\hat{\phi}(\hat{\boldsymbol{\sigma}}, \varepsilon_p) \equiv \hat{\sigma}_{eq}^2 - \hat{\sigma}_y^2$
iv	Loading-unloading conditions
	$\dot{\varepsilon}_p \geq 0, \qquad \hat{\phi} \leq 0, \qquad \dot{\varepsilon}_p \hat{\phi} = 0$
v	Hardening evolution
	$\hat{\sigma}_y \ = \ \hat{\sigma}_y(\varepsilon_p)$
vi	Flow rule
	$\boldsymbol{D}_p = \frac{3}{2} \dot{\varepsilon}_p \frac{\hat{\boldsymbol{\sigma}}^d}{\hat{\sigma}_{eq}}$
vii	Evolution of the effective plastic strain (ε_p)
	$\dot{\varepsilon}_p \ = \ \sqrt{\frac{2}{3} \boldsymbol{D_p} : \boldsymbol{D}_p}$

table ${}^4\hat{\boldsymbol{C}}_e$ is the standard elasticity tensor from linear elasticity,

$$^4\hat{\boldsymbol{C}}_{\boldsymbol{e}} \ = \ \hat{\lambda}\,\boldsymbol{I} \otimes \boldsymbol{I} + 2\hat{\mu}\,{}^4\boldsymbol{I}^s \tag{5.2}$$

and $\hat{\lambda}$ and $\hat{\mu}$ denote the Lamé constants of the undamaged (effective) material. $(\overset{\circ}{\cdot})$ denotes the Jaumann objective rate and $\hat{\sigma}_{eq}$ is the equivalent von-Mises stress, $\hat{\sigma}_{eq} \equiv \sqrt{\frac{3}{2}\hat{\boldsymbol{\sigma}}^d : \hat{\boldsymbol{\sigma}}^d}$.

Using the effective stress-elastic strain relation (Table 5.1 (ii)) and Eq. (5.1), the

homogenised elastic response can be expressed as

$$\overset{\circ}{\boldsymbol{\sigma}} = (1 - \omega_p)^4 \hat{\boldsymbol{C}}_e : \boldsymbol{D_e} - \frac{\dot{\omega}_p}{1 - \omega_p} \boldsymbol{\sigma} . \tag{5.3}$$

The yield function of the elastoplastic undamaged material (Table 5.1 (iii)) can similarly be rewritten as

$$\phi(\boldsymbol{\sigma}, \varepsilon_p, \omega_p) = \sigma_{eq}^2 - (1 - \omega_p)^2 \hat{\sigma}_y^2(\varepsilon_p) \leq 0 , \tag{5.4}$$

with

$$\phi = (1 - \omega_p)^2 \hat{\phi} . \tag{5.5}$$

The flow rule (Table 5.1 (iv)) can be expressed in the overall stress space or in the effective stress space, since

$$\frac{\partial \hat{\phi}}{\partial \hat{\boldsymbol{\sigma}}} = \frac{\hat{\boldsymbol{\sigma}}^d}{\hat{\sigma}_{eq}} = \frac{\partial \phi}{\partial \boldsymbol{\sigma}} = \frac{\boldsymbol{\sigma}^d}{\sigma_{eq}} . \tag{5.6}$$

5.2.1 Damage growth

The damage evolution equation in rate form reads

$$\dot{\omega}_p = h_\omega \dot{\kappa} , \tag{5.7}$$

where h_ω may generally depend on the damage variable ω_p and on the history variables κ. In order to retrieve a similar expression for the damage evolution as was used in [55] (see below in (5.12)), a piecewise constant h_ω must be used

$$h_\omega = \begin{cases} \frac{1}{\kappa_c - \kappa_i} & \text{if} \quad \kappa_i \leq \kappa \leq \kappa_c \\ 0 & \text{otherwise.} \end{cases} \tag{5.8}$$

The evolution of κ is related to a nonlocal damage driving variable $\bar{z}$ via the Kuhn-Tucker loading-unloading conditions

$$\dot{\kappa} \geq 0, \qquad \bar{z} - \kappa \leq 0, \qquad \dot{\kappa} (\bar{z} - \kappa) = 0 \tag{5.9}$$

and the initial value $\kappa_{(t=0)} = \kappa_i$.

$\bar{z}$ is obtained by solving a Helmholtz partial differential equation, formulated in the deformed (Eulerian) configuration (Chapter 3, [45, 50, 53, 85])

$$\bar{z} - \ell^2 \nabla^2 \bar{z} = z . \tag{5.10}$$

where ∇^2 denotes the Laplacian operator. z is a local damage driving variable which acts as source term in (5.10). ℓ is an internal length parameter which sets the width

of localisation zones and which is related to the material microstructure, e.g. the average void spacing. It has been demonstrated in [99] that the above partial differential equation (5.10) is strongly nonlocal, in the sense that the behaviour at a point depends on the response in a finite neighbourhood of the point. An advantage of the incorporation of nonlocality according to (5.10) compared to integral nonlocal constitutive relations (computed from weighted spatial averages), is that in the present formulation only an additional partial differential equation needs to be solved – an operation which can be done relatively easily in a finite element setting. Note that the Eulerian formulation selected here (see [53] for a comparison with a Lagrangian form) permits to pose the problem in terms of variables defined on the current configuration, which is more convenient from the point of view of remeshing (Chapter 3, [85]).

Eq. (5.10) is complemented by the homogeneous Neumann boundary condition

$$\vec{\nabla}\bar{z} \cdot \vec{n} \; = \; 0 \,, \tag{5.11}$$

with $\vec{n}$ being the boundary normal. This condition must be applied not only at the external boundaries of the continuum, but also at the newly generated crack faces.

In References [45, 50, 53] the local damage driving variable z was taken equal to the effective plastic strain ε_p. This is a reasonable assumption in shear-dominated problems, where there is little void growth. However, in cases where there is a significant hydrostatic stress component, the influence of this hydrostatic stress – particularly when it is tensile – on damage growth cannot be neglected. This influence can be taken into account, as proposed in Chapter 4 [83], by defining z according to the evolution law

$$\dot{z} \; = \; \left\langle 1 \, + \, A \, \frac{\tau_h}{\tau_{eq}} \right\rangle \varepsilon_p^B \, \dot{\varepsilon}_p \,, \tag{5.12}$$

taken from Goijaerts et al. [55]. In (5.12) the angular brackets $<\;>$ are the Macaulay brackets, i.e. $< x > = (\, x + |x|\,)/2$. Initially z can be set to zero. For low triaxialities, i.e. $\frac{\tau_h}{\tau_{eq}} \ll 1$, the growth of z and thus of damage is mainly governed by the amount of plastic straining. High triaxialities, however, promote damage growth, as confirmed in experiments [79], where voids grow faster under hydrostatic tension, promoting fracture at a smaller strain. Under large compressive triaxiality states, i.e. $\left|\frac{\tau_h}{\tau_{eq}}\right| > \frac{1}{A}$, damage growth is inhibited.

5.3   Operator-split implementation

The model described in Section 5.2 is governed by two partial differential equations, i.e. equilibrium and the nonlocal equation (5.10):

$$\boxed{\begin{aligned} \vec{\nabla} \cdot \boldsymbol{\sigma} \; &= \; \vec{0} \\[2mm] \bar{z} - \ell^2 \, \nabla^2 \bar{z} \; &= \; z \end{aligned}} \tag{5.13}$$

Together with the boundary conditions

$$
\begin{aligned}
\boldsymbol{\sigma} \cdot \vec{n}|_{\Gamma_p} &= \vec{p} \\
\vec{u}|_{\Gamma_u} &= \vec{u}^o \\
\vec{\nabla}\bar{\mathsf{z}} \cdot \vec{n}|_{\Gamma} &= 0
\end{aligned}
\tag{5.14}
$$

(where $\vec{p}$ represents the prescribed tractions on the boundary Γ_p, $\vec{u}^o$ are the displacements imposed on the boundary Γ_u and Eq. (5.11) is defined on $\Gamma = \Gamma_u \cup \Gamma_p$) and the initial conditions for the displacement $\vec{u}$ and for $\bar{\mathsf{z}}$, these partial differential equations define an initial boundary value problem (IBVP) in the space-time domain $\Omega \times [0, T]$. In References [45, 53], a monolithic solution algorithm was developed for the fully coupled problem, albeit using a slightly different, hyperelastoplastic model. Here, we develop an operator-split (incrementally staggered) approach, which consists in incrementally splitting the coupled problem into two sub-problems, namely (1) the equilibrium problem with a fixed nonlocal variable $\bar{\mathsf{z}}$ and hence a fixed damage field ("fixed-damage equilibrium step") and (2) the nonlocal problem (5.10) on a fixed spatial configuration. The main advantages of this approach are:

(i)   It allows to couple the gradient enhanced damage framework to existing finite element codes in a transparent and convenient manner. As a result, existing plasticity models and contact algorithms remain readily applicable, without having to reimplement them.

(ii)   After linearisation, two symmetric problems are obtained, in contrast to the fully coupled problem where a coupled, non-symmetric tangent operator has been found [45].

(iii)   In the present set of equations, Equation (5.10) becomes a linear partial differential equation for a fixed configuration, which means that the problem can be solved directly, without the necessity of iterations.

The implementation follows the lines of Reference [119], where a coupled thermoplasticity problem was split into an isothermal equilibrium problem plus a heat transfer problem at fixed spatial configuration. Here, the role of the balance of energy equation is replaced by the nonlocal averaging equation (5.10). First step in setting up the algorithm is the time discretisation. Here we use a backward Euler rule to express the evolution during each increment $[t, t + \Delta t]$ in terms of the deformation map $\vec{x} = \vec{x}(\vec{X})$ and the nonlocal driving variable $\bar{\mathsf{z}}(\vec{x})$ at the start and the end of the increment; these fields are indicated by $\vec{x}^t, \bar{\mathsf{z}}^t$ and $\vec{x}, \bar{\mathsf{z}}$ respectively. For a known state $(\vec{x}^t, \bar{\mathsf{z}}^t)$ at the start of the increment, a coupled set of boundary value problems is thus obtained for time $t + \Delta t$.

The operator-split is now obtained by first solving the first of these boundary value problems, the equilibrium problem, for $\mathsf{z} = \mathsf{z}^t$. This results in a position field $\vec{x}$ which is then used to set up the second boundary value problem, based on Eq. (5.10). Note that the current position $\vec{x}$ enters this equation via the Laplacian ∇^2.

For fixed $\vec{x}$, this equation is now a linear partial differential equation which can be solved in a straightforward way for $\bar{z}$. The split can thus be represented as follows:

$$\underbrace{\begin{bmatrix} \vec{\nabla} \cdot \boldsymbol{\sigma} = \vec{0} \\ \bar{z} - \ell^2 \, \nabla^2 \bar{z} = z \end{bmatrix}}_{\text{BVP}} \simeq \underbrace{\begin{bmatrix} \vec{\nabla} \cdot \boldsymbol{\sigma} = \vec{0} \end{bmatrix}}_{\text{BVP}_1 \text{ (fixed } \bar{z})} + \underbrace{\begin{bmatrix} \bar{z} - \ell^2 \, \nabla^2 \bar{z} = z \end{bmatrix}}_{\text{BVP}_2 \text{ (fixed } \vec{x})} \tag{5.15}$$

As a result of the operator-split, the two solution fields $\vec{x}$ and $\bar{z}$ at $t + \Delta t$ will generally be slightly inconsistent. For small increments, however, these differences will be small and therefore quite acceptable. In contrast to the fully coupled approach, the operator-split approach is only conditionally stable. However, the nonlinearity in the equilibrium problem, the remeshing and the contact algorithm generally require such small time increments, that stability of the time integration is not considered to be a problematic issue.

5.3.1   Fixed-damage equilibrium step

The first, equilibrium boundary value problem, (BVP_1 in terms of Eq. (5.15)) is solved for $\bar{z}$ constant, as given by $\bar{z}^t$. The only way in which this field enters the equilibrium problem is via the damage variable ω_p, which is also constant for constant $\bar{z}$. This damage variable ω_p, which is thus set equal to ω_p^t in the equilibrium part of the increment, is inserted in the yield stress

$$\sigma_y = (1 - \omega_p^t)\hat{\sigma}_y(\varepsilon_p) \tag{5.16}$$

and the degraded elastic constants

$$\begin{aligned} \lambda &= (1 - \omega_p^t)\hat{\lambda} \\ \mu &= (1 - \omega_p^t)\hat{\mu} \, . \end{aligned} \tag{5.17}$$

On the basis of these degraded material properties, the solution of the global equilibrium problem BVP_1 and the local stress update is done via an Updated Lagrange approach and a conventional Newton-Raphson iterative scheme using the finite element code MSC.MARC. Linear quadrilateral elements are used, with the constant dilatation and assumed strain options switched on to prevent locking [87].

Reference is made to [23, 87] for details on the solution procedure used by MSC.-MARC. Here we limit ourselves to mentioning that the damage ω_p^t is introduced in the work hardening behaviour (5.16) via the subroutine "WKSLP", which is called at every integration point during every iteration. The damage effect in the elastic properties is modelled as a fictitious temperature effect, using the input option "TEMPERATURE EFFECTS".

Upon convergence, the solution yields the nodal displacements $\underset{\sim}{u}$, which are used to update the nodal positions $\underset{\sim}{x} = \underset{\sim}{x}^t + \underset{\sim}{u}$, and the state variables $\{\boldsymbol{\sigma}, \varepsilon_p\}$ needed for the nonlocal step.

5.3.2   Nonlocal averaging step at fixed configuration

BVP_2 is solved for the configuration $\vec{x}$ obtained through the solution of BVP_1 (Section 5.3.1). The local damage driving variable z is updated based on the stress and plastic strain field obtained in BVP_1 employing a backward Euler integration rule:

$$z = z_t + \left\langle 1 + A\,\frac{\tau_h}{\tau_{eq}} \right\rangle \varepsilon_p^B \Delta\varepsilon_p \,. \tag{5.18}$$

The nonlocal variable $\bar{z}$ is obtained by numerically solving the nonlocal averaging problem (BVP_2) at the fixed configuration $\vec{x}$. For this part of the algorithm, a special purpose code has been written which is called at the end of each MSC.MARC increment. The weak form of (5.10) reads, for the domain Ω furnished by the equilibrium problem

$$\int_\Omega \left(w_{\bar{z}}\,\bar{z} + \ell^2 \vec{\nabla} w_{\bar{z}} \cdot \vec{\nabla}\bar{z} \right) d\Omega \;=\; \int_\Omega w_{\bar{z}}\,z\,d\Omega \,, \tag{5.19}$$

where use has been made of the divergence theorem and Eq. (5.11). The local variable z is known from (5.18) and $w_{\bar{z}}$ is a scalar test function which must satisfy the usual conditions. Using a standard Galerkin finite element discretisation, Eq. (5.19) is rewritten as

$$\int_\Omega (\underline{N}_{\bar{z}}^T\underline{N}_{\bar{z}} \,+\, \ell^2 \underline{B}_{\bar{z}}^T\,\underline{B}_{\bar{z}})\bar{z}\,d\Omega \;=\; \int_\Omega \underline{N}_{\bar{z}}^T z\,d\Omega \,, \tag{5.20}$$

with $\underline{N}_{\bar{z}}^T$ containing the nodal interpolation functions and $\underline{B}_{\bar{z}}^T$ their derivatives referred to the configuration $\vec{x}$. Eq. (5.20) can be written in a more compact format as

$$\underline{K}_{\bar{z}\bar{z}}\tilde{\bar{z}} \;=\; \underset{\sim}{f}_{\bar{z},\mathrm{int}}\,, \tag{5.21}$$

where the column matrix $\tilde{\bar{z}}$ contains the nodal values of $\bar{z}$, and the matrix $\underline{K}_{\bar{z}\bar{z}}$ and the column matrix $\underset{\sim}{f}_{\bar{z},\mathrm{int}}$ are given by

$$\underline{K}_{\bar{z}\bar{z}} \;=\; \int_\Omega (\underline{N}_{\bar{z}}^T\underline{N}_{\bar{z}} \,+\, \ell^2 \underline{B}_{\bar{z}}^T\,\underline{B}_{\bar{z}})\,d\Omega$$
$$\underset{\sim}{f}_{\bar{z},\mathrm{int}} \;=\; \int_\Omega \underline{N}_{\bar{z}}^T z\,d\Omega \tag{5.22}$$

respectively. Solving the linear system (5.21) delivers the nodal values of $\bar{z}$ and, by interpolation, the Gauss point values of this field. The history variable κ is then updated in each Gauss point through

$$\kappa \;=\; \max(\kappa^t, \bar{z}) \tag{5.23}$$

and consequently the damage variable

$$\omega_p \;=\; \omega_p^t + h_\omega \Delta\kappa \tag{5.24}$$

with h_ω defined in (5.8).

5.4   Crack initiation-propagation and mesh adaptivity

After every loading step, which consists of an equilibrium step and a nonlocal step, it is checked whether crack initiation or propagation occurs based on the damage field ω_p. The geometry of a propagating crack is accommodated in the finite element by generating a complete new mesh, which conforms the updated problem geometry. Remeshing is followed by transfer of the state variables. To restore equilibrium, an equilibrium step with zero load increment and no damage growth is performed, followed by a nonlocal step at fixed configuration. To avoid large element distortions, especially near the tools, remeshing is done after a fixed number of time increments. Details of the remeshing and transfer algorithm can be found in Chapter 2 [82] and are omitted for brevity here. A new element in the algorithm compared to Chapter 2 is the criterion which is used to set the local element sizes in the remeshing operation. In Chapter 2, smaller elements were generated near the crack tip. This introduces a certain adaptivity, since the refined region will always follow the propagation of the crack tip. However, this ad-hoc adaptivity only becomes active once a crack has been initiated. In order to accurately describe the damage growth prior to crack initiation and the precise onset of crack initiation, a priori knowledge on the location of the crack was still necessary. To make the simulation tool more generally applicable without resorting to a fine mesh in the entire domain, an adaptive meshing criterion has been implemented based on the damage development. Since the crack growth is governed by the evolution of damage ahead of the crack, this criterion will still result in a refined mesh ahead of cracks. But before crack initiation it will also pick up the regions in which damage is developing, automatically inducing a refinement of the discretisation in these regions.

Different adaptive remeshing criteria have been proposed in the literature for localised responses [91, 112, 140]. In a local damage context, heuristic error estimators have been devised which reflect the nature of the localisation processes; for example the criterion proposed in [132] is based on the damage work. Other error estimators have been derived for nonlocal damage models of the integral type [36, 109] and gradient type [126].

In [94], where an integral-nonlocal brittle damage model is applied, a simple criterion was used, which consists in distributing the desired element size according to the damage field, hence having finer elements in the regions of higher damage. However, the application of this criterion to our crack propagation model would result in an excessively refined crack wake, since the damage is maximum there, which would not contribute to improve the accuracy of the solution and would only make the computations unnecessarily expensive. For this reason, we will use a *damage rate* based criterion, whereby the finest elements are used in the areas with the highest damage rate, which are generally found in the fracture process zone ahead of the crack. Before the nucleation of cracks, this damage-rate based mesh adaptivity criterion enables to have a fine mesh in those areas where crack initiation will ultimately occur.

When the average damage rate in an element, given by

$$\dot{\omega}_p^e \;=\; \frac{\int_{\Omega_e} \dot{\omega}_p \, d\Omega_e}{\int_{\Omega_e} d\Omega_e} \; , \tag{5.25}$$

exceeds a maximum value r_{max}, the new element length l_e is set equal to l_{min}, which is a fraction of the internal length ℓ (e.g. $\frac{\ell}{4}$). Note that elements should be smaller than ℓ in localisation bands in order to maintain the mesh objectivity. In regions where there is no damage growth or where $\dot{\omega}_p^e$ tends to be smaller than the threshold r_{min} (i.e. a fraction of r_{max}), the new element length is set to l_{max} (i.e. a multiple of ℓ). For intermediate values, $r_{min} < \dot{\omega}_p^e < r_{max}$, the new element length l_e is interpolated between l_{max} and l_{min}. The resulting values of l_e are used as target values for the mesher.

Numerically $\dot{\omega}_p^e$ is computed using a finite difference rule in time and the quadrature rule of the element:

$$\dot{\omega}_p^e \;\approx\; \frac{\Delta \omega_p^e}{\Delta t} \;=\; \frac{\sum_{k=1}^{n} \mathsf{w}_k \, \Delta \omega_p^k J_k}{\Delta t \, \sum_{k=1}^{n} \mathsf{w}_k J_k} \tag{5.26}$$

where w_k, J_k denote the weighting factor and Jacobian at the kth quadrature point, and n is the number of quadrature points per element.

The correlation between mesh density and damage rate is illustrated in Fig. 5.1, which shows different stages of a blanking simulation that will be discussed in detail in Section 5.5.1. During blanking, most of the plastic deformation and damage takes place in a shear band which is formed between the punch and the die, in which fracture will ultimately occur. Fig. 5.1 shows the mesh evolution in this shear band, for the proposed damage-rate remeshing criterion, along with the damage increment between successive time steps. As can be noticed, a higher mesh density indeed corresponds with regions of higher damage growth and a fine discretisation is thus obtained in a region which is currently governing the overall response. As the punch goes down, damage growth and hence the mesh become more localised. During crack propagation, all damage growth takes place between the crack tips and the mesh is concentrated in this ligament.

5.5 Applications

In order to illustrate the ability of the operator-split ductile damage implementation to model industrially relevant manufacturing processes, a few typical cases have been modelled and results are next compared with published experimental data where possible.

5.5.1 Blanking

Blanking is a metal forming process whereby a piece of material is cut from a sheet by extreme shearing (Fig. 5.2). A punch pushes the metal sheet downwards into a
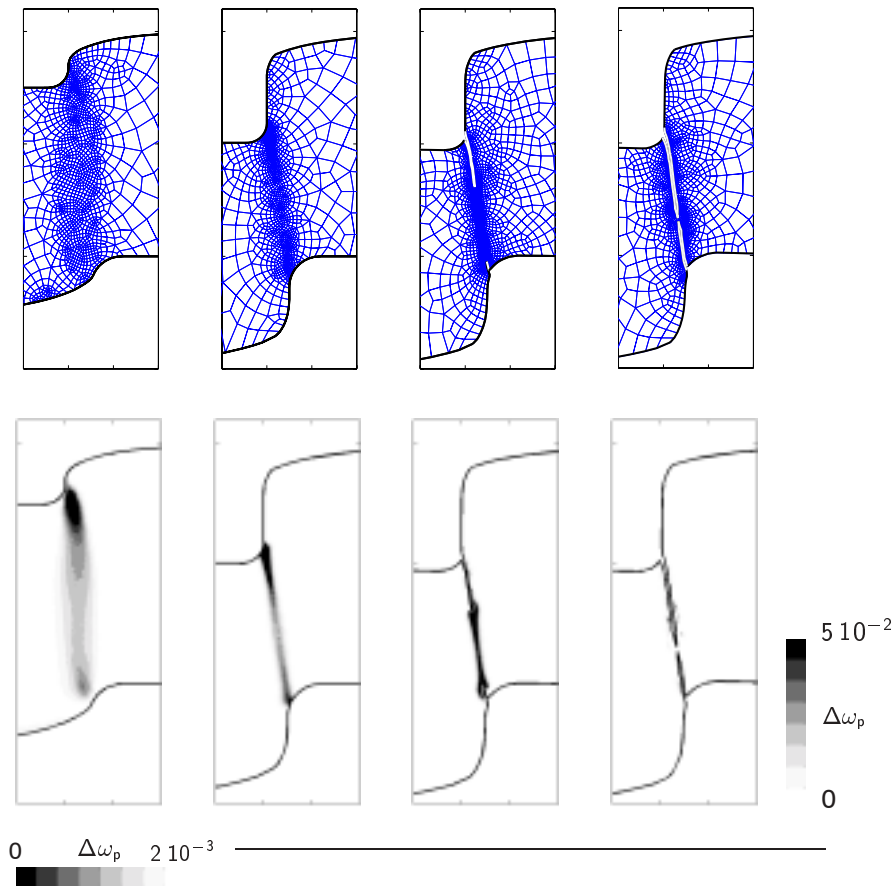
Figure 5.1 — *Adaptive remeshing in crack propagation. Mesh evolution (above), damage increment (below).*

die, while the sheet is simultaneously held in place by a blankholder, which may not be present in simpler setups. This causes the metal sheet to shear, and eventually the material fractures along a shear crack. Fig. 5.2 shows a schematic representation of the cut edge after complete separation. A number of zones can be distinguished on the edge, namely a rollover zone in which the material has been drawn into the clearance between punch and die, a sheared edge which has been in contact with the die and generally has a smooth appearance, and a much rougher fracture surface along which the material has finally failed. At the end of the fracture surface a burr is usually formed. This burr and the relatively rough fracture surface are usually undesired and must therefore be removed by subsequent operations (e.g. grinding).

Reducing or even eliminating them by optimising e.g. the tool design, is therefore of great interest, and the computational tool developed here may assist in this optimisation process by predicting the influence of design changes.
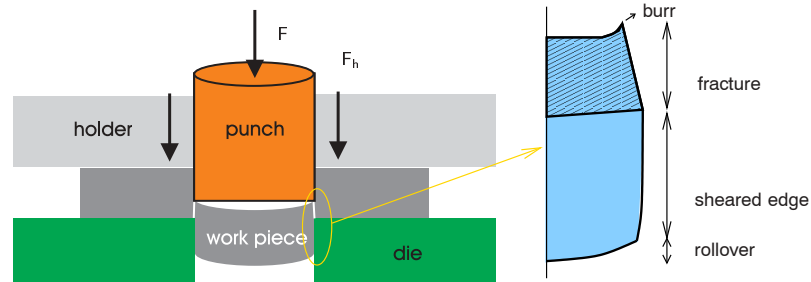

Figure 5.2 — *(left) Blanking setup. (right) Schematic representation of a typical product edge after blanking.*

Blanking has been object of much research, both experimental [60] and numerical. Numerical simulations of blanking often rely on an uncoupled damage variable to predict fracture [113], also known as the local approach. This type of approaches are straightforward to implement, but do not account properly for material failure. More advanced coupled models, which rely on continuum damage mechanics or softening plasticity, have been used to model material failure in blanking, e.g. Gurson models, [58, 105]. However, these coupled models were not regularised and were therefore prone to pathological localisation effects – although in [58] the damage law was adapted to obtain the proper fracture energy. Contrary to the uncoupled models, coupled models show a pronounced localisation of plastic strain as occurs in reality [104]. To predict the failure surface in blanking – and thus the product shape –, element erosion [128], nodal separation [67] and remeshing techniques [30] have been used. A shortcoming of the coupled continuous-discontinuous approaches towards blanking as reported in the literature is that they are based on local continuum descriptions and therefore suffer from pathological localisation. As previously mentioned and by now generally accepted, coupled models must be supplied with an internal length (regularisation) in order to obtain meaningful results. It is the purpose of this section to illustrate how the combined gradient continuum-discontinuum approach developed in the previous sections may be used to address this shortcoming of existing models.

In this section the results of blanking simulations are compared with experiments performed by Goijaerts et al. [55], who performed blanking tests on a variety of materials. We will consider, however, only the experiments on a X30Cr13 stainless steel sheet of $t = 1$ mm thickness. A cylindrical punch was used, with dimensions, indicated in Fig. 5.3, $l_d = 15$, $l_s = 5$, $r_d = 0.136$ (units in *mm*). Several values have been used for the clearance (s) and the punch radius (r_p); the combinations used are

given in Fig. 5.3.

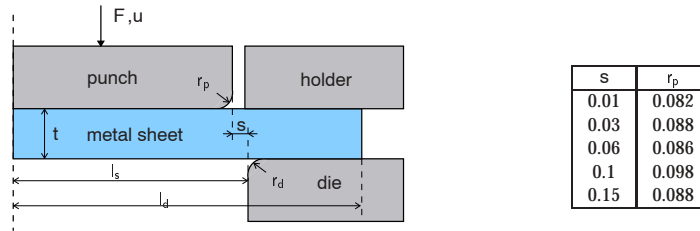| s	r_p
0.01	0.082
0.03	0.088
0.06	0.086
0.1	0.098
0.15	0.088

Figure 5.3 — *Geometry used in the blanking simulations; the table defines the different punch geometries used (units in mm).*

The material behaviour was modelled using the gradient enhanced elastoplastic damage model discussed in Section 5.2, with the material parameters summarised in Table 5.2 [55]. The hardening response of the undamaged (effective) material has been determined experimentally by Goijaerts in the form of a table; a graphical representation is given in Fig. 5.4.
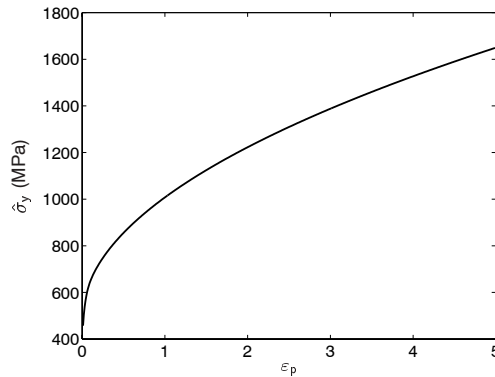

Figure 5.4 — *Strain hardening curve, from Goijaerts et al. [55].*

The parameter κ_c of the damage evolution has been determined so that the measured values of punch displacement at fracture could be reproduced, assuming $\kappa_i = 0$. The internal length has been set to $\ell = 10\mu$m, which seems to be a reasonable estimate for the scale at which void interaction takes place. Linear, quadrilateral axisymmetric elements were used in the computations, with constant dilatation and assumed strain. The punch, holder and die have been modelled as rigid tools. The simulations were displacement driven. Adaptive remeshing as described in Section 5.4 was used throughout the computations.

Table 5.2 — *Material properties of X30Cr13 stainless steel [55] used in the blanking simulations.*

Shear modulus G	70.3 GPa
Bulk modulus K	136.4 GPa
Initial flow stress σ_{y0}	0.443 GPa
Damage initiation threshold κ_i	0
Critical value of history parameter κ_c	7
Damage parameter A	3.9
Damage parameter B	0.63
Internal length ℓ	10 μm

Fig. 5.5 shows the evolution of the ductile damage, the triaxiality, as well as of the geometry during the punch penetration for a clearance of 0.03 mm. The lowering of the punch gives rise to an increase in plastic deformation in the clearance area, resulting in damage and localisation into a shear band. The damage is maximum at the rounded punch edge. A first crack therefore appears here, and propagates towards the die in a shear mode. From the figure, it is clear that the radius of the tool has an important impact on the burr height and should be small for smooth products. However, in practice r_p tends to increase due to wear. With increasing deformation, a second crack is initiated at the die. Both cracks meet somewhere along the thickness, provided the clearance is not too large.

The experiments showed that smaller clearances resulted in larger punch forces and a deeper penetration of the punch before fracture occurred. It was argued by Goijaerts et al. [55] that this increase in ductility with decreasing clearance must be due to the presence of a higher compressive (or lower tensile) stress state, which delays void growth. This effect is captured in the present simulations, as illustrated in Fig. 5.6, which shows the simulated force-displacement curves (Fig. 5.6 (a)) and a comparison of the maximum forces and displacements in these curves with the experimental data from [55] (Fig. 5.6 (b)). The presence of higher (tensile) hydrostatic stress for larger clearances is confirmed by Fig. 5.7, which shows that for the same punch stroke, triaxiality increases with clearance, thereby causing earlier failure. Note, however, that the pictures show that the 10 mm clearance is not the most damaged, because of its larger punch radius (Fig. 5.3 right).

The final product shapes obtained in the simulations for different clearances are shown in Fig. 5.8 (a) and Fig. 5.8 (b), where the latter shows a zoom of the cut surface. The smaller the clearance, the larger the shear zone and the smaller the fracture zone. This trend is in agreement with the observations made in the experiments [55]. It can also be observed that the burr height is relatively unaffected by the clearance.
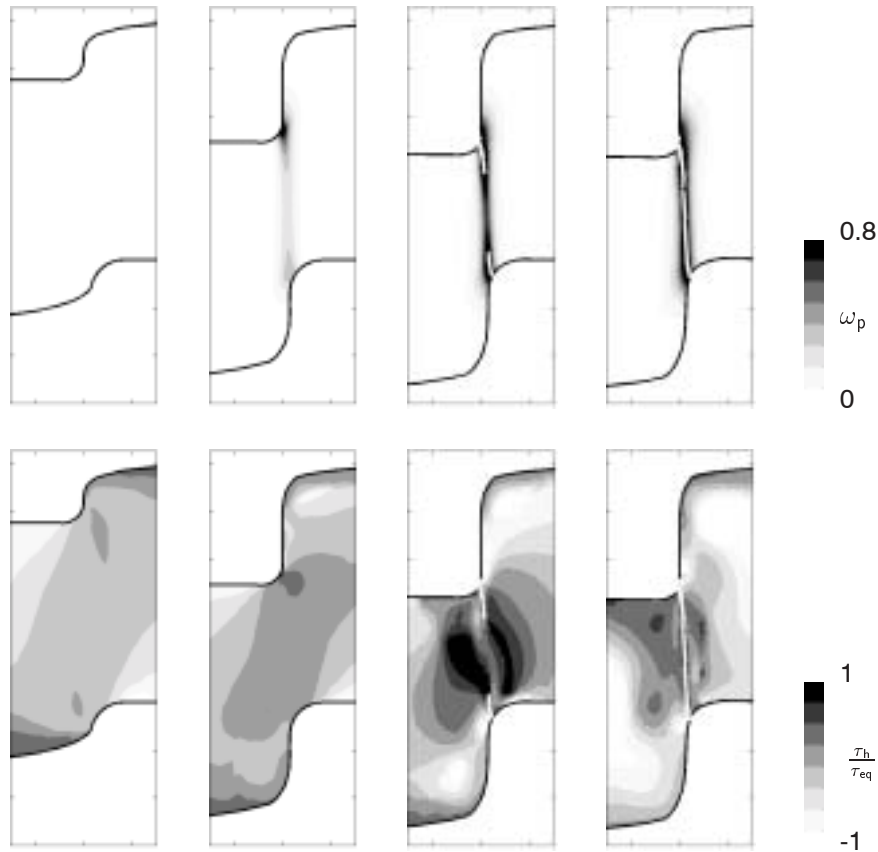
Figure 5.5 — *Blanking. Evolution of state variables in the shear zone (clearance 0.03 mm): Damage (ω_p) and triaxiality ($\frac{\tau_h}{\tau_{eq}}$).*

5.5.2   Fine blanking

The significant influence of hydrostatic stress on the ductile fracture process has sparked attempts to improve the quality of blanked edges by inducing compressive stresses during the blanking process. This is the basic concept upon which fine blanking was developed. It features the use of three independent presses, working in a 'triple action mode' (Fig. 5.9 (a)). The first action is the holder closure (F_h). This holder may have a v-ring, aimed at creating an additional compressive stress as well as at keeping the sheet in place. The second action is the downward motion of the blanking punch (F). The third action is applied by a counterpunch, working against the blanking punch (F_c). Fine blanking uses smaller clearances compared to conventional blanking. The result is a clean-cut surface and an improved flatness of the
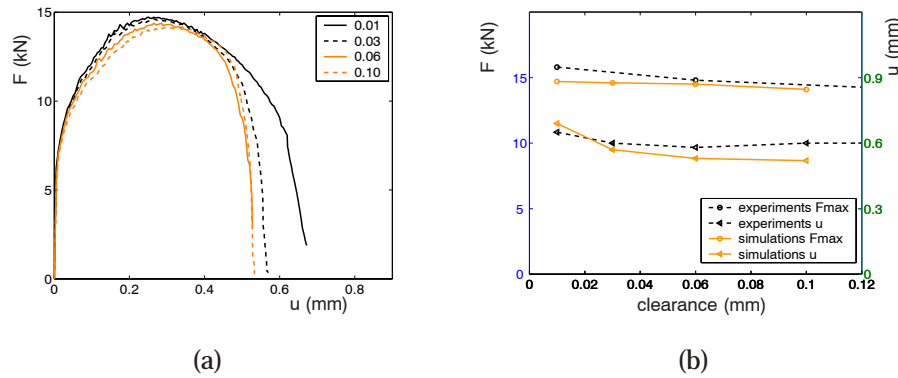
(a)   (b)

Figure 5.6 — *Blanking. (a) Simulated punch force-displacement curves for different clearances. (b) Experimental versus simulated maximum force and punch displacement at fracture for different clearances.*

resulting product.

Fine blanking has been investigated experimentally [34, 72] and numerically. Numerically, uncoupled [68] and coupled [59] damage models have been used in fine blanking. In Ref. [59] the same fracture-energy 'regularisation' technique was used as in [58] (see above, blanking Section 5.5.1). The crack geometry has been represented in [68] using an element-erosion technique, where also study of the effect of the v-ring indenter can be found. Here, the combined approach as discussed earlier has been applied to the fine blanking process.

The material properties used in our simulations are the same as in the blanking case discussed above. A clearance of 0.01 mm has been used. The radii of the tools are taken from Fig. 5.3. The dimensions of the v-ring are indicated in Fig. 5.9 (b), with $d_r = 0.3$ mm, $r_r = 0.05$ mm, $h_r = 0.2$ mm. A holder force (F_h) of 25 kN is applied, which ensures that the sheet material stays in contact with the die and which creates a high hydrostatic compressive stress state. Adaptive remeshing is used throughout the computations (Section 5.4).

By increasing the counterpunch force, a higher hydrostatic compressive stress is induced in the clearance zone, which delays the formation and growth of voids and thus increases the material ductility. As a result, the material deforms more extensively before a crack is initiated, resulting in a larger shear zone and thus in a smoother final surface. This is shown in Fig. 5.10 (a), where the profiles at the onset of fracture are shown for two different counterpunch forces, namely for 10 kN, 50 kN and for the case of 10 kN with a v-ring. The result obtained without counterpunch ('blanking') is also given as a reference. The 10 kN counterpunch is shown to slightly increase the ductility by increasing the compressive hydrostatic stress state. The v-ring gives a slight further improvement. But by far the best result is obtained with the (very high) counterpunch force of 50 kN. Of the four cases studied
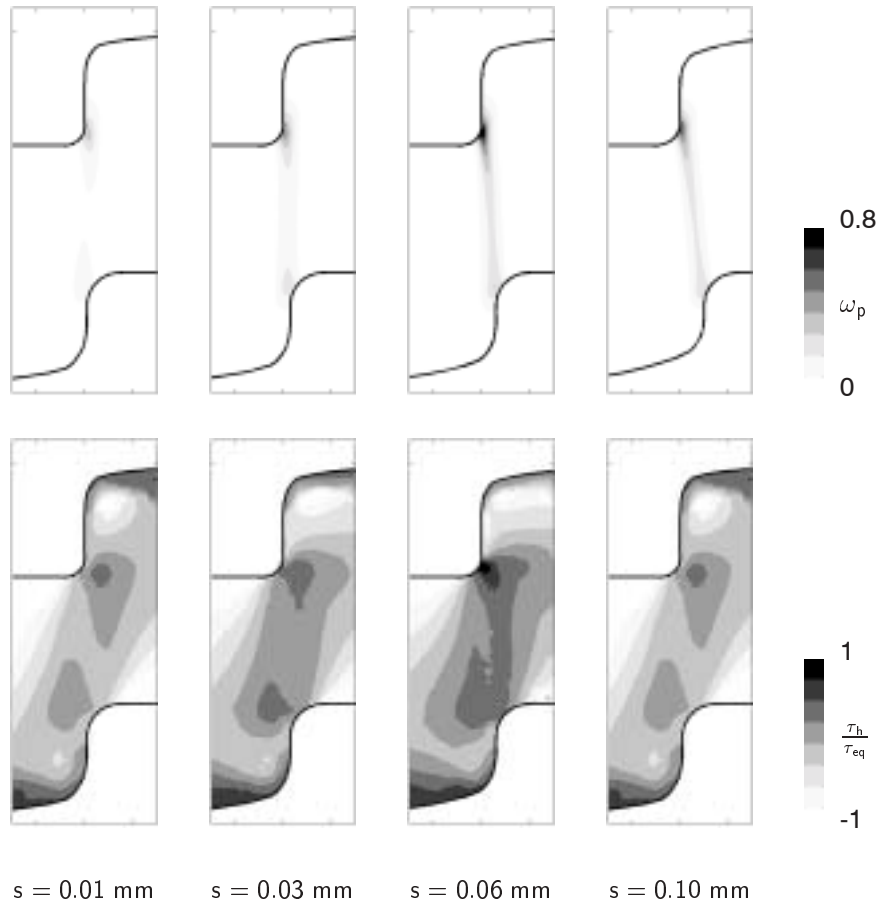
Figure 5.7 — *Blanking. Increase in triaxiality (higher hydrostatic tensile state) and damage with clearance. (above) damage ω_p, (below) triaxiality $\frac{\tau_h}{\tau_{eq}}$.*

the maximum force difference between punch and counterpunch, ΔF, is very similar, approximately 15 kN (Fig. 5.10 (b)). The beneficial effect of the superimposed compressive hydrostatic stress can be seen in Fig. 5.11, which shows the damage and triaxiality fields at the same punch depth for the three fine blanking cases and for regular blanking (0.01 mm clearance). A high external pressure reduces the local hydrostatic tension near the punch corner and thus delays the growth of damage. This is why the 50 kN counterforce fine-blanking case fails last (Fig. 5.11 (d)). The 10 kN counterforce has the same effect, but to a lesser extent. The highest triaxiality is found for conventional blanking which is therefore the first to fail (Fig. 5.11 (a)). Compared with the $F_c = 10$ kN case, the v-ring leads to only a slight improvement

(a)   (b)
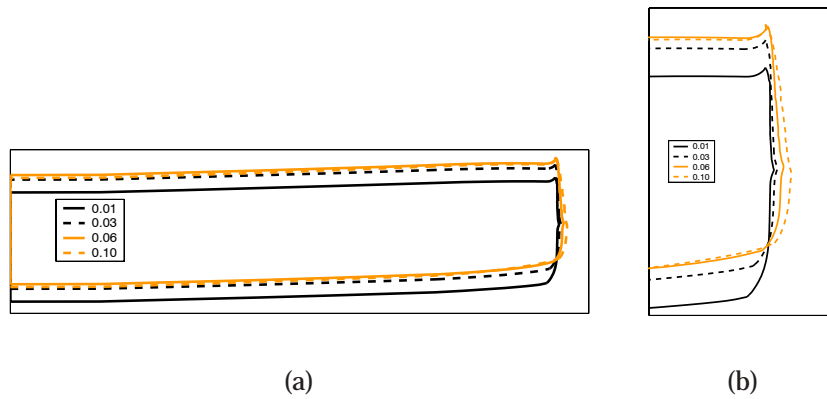
Figure 5.8 — *Blanking. (a) Final product shape for different clearances. (b) Zoom of cut edge.*
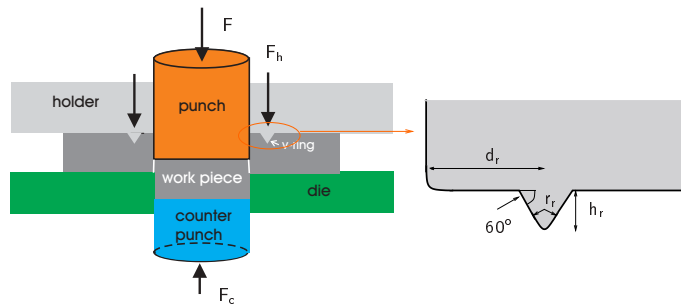
Figure 5.9 — *(left) Fine blanking setup. (right) v-ring dimensions.*

since its action is local, and quite far from the fracture process zone (Fig. 5.11 (c)).

As a result of the counterpunch force, fine blanking results in a much flatter product, as can be observed by comparing the final product shapes of Fig. 5.12 (a) with those of Fig. 5.8 (a). Furthermore, the delayed initiation of cracks results in a smaller fracture zone and thus in a smoother edge profile, as compared with blanking (Fig. 5.12 (b)). This beneficial influence increases for larger counterpunch forces.

(a)   (b)

Figure 5.10 — *Fine blanking. Effect of counterpunch and v-ring. (a) profiles at crack initiation; (b) nett force $\Delta F = F - F_c$ (punch force minus counterpunch force) vs displacement, u.*

5.5.3 Score forming

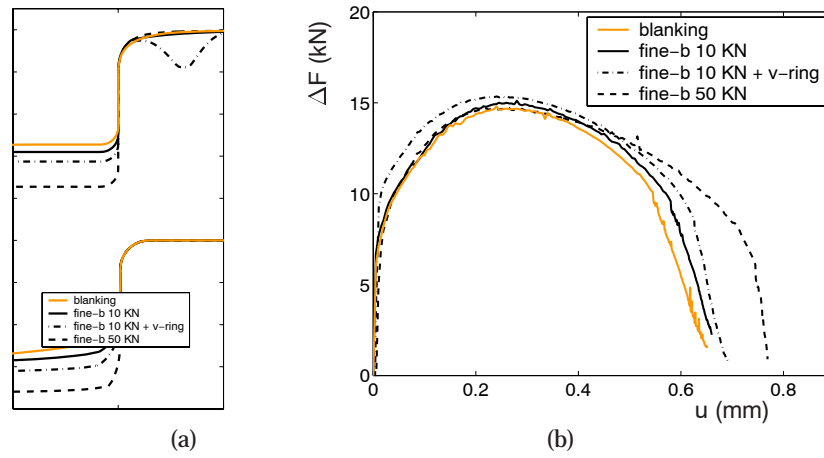The final application considered here is the score forming process. Score forming is an operation used in the can making industry to produce a groove along the perimeter of FAEOE (Full Aperture Easy Open End [138]) can lids. A detailed experimental and numerical study of the score forming process has been done by Boers et al. [23]. In the experiments, a groove was formed by indentation of metal strips, and the influence of the material type and indenter shape was studied. The simulations were done using a gradient damage-plasticity model with a shear-driven damage evolution law, in which the operator-split implementation of the gradient damage enhancement was introduced for the first time. Here we will use the full, triaxiality-dependent damage modelling as introduced in Section 5.2, as well as the adaptive remeshing and crack growth algorithms, enabling us to carry out the computations to final failure. This application is particularly interesting because it shows a strong, experimentally established, relationship between damage development and crack growth. Indeed, it turns out that the damage which is generated during the forming of the score has an important impact on the lid's opening behaviour.

The dimensions of the score forming setup are given in Fig. 5.13 [23]. The experiments showed that depending on the type of indenter and on the material, failure occurred at different indentation depths. The failure mechanisms consisted in the formation of localised shear bands under the indenter, with nucleation and growth of elongated voids, which evolved into macroscopic cracks (Fig 5.14 (a), (b)).

In the present simulations, a 210 μm thick T67CA steel strip was investigated. The deformation has been assumed to be symmetric and planar. The material prop-
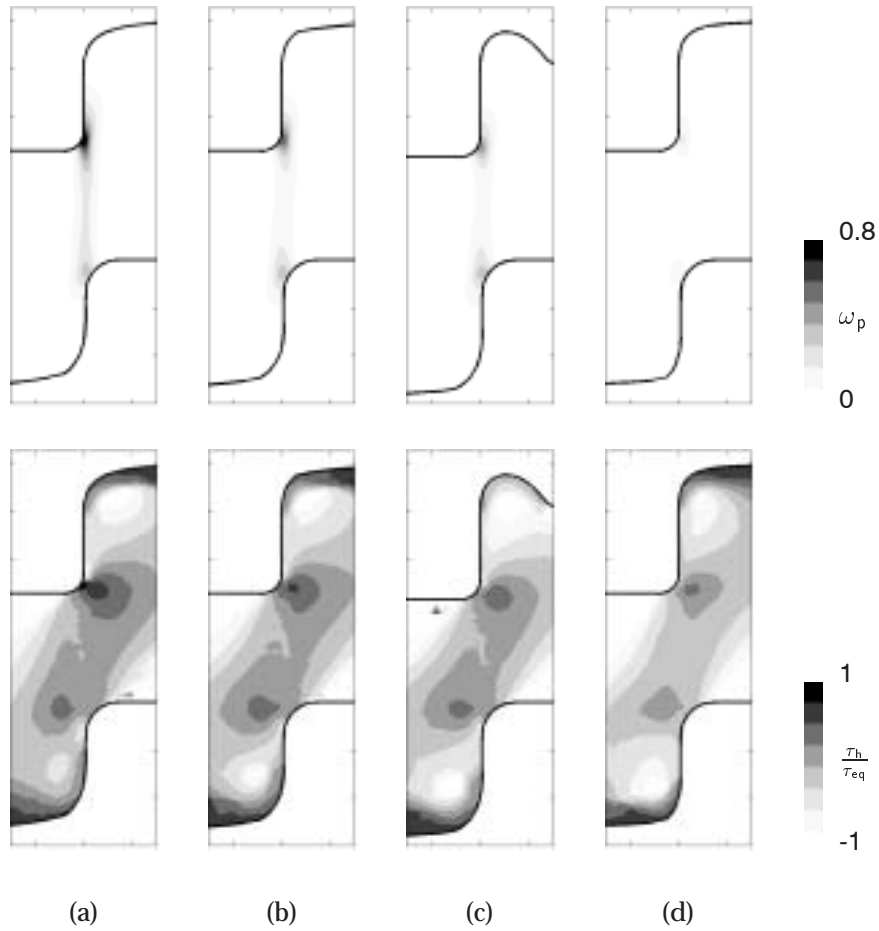
Figure 5.11 — *Influence of fine-blanking configuration on damage development and stress triaxiality (clearance 0.01 mm). (a) regular blanking; (b) fine-blanking, $F_c = 10$ kN; (c) fine-blanking, $F_c = 10$ kN with v-ring; (d) fine-blanking, $F_c = 50$ kN.*

erties are summarised in Table 5.3, obtained in [23]. The strain-hardening behaviour is described in Fig. 5.15. The damage parameters A and B correspond to the values reported in [55] for a steel. Assuming $\kappa_i = 0$, the parameter κ_c has been determined in order to be able to reproduce the experimentally measured force-indentation depth curves, as well as to capture the failure mode (see below in Fig. 5.17 and Fig. 5.18).

Fig. 5.16 shows the deformation of the sheet near the indenter and the corresponding damage field as predicted by the model of Section 5.2 and by the triaxiality-insensitive model ($z = \varepsilon_p$), which was used by Boers et al. [23]. In this model $\kappa_c = 5$,

(a)   (b)
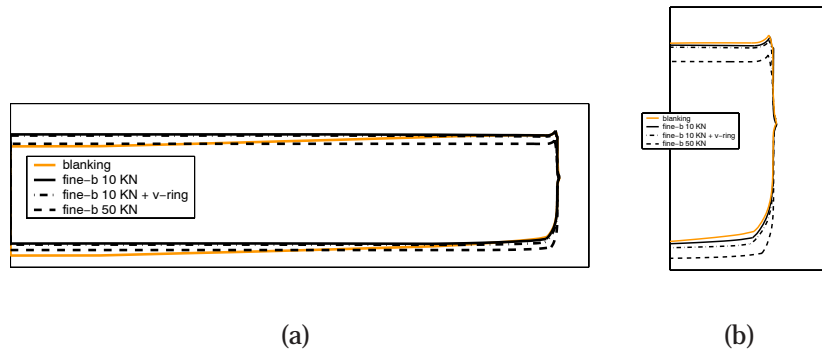
Figure 5.12 — *Fine blanking. (a) Final product shape for different counterpunch forces. (b) Zoom of cut edge.*
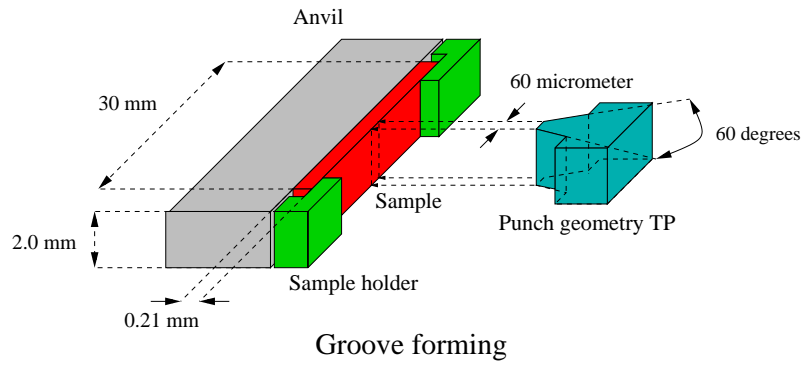
Figure 5.13 — *Groove forming setup and dimensions (courtesy of S.H.A. Boers).*

Table 5.3 — *Material properties of steel T67CA used in the score-forming simulations.*

Shear modulus G	80.77 GPa
Bulk modulus K	175 GPa
Initial flow stress σ_{y0}	0.506 GPa
Damage initiation threshold κ_i	0
Critical value of history parameter κ_c	15
Damage parameter A (Goijaerts)	3.9
Damage parameter B (Goijaerts)	0.63
Internal length ℓ	1 μm
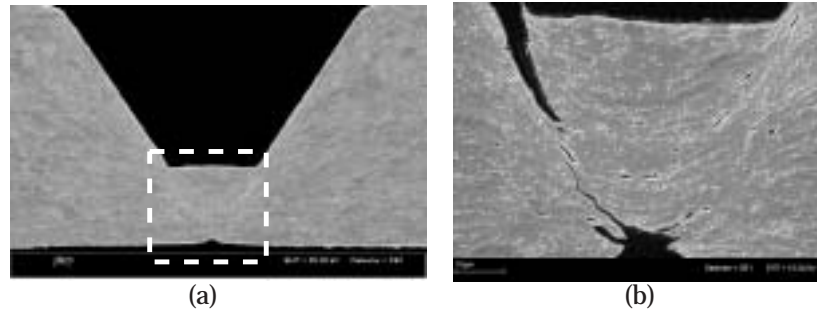
Figure 5.14 — *Scanning Electron Microscopy images of specimen after score-forming (courtesy of S.H.A. Boers).*
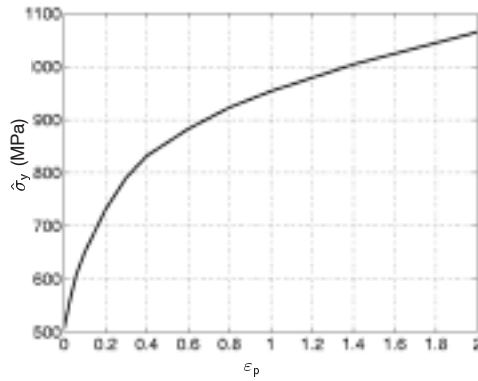
Figure 5.15 — *Strain hardening curve, from Boers et al. [23].*

so that failure would occur at approximately the same indenter depth as for the triaxiality-sensitive model. The triaxiality-insensitive model exhibits a high concentration of damage along the face of the indenter. In the experiments little damage was observed in this region, which can be explained by the fact that it experiences a compressive hydrostatic stress, as indicated by a '-' in Fig. 5.16, which prevents the formation and growth of voids. This is correctly picked up by the triaxiality-dependent model, which does not show any damage development in the compressive regions and a more localised damage band from the corner of the indenter to the bottom of the specimen. This is clearly more in agreement with the experiments (see Fig. 5.14).

Fig. 5.17 shows the finite element mesh and the distribution of damage and triaxiality at different stages of indentation. Initially, damage growth occurs at the bottom of the metal strip. As the indenter penetrates into the strip, a shear band is formed

Figure 5.16 — *Influence of triaxiality in the failure mechanism. (left) Goijaerts ($A = 3.9$), (right)* z $= \varepsilon_p$. *(+) compression, (-) tension.*

under the indenter, where most of the subsequent damage growth takes place and the triaxiality is positive. When the critical damage value is reached ($\omega_p = 1$), a first crack starts to grow from the indenter corner along the shear band, after which a second crack is initiated at the other end of the shear band, i.e. at the bottom of the specimen, near the symmetry axis. Wh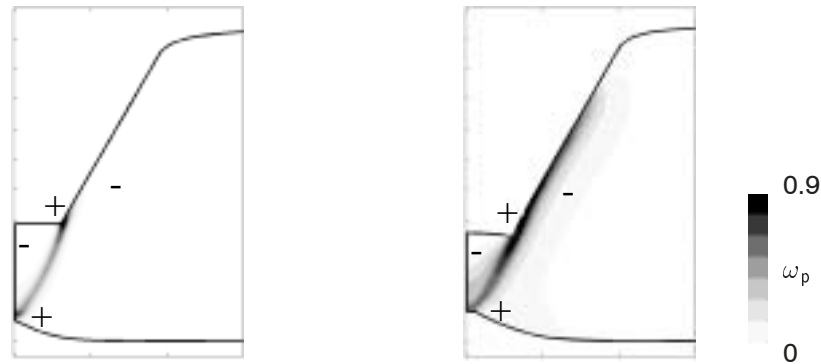en the two cracks meet, a wedge of material is separated from the surrounding material. The same failure pattern was observed for a number of materials. The agreement between simulations and experiments for one of this materials can be noticed in Fig. 5.18, which shows the experimentally observed and simulated geometries. Damage localisation, cracks and even the burr at the corner of the indenter are well predicted.

For the material parameters used in the simulations the agreement between the force-displacement response of the indenter is reasonable. The observed spikes in the hardening part of the simulated force-displacement curve may have two origins: transfer of state variables at each remeshing step and contact. These spikes disappear in the softening part, (i) because the stress changes are lower due to damage, and (ii) concentrate in a shear band, which is very finely meshed, and therefore the transfer errors are smaller. Due to this mesh adaptivity, the simulated force-displacement curve is much smoother than those given in [23].

5.6   Conclusions

This work aimed to develop a model for the simulation of ductile failure in metal forming process, including crack initiation and crack propagation. For this purpose a gradient enhanced elastoplastic damage model has been used in combination with a numerical framework for the modelling of discrete cracks.

We have shown that a combined approach, i.e. continuous damage plus discon-
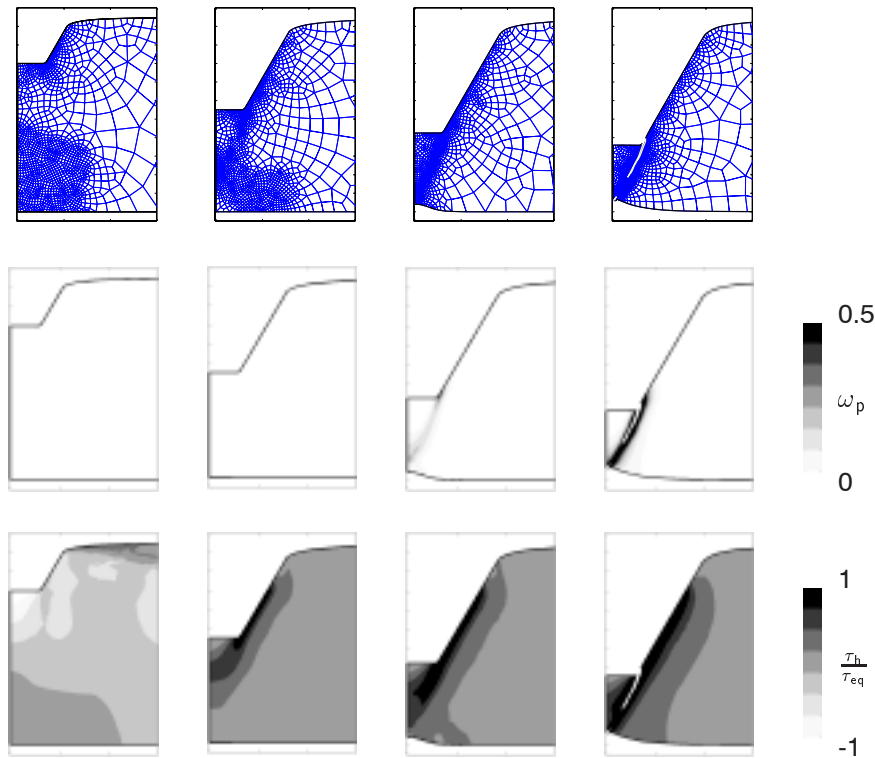
Figure 5.17 — *Evolution of mesh and state variables (damage ω_p, equivalent stress τ_{eq}, triaxiality $\frac{\tau_h}{\tau_{eq}}$) during the score forming process.*

tinuous cracks, is capable of describing the complete failure process. Crack initiation and propagation are based on a damage variable, which describes the microscopic degradation process in a phenomenological manner. Unlike uncoupled damage approaches, in a combined approach:

- Damage affects the mechanical material properties, which allows to describe better the transition from a continuous material to a discrete crack in a gradual manner.

- For the same reason, this combined model predicts vanishing stresses at the crack tip during crack propagation, which is more realistic than fracture mechanics or uncoupled damage approaches, since microscopic observations show that the material in this region is full of voids, and therefore the averaged mechanical properties are very low.

- The influence of pre-existing damage, e.g. resulting from previous forming
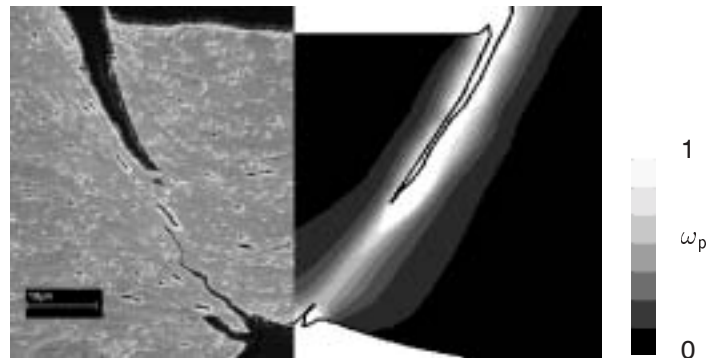
Figure 5.18 — *Ductile failure in score forming. Experiment versus simulation (damage field ω_p).*
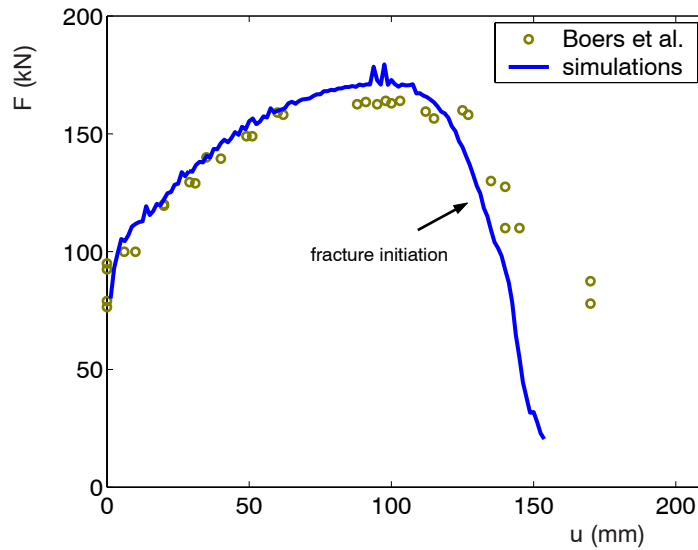
Figure 5.19 — *Score forming. Indenter force-displacement (clearance 3 mm): experiments versus simulation.*

steps, on the plastic deformation and the fracture behaviour can be taken into account in a natural fashion.

- Damage leads to softening and localisation (e.g. shear bands), which are also observed in experiments.

However, because of the softening, numerically a combined approach is more involved than an uncoupled one, since it requires special techniques to guarantee mesh

independent results. In the present work, a gradient enhancement has been used, which requires solving an additional partial differential equation, which together with equilibrium forms a coupled problem. Original aspects of this framework are:

- A realistic experimentally validated ductile damage evolution law has been used, which reflects the role of plastic strain and triaxiality in the microscopic degradation processes. The damaged response has been derived from the elastoplastic undamaged material using the notion of effective stress.

- The model has been implemented in an operator-split manner, which is easier to implement than the fully coupled problem and may therefore be more appealing for engineering purposes. For the solution of the equilibrium problem any commercial FE software can be used. We have opted for MSC.MARC, enabling to access various plasticity models and contact algorithms for the examples treated.

- A new mesh adaptivity criterion has been proposed, in combination with crack propagation. Simulations have shown that the proposed damage rate adaptivity criterion is capable of identifying critical areas in which a fine mesh is required. Mesh adaptivity hence extends the range of applicability of the modelling, by enabling to model large domains in spite of the small internal lengths necessary. Moreover, mesh adaptivity reduces the amount of diffusion associated with the transfer of state variables.

We have seen in the results of the simulations of blanking, fine-blanking and score forming processes (Sec 5.5), that the combined approach is indeed able to predict the relevant failure mechanisms, in agreement with experimental observations. So the developed simulation tool can indeed be used for damage engineering, i.e. the controlled application of damage and fracture.

In particular, the influence of stress triaxiality in the applications has been revealed. This influence in included in the constitutive modelling via the triaxiality-dependent damage growth according to Eq. (5.12). Although this evolution law improves the description of ductile failure with respect to standard J_2 plasticity and the pressure-insensitive plasticity-damage modelling used before to model e.g. score forming, the assumption that plastic flow is isochoric may still be too restrictive for applications in which a high hydrostatic tension exists. An extension of the continuum modelling which allows to capture plastic dilatation due to void growth is the subject of current research.

Chapter 6

Conclusions

The correct description of material failure has many useful applications, not only in the prevention of structural failure or structural life time assessments, but also in the design of manufacturing processes for new products. The latter application mainly motivated this research. At present, many different models are available to describe ductile failure, which can be categorised as either continuous (damage and softening plasticity) or discontinuous (e.g. cohesive zones). These models intend to provide useful results for specific problems, yet it is in general the combination of both, continuous and discontinuous, that gives the most accurate representation of ductile failure. A continuum model provides a better description of the underlying microscopic mechanisms that trigger failure, through a properly defined and regularised constitutive relation, which constitutes the precursor to the formation of cracks. Cracks, however, are better described with a discontinuous model. The main goal of this work was the development of a continuum-discontinuous model for the representation of failure, and of ductile failure in particular.

Cracks, from a computational perspective, are modelled here using a remeshing strategy. The main advantages of this approach are: (i) it allows to model arbitrary crack paths (unlike interface elements); (ii) it is compatible with any finite element code (no additional degrees of freedom need to be added as in partitions of unity methods); (iii) it prevents excessive element distortions in a large strain framework, (iv) it can be used in an adaptive manner to optimise the element distribution in the mesh. In most cases remeshing has a number of drawbacks: (i) the implementation is already quite cumbersome in two dimensions and even more elaborate in three dimensions, (ii) it may lead to lack of robustness in the computations, due to errors in the transfer of state variables, (iii) it can not handle many cracks propagating simultaneously. Nevertheless, remeshing has been applied here, where considerable attention has been given to dedicated techniques which address theses difficulties. The precise coupling of continuum and discontinuum models in this sense constitutes the main challenge of this work.

The main conclusions of the study reported in this thesis are:

- Crack propagation strategies based on uncoupled damage models (Chapter 2) tend to be practically appealing, because they are easy to implement and do not suffer from the difficulties associated with softening materials. Yet, uncoupled models cannot predict the localisation of damage and plastic strain due to damage, and do not capture the effect of (pre-existing) damage on the plastic response.

- Truly combined models (Chapters 3, 5), in which damage affects the constitutive material behaviour, are more accurate than their uncoupled counterparts. In a combined model, the transition from a continuous material to a discrete crack occurs in a more realistic, gradual, manner. Yet, their implementation is more elaborate, because the continuum softening model has to be regularised. In this study, the regularisation is done by means of a gradient enhancement, which has the advantage of being less involved numerically than other regularisation techniques, while providing the strong nonlocality needed in crack growth analysis.

- In reality, cracks are preceded by strain localisation, and this determines the direction of crack propagation. These phenomena are well captured in a combined approach. The direction of crack propagation in a combined approach depends on the damage evolution. One way to validate the damage evolution, is whether or not the resulting localisation pattern agrees with experimentally observed crack paths.

- The approach followed here, which combines a regularised softening material with discontinuities, is more realistic than so-called strong discontinuity approaches or approaches which combine discontinuities with non-regularised softening materials. Here traction-free discontinuities appear as a result of failure; whereas in strong discontinuity approaches the continuum material is replaced by a cohesive discontinuity upon bifurcation, which governs the material response until failure.

- In ductile failure, the damage evolution must include two influences, in order to reflect the underlying microscopic processes (Chapter 4): plastic deformation (deviatoric in nature) and hydrostatic stress or stress triaxiality. The effect of the triaxiality is that it decreases the material ductility in hydrostatic tension.

- Results based on continuum damage mechanics show that the effect of ductile damage on the yield stress is much more important than on the elastic stiffness.

- Remeshing is a useful tool to model crack propagation, and in combination with large strain localising materials it is a necessity. These three issues (crack propagation, large strains and localisation) can be tackled simultaneously with a single remeshing strategy (Chapter 5). The proposed mesh adaptivity strategy reflects the underlying physical processes, i.e. localisation pattern. In a gradient model, the localisation width depends on the internal length, which

imposes conditions on the element size. The use of adaptive remeshing allows to model larger domains with smaller, more realistic, internal lengths.

- The combined approach to ductile fracture requires a numerical strategy, which ensures the robustness of the computations, since this may be hampered by various factors. Among others: transfer errors during remeshing, abrupt changes in geometry during crack propagation, large element distortions, extensive damage development, sudden contact changes, etc. In this work, numerical strategies have been developed which successfully counter the negative effect of some of these factors, leading to a considerable improvement of the robustness of the computations (Chapter 2).

- The application of combined failure approaches to metal forming process which involve material separation (Chapter 5) is quite promising, and can give better results compared to previously applied uncoupled models. A gradient regularisation can be implemented readily in combination with commercial codes by making use of an operator-split algorithm for the coupled problem. Results of blanking and fine blanking have shown that the quality of the product depends on the stress triaxiality, since this determines the onset of fracture and thus the length of the fracture zone. In blanking, the fracture zone can be reduced by decreasing the clearance, since this decreases the triaxiality, whereas in fine blanking, the fracture zone can be further reduced by increasing the counterpunch force. In score forming, the presented combined model can capture the experimentally failure mode more realistically than the previously used pressure-insensitive modelling.

The following aspects still need further investigation:

- Determination of the length scale and other parameters for the gradient model, which can be obtained from indirect parameter identification based on measurements of the strain field [51], or micromechanical considerations (nonlocal void interactions).

- The damage evolution laws that have been used throughout this work are phenomenological, and are therefore only valid for a limited number of materials and under specific loading conditions. In a more general context, the damage evolution must rely on the material microstructure, for which unit-cell computations or more advanced multiscale models could be used.

- Viscous and thermal effects, since they may play an important role in metal forming processes at high strain rates. Thermal effects may cause softening and the formation of adiabatic shear bands, for which a regularisation scheme is needed as well.

- Damage anisotropy. Some loading conditions result in strongly anisotropic damage, which increases until failure occurs [75, 127].

Appendix A

Comparison between elastoplastic damage and plastic damage models-Numerical aspects

The elastoplastic damage model presented in Chapter 4 differs from the plastic damage model upon which it was based [50], in that damage not only affects the yield behaviour, but also the elastic response. The elastoplastic damage model is more realistic since it accounts for the physical fact that the elastic stiffness decreases with the increase in damage. Nevertheless, in Chapter 4 it was shown that the responses of both models were very similar. The numerical implementation of the elastoplastic damage model is slightly more straightforward, since the return mapping can be done in the effective stress space and then reduces to the return mapping of the underlying elastoplasticity model. Here, the computational differences between the two models are highlighted.

Continuum governing model

The governing equations of the elastoplastic and plastic damage models are listed in Table A-1. In the damage plastic model the distinction between effective and homogenised behaviour exists only in the yield stress, whereas a rigorous distinction between the two stress measures is made in the elastoplastic damage model. Nevertheless, the results shown in Chapter 4 were quite similar for realistic parameter values.

Table A-1 — *Continuum models: Elastoplastic damage versus plastic damage.*

Elastoplastic damage	Plastic damage	
$$\begin{aligned} \hat{\boldsymbol{\tau}} &= \tfrac{1}{2}\,{}^{4}\boldsymbol{H} : \ln \boldsymbol{b}_e \\ \hat{\tau}_y &= \hat{\tau}_y(\varepsilon_p) \\ \tau_y &= (1-\omega_p)\tau_y(\varepsilon_p) \end{aligned}$$		▶ effective elastic response ▶ effective hardening law ▶ homogenised softening-hardening yield stress
$\boldsymbol{\tau} = (1-\omega_p)\,\hat{\boldsymbol{\tau}}$ $\overset{\nabla}{\boldsymbol{b}}_e = -3\dot{\gamma}\,\frac{\hat{\boldsymbol{\tau}}^d}{\hat{\tau}_{eq}}\cdot\boldsymbol{b}_e$ $\dot{\gamma} \geq 0 \qquad \hat{\phi} \leq 0 \qquad \dot{\gamma}\hat{\phi}=0$ $\hat{\phi} \equiv \hat{\tau}_{eq} - \hat{\tau}_y$	$\boldsymbol{\tau} = \hat{\boldsymbol{\tau}}$ $\overset{\nabla}{\boldsymbol{b}}_e = -3\dot{\gamma}\,\frac{\boldsymbol{\tau}^d}{\tau_{eq}}\cdot\boldsymbol{b}_e$ $\dot{\gamma} \geq 0 \qquad \phi \leq 0 \qquad \dot{\gamma}\phi=0$ $\phi \equiv \tau_{eq} - \tau_y$	▶ homogenised stress ▶ flow rule ▶ loading-unloading conditions ▶ yield function
$$\dot{z} = \left\langle 1 + A\,\frac{\tau_h}{\tau_{eq}} \right\rangle \varepsilon_p^B\,\dot{\varepsilon}_p$$		▶ evolution of local variable z

Time discretisation

Stresses are integrated in time using an elastic predictor and a return mapping algorithm. As was already mentioned, in the elastoplastic damage model the return-mapping is done in the effective stress space and damage is only used to map effective stresses to homogenised stresses, which are then used to solve the equilibrium equation. The time integration of the rate evolution equation of the local variable is done by means of a Backward Euler rule. The discretised equations of the two models have been summarised in Table A-2.

Algorithmic tangent

The material part of the algorithmic tangents is obtained by linearisation of the Kirchhoff stress tensor τ and the increment of the local variable Δz (Table A-2). The results are presented in compact form in Table A-3 for the linearised stress $\delta\tau$ and the linearised local variable δz. Note that the structure of the tangents in the elastoplastic damage model is more clear. In the plastic damage model a nonlocal term appears due to the dependence of the local variable z on the damage ω_p. This dependence does not exist in the elastoplastic damage model and therefore the nonlocal term vanishes. The coefficients f_1 and f_2 are given in Chapter 4 and differ between the two models. In the elastoplastic damage model, f_1 and f_2 are expressed in terms of the effective stress, while in the plastic damage model they are expressed in terms of the homogenised stress.

Table A-2 — *Elastoplastic damage versus plastic damage.*

Elastoplastic damage	Plastic damage	
$\hat{\boldsymbol{\tau}} = {}^{\star}\hat{\boldsymbol{\tau}} - 3G\Delta\gamma\dfrac{{}^{\star}\hat{\boldsymbol{\tau}}^{d}}{{}^{\star}\hat{\tau}_{eq}}$ $\Delta\gamma = \dfrac{{}^{\star}\hat{\phi}}{H+3\,G}$ ${}^{\star}\hat{\phi} = {}^{\star}\hat{\tau}_{eq} - \hat{\tau}_{y}^{t}$ $\boldsymbol{\tau} = (1-\omega_p)\,\hat{\boldsymbol{\tau}}$	$\boldsymbol{\tau} = {}^{\star}\boldsymbol{\tau} - 3G\Delta\gamma\dfrac{{}^{\star}\boldsymbol{\tau}^{d}}{{}^{\star}\tau_{eq}}$ $\Delta\gamma = \dfrac{{}^{\star}\phi}{H\,(1-\omega_p)+3\,G}$ ${}^{\star}\phi = {}^{\star}\tau_{eq} - (1-\omega_p)\,\tau_{y}^{t}$ ${}^{\star}\boldsymbol{\tau} = {}^{\star}\hat{\boldsymbol{\tau}}$	▸ return mapping ▸ strain equivalence
$\Delta\mathsf{z} = \left\langle 1 + A\,\dfrac{\tau_h}{\tau_{eq}} \right\rangle \varepsilon_p^{B}\,\Delta\varepsilon_p$		▸ increment of local variable

Table A-3 — *Tangent operators for the elastoplastic damage and plastic damage models.*

$$\delta\boldsymbol{\tau} \;=\; d_1\,{}^4\boldsymbol{C}_{ep} : \frac{\partial \ln {}^\star\boldsymbol{b}_e}{\partial {}^\star\boldsymbol{b}_e} : \frac{\partial {}^\star\boldsymbol{b}_e}{\partial \boldsymbol{L}_\delta^T} : \boldsymbol{L}_\delta^T \;+\; \boldsymbol{C}_d\,\delta\bar{\mathbf{z}}$$

$${}^4\boldsymbol{C}_{ep} \;=\; \left[\, b_0\,\boldsymbol{I}\otimes\boldsymbol{I} + (1-3b_0)\,{}^4\boldsymbol{I}^{s} + 2(b_0-b_1)\,{}^\star\boldsymbol{N}\otimes{}^\star\boldsymbol{N} \,\right] : \tfrac{1}{2}{}^4\boldsymbol{H}$$

▶ linearised stress

Elastoplastic damage	Plastic damage	
$d_1 \;=\; 1-\omega_p$ $b_1 \;=\; \dfrac{Gc_1}{c_1^2 + \frac{\partial h_\varepsilon}{\partial \varepsilon_p}}$ with $c_1 \;=\; 3G + h_\varepsilon$ $\boldsymbol{C}_d \;=\; -\dfrac{\partial \omega_p}{\partial \kappa}\dfrac{\partial \kappa}{\partial \bar{\mathbf{z}}}\hat{\boldsymbol{\tau}}$	$d_1 \;=\; 1$ $b_1 \;=\; \dfrac{Gc_1}{c_1^2 + {}^\star\phi\,\frac{\partial h_\varepsilon}{\partial \varepsilon_p}(1-\omega_p)}$ with $c_1 \;=\; 3G + h_\varepsilon(1-\omega_p)$ $\boldsymbol{C}_d \;=\; -2\,b_2\,G\,{}^\star\boldsymbol{N}$ with $b_2 \;=\; \dfrac{c_1\tau_y^t + {}^\star\phi\,h_\varepsilon\,\frac{\partial \omega_p}{\partial \kappa}\frac{\partial \kappa}{\partial \bar{\mathbf{z}}}}{c_1^2 + {}^\star\phi\,\frac{\partial h_\varepsilon}{\partial \varepsilon_p}(1-\omega_p)},$ $\qquad {}^\star\boldsymbol{N} \;\equiv\; \tfrac{3}{2}\dfrac{{}^\star\boldsymbol{\tau}^{d}}{{}^\star\tau_{eq}}$ and ${}^\star\phi \;=\; {}^\star\tau_{eq} - \tau_y^t$	

$$\delta\mathbf{z} \;=\; \delta(h_{\mathbf{z}}\Delta\varepsilon_p) \;=\; \boldsymbol{M}_{ep} : \frac{\partial \ln {}^\star\boldsymbol{b}_e}{\partial {}^\star\boldsymbol{b}_e} : \frac{\partial {}^\star\boldsymbol{b}_e}{\partial \boldsymbol{L}_\delta^T} : \boldsymbol{L}_\delta^T \;+\; M_d\,\delta\bar{\mathbf{z}}$$

$$\boldsymbol{M}_{ep} \;=\; f_1\,b_1\,{}^\star\boldsymbol{N} + f_2\,\boldsymbol{I}$$

▶ linearised local variable

Elastoplastic damage	Plastic damage	
$M_d \;=\; 0$	$M_d \;=\; f_1 b_2$	

Appendix B

On the effect of an external pressure in the damage evolution

The effect of an external pressure on the material ductility was studied in Chapter 4. In a tensile test performed under different the external pressures (Fig. B-1), damage growth was accelerated or decelerated depending on whether the external pressure was negative (tension) or positive (compression).
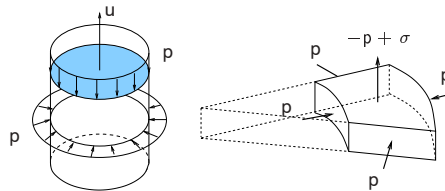

Figure B-1 — *(left) Tensile test on a cylindrical bar under a superimposed external pressure. (right) Stress state.*

If the external pressure is applied as an external fluid pressure as in [55], two situations may arise, depending on whether the voids are isolated from the fluid or not (see Fig. B-2). In the first case, with closed voids, the external pressure is solely supported by the matrix material. In the second, with open voids, the external pressure is balanced by the internal pressure acting in the voids together with the matrix material. Clearly the latter case, i.e. with open voids, is more favourable (under a compressive external pressure) since the matrix material has to support less load, resulting in less damage growth (see below). Note that similar situations arise in soil mechanics in consolidation problems. Yet, the effect of the external pressure is less accused here, since the porous material is limited to the fracture process zone.

In the case of closed voids, the volumetric effective Kirchoff stress acting on the
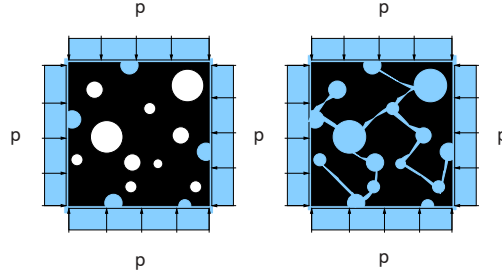
Figure B-2 — *External pressure applied to the voided material by a surrounding fluid. (left) Closed voids; the voids are isolated from the boundary and the pressure is resisted by the material matrix. (right) Open voids; the voids are connected with the boundary. The fluid penetrates and the external pressure is resisted by the internal pressure in the voids and the matrix.*

matrix material is given by

$$\hat{\tau}_{h-p} = \hat{\tau}_h - \frac{pJ}{1 - \omega_p}, \tag{B-1}$$

where $\hat{\tau}_h$ is the effective volumetric stress caused by the tensile loading, p is the external pressure and J is the volume ratio. When the voids are open, $\hat{\tau}_{h-p}$ is

$$\hat{\tau}_{h-p} = \hat{\tau}_h - pJ. \tag{B-2}$$

Eqs. (B-1) and (B-2) show that the open voids situation is less sensitive to the external pressure than the closed voids situation, i.e. the same pressure p will have a larger effect on the matrix material of the closed void case, hence causing less damage for the same compressive pressure p (positive). On the contrary, for negative (tensile) pressures, a faster damage growth is obtained in the closed voids case.

Numerical treatment of the uniform tension case

A difficulty in modelling this uniform tension problem (Fig. B-1) using finite elements, is that the tensile loading is displacement driven (it can not be force driven because of the softening behaviour), and therefore can not be superposed to the external pressure acting on the same boundary. To overcome this, the external pressure is not considered directly in the equilibrium problem, and only its effect on the damage evolution is accounted for. Note that damage influences the equilibrium state indirectly since it is linked to the stress state. Since we are only interested in the deformation caused by the tensile force, the volumetric elastic deformation caused by the external pressure can be neglected.

To maintain the quadratic convergence of the computations, the local variable z corresponding to the new hydrostatic stress, Eq. B-1 (or B-2), must be linearised.

The final expression of δz differs from that in (4.41), since this was derived for a zero external pressure.

In the closed void situation, the linearised local variable δz is given by

$$\delta z \ = \ \delta(h_z \Delta \varepsilon_p) \ = \ \boldsymbol{M}_{ep} : \frac{\partial \ln{}^{\star}\boldsymbol{b}_e}{\partial {}^{\star}\boldsymbol{b}_e} : \frac{\partial {}^{\star}\boldsymbol{b}_e}{\partial \boldsymbol{L}_{\delta}^{T}} : \boldsymbol{L}_{\delta}^{T} + 3f_2 \frac{p}{1 - \omega_p} \boldsymbol{I} : \boldsymbol{L}_{\delta}^{T} + M_d \delta \bar{z} . \quad \text{(B-3)}$$

with

$$M_d \ = \ \frac{3f_2 pJ}{(1 - \omega_p)^2} \frac{\partial \omega_p}{\partial \kappa} \frac{\partial \kappa}{\partial \bar{z}} . \quad \text{(B-4)}$$

and $\boldsymbol{M}_{ep}$ and the coefficients f_1 and f_2 defined in (4.42) and (4.43), where $\hat{\tau}_h$ has been replaced by $\hat{\tau}_{h-p}$, according to (B-2). The most striking difference with (4.41) is the nonlocal term $M_d \delta \bar{z}$ which is as a consequence of the linearisation of the damage variable ω_p in (B-2).

In the open void situation, the linearised local variable z is expressed as

$$\delta z \ = \ \delta(h_z \Delta \varepsilon_p) \ = \ \boldsymbol{M}_{ep} : \frac{\partial \ln{}^{\star}\boldsymbol{b}_e}{\partial {}^{\star}\boldsymbol{b}_e} : \frac{\partial {}^{\star}\boldsymbol{b}_e}{\partial \boldsymbol{L}_{\delta}^{T}} : \boldsymbol{L}_{\delta}^{T} + 3f_2 p \boldsymbol{I} : \boldsymbol{L}_{\delta}^{T} , \quad \text{(B-5)}$$

where the nonlocal term $\bar{z}$ has vanished.

Comparison: open versus closed voids

The results in the form of stress-strain curves for different pressures, negative and positive, are shown in Fig. B-3(a) and Fig. B-3(b), for the closed-voids and open-voids situations respectively. In either case, a positive (compressive) pressure reduces the amount of softening (damage) as compared with the zero-pressure case, whereas a negative external pressure accelerates failure (more softening). The difference between the closed-voids and open voids situations is as explained above. Under an external compressive pressure, the damaged growth of the closed voids material slows down faster, i.e. less softening, while under tension, the opposite effect occurs.
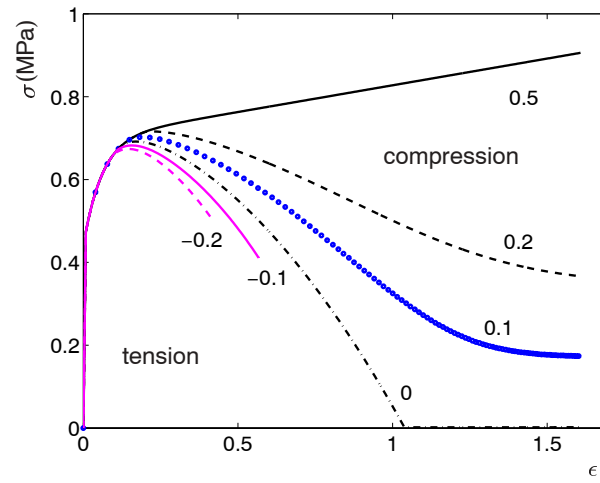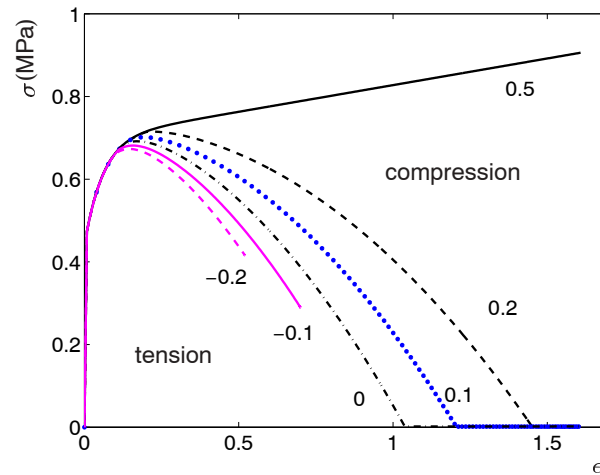
Figure B-3 — *Influence of an external pressure on the ductility. True stress (σ) - logarithmic strain (ϵ) in a tensile test. (a) closed voids, (b) open voids.*

Bibliography

[1] Aliabadi, M.H., 1997. A new generation of boundary element methods in fracture mechanics. *Engineering Fracture Mechanics*, **86**, 91–125.

[2] Alves, M. and Jones, N., 1999. Influence of hydrostatic stress on failure of axisymmetric notched specimens. *Journal of the Mechanics and Physics of Solids*, **47**, 643–667.

[3] Amstutz, B.E., Sutton, M.A., Dawicke, D.S. and Newman, J.C., 1996. An experimental study of CTOD for mode I/mode II stable crack growth in thin 2024-T3 aluminium specimens. *Fracture Mechanics*, vol. 26, ASTM, 256–271.

[4] Amstutz, B.E., Sutton, M.A., Dawicke, D.S. and Boone, M.L., 1997. Effects of mixed mode I/II loading and grain orientation on crack initiation and stable tearing in 2024-T3 aluminum. *Fatigue and Fracture*, **27**, 217–224.

[5] Anderson, T.L. (ed.), 1995. *Fracture mechanics: fundamentals and applications*. Boca Raton:CRC Press.

[6] Andersson, H., 1973. Finite element representation of stable crack growth. *Journal of the Mechanics and Physics of Solids*, **21**, 337–356.

[7] Arcan, M., Hashin, Z. and Voloshin, A., 1978. Method to produce uniform plane stress states with applications to fiber-reinforced materials. *Experimental Mechanics*, **18**, 141–146.

[8] Areias, P.M.A., de Sa, J.M.A. Cesar and Antonio, C.A. Conceicao, 2003. A gradient model for finite strain elastoplasticity coupled with damage. *Finite Elements in Analysis and Design*, **39**, 1191–1235.

[9] Armero, F. and Garikipati, K., 1996. An analysis of strong discontinuities in multiplicative finite strain plasticity and their relation with the numerical simulation of strain localization in solids. *International Journal of Solids and Structures*, **33**, 2863–2885.

[10] Armero, F. and Oller, S., 2000. A general framework for continuum damage models. I. Infinitesimial plastic damage models in stress space. *International Journal of Solids and Structures*, **37**, 7437–7464.

[11] Askes, H. and Sluys, L.J., 2002. Explicit and implicit gradient series in damage mechanics. *European Journal of Mechanics - A/Solids*, **21**, 379–390.

[12] Barenblatt, D.S., 1962. The mathematical theory of equilibrium cracks in brittle fracture. *Advances in Applied Mechanics*, **7**, 55–129.

[13] Bažant, Z.P. and Oh, B.H., 1983. Crack band theory for fracture of concrete. *Materials and Structures*, **16**, 155–177.

[14] Bažant, Z.P. and Pijaudier-Cabot, G., 1988. Nonlocal continuum damage, localization instability and convergence. *Journal of Applied Mechanics*, **55**, 287–293.

[15] Belytschko, T. and Black, T., 1999. Elastic crack growth in finite elements with minimal remeshing. *International Journal for Numerical Methods in Engineering*, **45**, 601–620.

[16] Belytschko, T., Fish, J. and Engelmann, B.E., 1988. A finite element with embedded localization zones. *Computer Methods in Applied Mechanics and Engineering*, **70**, 59–89.

[17] Belytschko, T., Lu, Y.Y. and Gu, L., 1995. Crack propagation by element-free Galerkin methods. *Engineering Fracture Mechanics*, **51**, 295–315.

[18] Belytschko, T., Liu, W.K. and Moran, B. (eds.), 1996. *Nonlinear finite elements for continua and structures*. J. Wiley & Sons.

[19] Beremin, F.M., 1981. Experimental and numerical study of the different stages in ductile rupture: Application to crack initiation and stable crack growth. Nemat-Nasser, S. (ed.), *Three-Dimensional Constitutive Relations and Ductile Fracture*, North-Holland, 85–205.

[20] Beremin, F.M., 1983. A local criterion for cleavage fracture of a nuclear pressure vessel steel. *Metallurgical Transactions*, **14A**, 2277–2287.

[21] Bhattacharjee, D. and Knott, J.F., 1994. Ductile fracture in HY100 steel under mixed mode I/mode II loading. *Acta Metallurgica et Materialia*, **42**, 1747–1754.

[22] Bittencourt, T.N., Wawrzynek, P.A., Ingraffea, A.R. and Sousa, J.L., 1996. Quasi-automatic simulation of crack propagation for 2D LEFM problems. *Engineering Fracture Mechanics*, **55**, 321–334.

[23] Boers, S.H.A., Schreurs, P.J.G. and Geers, M.G.D., 2005. Groove forming in food can lids. *International Journal of Solids and Structures*.

[24] Boroomand, B. and Zienkiewicz, O.C., 1999. Recovery procedures in error estimation and adaptivity. Part II: Adaptivity in nonlinear problems of elasto-plasticity behaviour. *Computer Methods in Applied Mechanics and Engineering*, **176**, 127–146.

[25] Børvik, T., Hopperstad, O.S., Berstad, T. and Langseth, M., 2001. Numerical simulation of plugging failure in ballistic penetration. *International Journal of Solids and Structures*, **38**, 6241–6264.

[26] Børvik, T., Hopperstad, O.S. and Berstad, T., 2003. On the influence of stress triaxiality and strain rate on the behaviour of a structural steel. Part II. Numerical study. *European Journal of Mechanics - A/Solids*, **22**, 15–32.

[27] Bouchard, P.O., Bay, F., Chastel, Y. and Tovena, I., 2000. Crack propagation modelling using an advanced remeshing technique. *Computer Methods in Applied Mechanics and Engineering*, **189**, 723–742.

[28] Brokken, D., 1999. *Numerical modelling of ductile fracture in blanking*. Ph.D. thesis, Eindhoven University of Technology.

[29] Brokken, D., Brekelmans, W.A.M. and Baaijens, F.P.T., 1998. Numerical modelling of the metal blanking process. *Journal of Materials Processing Technology*, **83**, 192–199.

[30] Brokken, D., Brekelmans, W.A.M. and Baaijens, F.P.T., 2000. Predicting the shape of blanked products: a finite element approach. *Journal of Materials Processing Technology*, **103**, 51–56.

[31] Camacho, G.T. and Ortiz, M., 1996. Computational modelling of impact damage in brittle materials. *International Journal of Solids and Structures*, **33**, 2899–2938.

[32] Camacho, G.T. and Ortiz, M., 1997. Adaptive Lagrangian modelling of ballistic penetration of metallic targets. *Computer Methods in Applied Mechanics and Engineering*, **142**, 269–301.

[33] Chao, Y.J. and Zhu, X.K., 1999. A simple theory for describing the transition between tensile and shear mechanisms in mode I, II, III. *Mixed-Mode Crack Behavior*, vol. STP 1359, ASTM, 41–57.

[34] Chen, Z.H., Chan, L.C., Lee, T.C. and Tang, C.Y., 2003. An investigation on the formation and propagation of shear band in fine-blanking process. *Journal of Materials Processing Technology*, **138**, 610–614.

[35] Comi, C. and Perego, U., 1996. A unified approach for variationally consistent finite elements in elastoplasticity. *Computer Methods in Applied Mechanics and Engineering*, **121**, 323–344.

[36] Comi, C. and Perego, U., 2004. Criteria for mesh refinement in nonlocal damage finite element analyses. *European Journal of Mechanics - A/Solids*, **23**, 615–632.

[37] Cosserat, E. and Cosserat, F., 1909. *Théorie des Corps Déformables*. Herman et fils.

[38] Cruse, T.A. (ed.), 1972. *Surface cracks: Physical problems and computational solutions*. American Society of Mechanical Engineers.

[39] Dawicke, D.S., Sutton, M.A., Jr., J.C. Newman and Bigelow, C.A., 1995. Measurement and analysis of critical CTOA for aluminum alloy sheet. *Fracture Mechanics*, vol. 25, ASTM, 358–379.

[40] de Borst, R. and Muehlhaus, H.B., 1992. Gradient-dependent plasticity: Formulation and algorithmic aspect. *International Journal for Numerical Methods in Engineering*, **35**, 521–539.

[41] de Borst, R., Sluys, L.J., Muhlhaus, H.-B. and Pamin, J., 1993. Fundamental issues in finite element analyses of localization of deformation. *Engineering Computations*, **10**, 99–121.

[42] de Borst, R., Pamin, J., Peerlings, R.H.J. and Sluys, L.J., 1995. On gradient-enhanced damage and plasticity models for failure in quasi-brittle and frictional materials. *Computational Mechanics*, **17**, 130–141.

[43] Dodds, R.H., Tang, J.R. and Tang, M., 1993. Numerical procedures to model ductile crack extension. *Engineering Fracture Mechanics*, **46**, 253–264.

[44] Dugdale, D.S., 1960. Yielding in steel sheets containing slits. *Journal of the Mechanics and Physics of Solids*, **8**, 100–108.

[45] Engelen, R.A.B., Geers, M.G.D. and Baaijens, F.P.T., 2003. Nonlocal implicit gradient-enhanced elasto-plasticity for the modelling of softening behaviour. *International Journal of Plasticity*, **19**, 403–433.

[46] Erdogan, F. and Sih, G.C., 1963. On the crack extension in plates under plane loading and transverse shear. *Journal of Basic Engineering*, **85**, 519–527.

[47] Espinosa, H.D., Zavattieri, P.D. and Emore, G.L., 1998. Adaptive FEM computation of geometric and material nonlinearities with application to brittle failure. *Mechanics of Materials*, **29**, 275–305.

[48] Feenstra, P.H. and de Borst, R., 1996. A composite plasticity model for concrete. *International Journal of Solids and Structures*, **33**, 707–730.

[49] Fleck, N.A. and Hutchinson, J.W., 1997. Strain gradient plasticity. *Advances in Applied Mechanics*, vol. 33, Academic Press, 295–361.

[50] Geers, M.G.D., 2004. Finite strain logarithmic hyperelato-plasticity with softening: a strongly nonlocal implicit gradient framework. *Computer Methods in Applied Mechanics and Engineering*, **193**, 3377–3401.

[51] Geers, M.G.D., Peijs, T., Brekelmans, W.A.M. and Borst, R. De, 1996. Experimental monitoring of strain localization and failure behaviour of composite materials. *Composites Science and Technology*, **56**, 1283–1290.

[52] Geers, M.G.D., Borst, R. De, Brekelmans, W.A.M. and Peerlings, R.H.J., 1998. Strain-based transient-gradient damage model for failure analysis. *Computer Methods in Applied Mechanics and Engineering*, **160**, 133–154.

[53] Geers, M.G.D., Ubachs, R.L.J.M. and Engelen, R.A.B., 2003. Strongly nonlocal gradient-enhanced finite strain elastoplasticity. *International Journal for Numerical Methods in Engineering*, **56**, 2039–2068.

[54] Ghosal, A.K. and Narasmhan, R., 1994. A finite element analysis of mixed mode fracture initiation by ductile failure mechanisms. *Journal of the Mechanics and Physics of Solids*, **42**, 953–978.

[55] Goijaerts, A.M., Govaert, L.E. and Baaijens, F.P.T., 2001. Evaluation of ductile fracture models for different metals in blanking. *Journal of Materials Processing Technology*, **110**, 312–323.

[56] Gurson, A.L., 1977. Continuum theory of ductile rupture by void nucleation and growth: part I - yield criteria and flow rule for porous ductile media. *Journal of Engineering Materials and Technology, Transactions of the ASME*, **99**, 1–15.

[57] Hallback, N., 1997. Mixed-mode I/II fracture behaviour of a high strength steel. *International Journal of Fracture*, **87**, 363–388.

[58] Hambli, R., 2001a. Comparison between Lemaitre and Gurson damage models in crack growth simulation during blanking process. *International Journal of Mechanical Sciences*, **43**, 2769–2790.

[59] Hambli, R., 2001b. Finite element simulation of fine blanking processes using a pressure-dependent damage model. *Journal of Materials Processing Technology*, **116**, 252–264.

[60] Hambli, R., Potiron, A. and Kobi, A., 2003. Application of design of experiment technique for metal blanking processes optimization. *Mécanique & Industries*, **4**, 175–180.

[61] Hinton, E. and Campbell, J.S., 1974. Local and global smoothing of discontinuous finite element functions using a least squares method. *International Journal for Numerical Methods in Engineering*, **8**, 461–480.

[62] Hopperstad, O. S., Børvik, T., Langseth, M., Labibes, K. and Albertini, C., 2003. On the influence of stress triaxiality and strain rate on the behaviour of a structural steel. Part I. Experiments. *European Journal of Mechanics - A/Solids*, **22**, 1–13.

[63] Hutchinson, J.W., 1968. Singular behaviour at the end of a tensile crack in a hardening material. *Journal of the Mechanics and Physics of Solids*, **16**, 13–31.

[64] Jirásek, M. and Zimmerann, T., 2001. Embeded crack model I: Basic formulation. *International Journal for Numerical Methods in Engineering*, **50**, 1269–1290.

[65] Kachanov, L.M. (ed.), 1986. *Introduction to Continuum Damage Mechanics*. Kluwer Academic Publishers.

[66] Klein, P.A., Foulk, J.W., Chen, E.P., Wimmer, S.A. and Gao, H.J., 2001. Physics-based modeling of brittle fracture: cohesive formulations and the application of meshfree methods. *Theoretical and Applied Fracture Mechanics*, **37**, 99–166.

[67] Komori, K., 2001. Simulation of shearing by node separation method. *Computers & Structures*, **79**, 197–207.

[68] Kwak, T.S., Kim, Y.J., Seo, M. K. and Bae, W. B., 2003. The effect of v-ring indenter on the sheared surface in the fine-blanking process of pawl. *Journal of Materials Processing Technology*, **143,144**, 656–661.

[69] Leblond, J.B., Perrin, G. and Devaux, J., 1994. Bifurcation effects in ductile metals with damage delocalization. *Journal of Applied Mechanics*, **61**, 236–242.

[70] Lee, E.H., 1969. Elastoplastic deformations at finite strains. *Journal of Applied Mechanics*, 1–6.

[71] Lee, N.S. and Bathe, K.J., 1994. Error indicators and adaptive remeshing in large deformation finite element analysis. *Finite Elements in Analysis and Design*, **16**, 99–139.

[72] Lee, T.C., Chan, L.C. and Wu, B.J., 1995. Straining behaviour in blanking process - fine blanking vs conventional blanking. *Journal of Materials Processing Technology*, **48**, 105–111.

[73] Lemaitre, J., 1984. Coupled elasto-plasticity and damage consitutive equations. *Computer Methods in Applied Mechanics and Engineering*, **51**, 31–49.

[74] Lemaitre, J. (ed.), 1992. *A Course on Damage Mechanics*. Springer.

[75] Lemaitre, J., Desmorat, R. and Sauzay, M., 2000. Anisotropic damage law of evolution. *European Journal of Mechanics - A/Solids*, **19**, 187–208.

[76] Lim, I.L., Jonhston, I.W. and Choi, S.K., 1996. A finite element code for fracture propagation analysis within elasto-plastic continuum. *Engineering Fracture Mechanics*, **53**, 193–211.

[77] Loubignac, G. and Cantin, G., 1977. Continuous stress fields in finite element analysis. *AIAA journal*, **15**, 1645–1647.

[78] Maccagno, T.M. and Knott, J.F., 1989. The fracture behaviour of PMMA in mixed modes I and II. *Engineering Fracture Mechanics*, **34**, 65–86.

[79] Mackenzie, A.C., Hancock, J.W. and Brown, D.K., 1977. On the influence of state of stress on ductile failure initiation in high strength steels. *Engineering Fracture Mechanics*, **9**, 167–188.

[80] Mahishi, J.M. and Adams, D.F., 1982. Micromechanical predictions of crack initiation, propagation, and crack growth resistance in boron/aluminum composites. *Journal of Composite Materials*, **16**, 457–469.

[81] McClintock, F.A., 1968. A criterion for ductile fracture by the growth of holes. *Journal of Applied Mechanics*, **35**, 363–371.

[82] Mediavilla, J., Peerlings, R.H.J. and Geers, M.G.D., 2004. A robust and consistent remeshing-transfer operator for ductile fracture simulations. *Submitted to Computers & Structures.*

[83] Mediavilla, J., Peerlings, R.H.J. and Geers, M.G.D., 2005a. A nonlocal triaxiality-dependent ductile damage model for finite strain plasticity. *To be submitted to Computer Methods in Applied Mechanics and Engineering.*

[84] Mediavilla, J., Peerlings, R.H.J. and Geers, M.G.D., 2005b. An integrated nonlocal cotinuous-discontinous approach towards damage engineering in metal forming processes. *To be submitted to Engineering Fracture Mechanics.*

[85] Mediavilla, J., Peerlings, R.H.J. and Geers, M.G.D., 2005c. Discrete modelling of ductile fracture driven by nonlocal softening plasticity. *To be submitted to International Journal for Numerical Methods in Engineering.*

[86] Moës, N., Dolbow, J. and Belytschko, T., 1999. A finite element method for crack growth without remeshing. *International Journal for Numerical Methods in Engineering*, **46**, 131–150.

[87] MSC.Software Co, 2001. *MSC.MARC manuals.*

[88] Nedjar, B., 2001. Elastoplastic-damage modelling including the gradient of damage: formulation and computational aspects. *International Journal of Solids and Structures*, **38**, 5421–545.

[89] Needleman, A., Tvergaard, V. and Hutchinson, J.W., 1992. *Void growth in plastic solids.* Springer-Verlag.

[90] Oliver, J., 1989. A consistent characteristic length for smeared cracking models. *International Journal for Numerical Methods in Engineering*, **28**, 461–474.

[91] Ortiz, M. and Quigley, J., 1991. Adaptive mesh refinement in strain localization problems. *Computer Methods in Applied Mechanics and Engineering*, **90**, 781–804.

[92] Ortiz, M., Leroy, Y. and Needleman, A., 1987. A finite element method for localized failure analysis. *Computer Methods in Applied Mechanics and Engineering*, **61**, 189–214.

[93] Oyane, M., Sato, T., Okimoto, K. and Shima, S., 1979. Criteria for ductile fracture and their applications. *Journal of Mechanical Working Technology*, **4**, 65–81.

[94] Patzák, B. and Jirásek, M., 2004. Adaptive resolution of localized damage in quasibrittle materials. *Journal of Engineering Mechanics Division ASCE*, **130**, 720–732.

[95] PavanaChand, Ch. and KrishnaKumar, R., 1998. Remeshing issues in the finite element analysis of metal forming problems. *Journal of Materials Processing Technology*, **75**, 63–74.

[96] Peerlings, R.H.J., 1999. *Enhanced damage modelling for fracture and fatigue.* Ph.D. thesis, Eindhoven University of Technology, The Netherlands.

[97] Peerlings, R.H.J., de Borst, R., Brekelmans, W.A.M. and Vree, J.H.P. De, 1996. Gradient enhanced damage for quasi-brittle materials. *International Journal for Numerical Methods in Engineering*, **39**, 3391–3403.

[98] Peerlings, R.H.J., Geers, M.G.D., de Borst, R. and Brekelmans, W.A.M., 2001a. A critical comparison of nonlocal and gradient-enhanced continua. *International Journal of Solids and Structures*, **38**, 7723–7746.

[99] Peerlings, R.H.J., Geers, M.G.D., de Borst, R. and Brekelmans, W.A.M., 2001b. A critical comparison of nonlocal and gradient-enhanced continua. *International Journal of Solids and Structures*, **38**, 7723–7746.

[100] Peerlings, R.H.J., de Borst, R., Brekelmans, W.A.M. and Geers, M.G.D., 2002. Localisation issues in local and nonlocal continuum approaches to fracture. *European Journal of Mechanics - A/Solids*, **21**, 175–189.

[101] Perić, D., Hochard, Ch., Dutko, M. and Owen, D.R.J., 1996. Transfer operators for evolving meshes in small strain elasto-placticity. *Computer Methods in Applied Mechanics and Engineering*, **137**, 331–344.

[102] Pirondi, A. and Bonora, N., 2003. Modeling ductile damage under fully reversed cycling. *Computational Materials Science*, **26**, 129–141.

[103] Pirondi, A. and Donne, C. Dalle, 2001. Characterisation of ductile mixed-mode fracture with the crack-tip displacement vector. *Engineering Fracture Mechanics*, **68**, 1385–1402.

[104] Pyttel, T., John, R. and Hoogen, M., 2000. A finite element based model for the description of aluminium sheet blanking. *International Journal of Machine Tools and Manufacture*, **40**, 1993–2002.

[105] Rachik, M., Roelandt, J. M. and Maillard, A., 2002. Some phenomenological and computational aspects of sheet metal blanking simulation. *Journal of Materials Processing Technology*, **128**, 256–265.

[106] Reusch, F., Svendsen, B. and Klingbeil, D., 2003. Local and non-local Gurson-based ductile damage and failure modelling at large deformation. *European Journal of Mechanics - A/Solids*, **22**, 779–792.

[107] Rice, J.R. and Rosengren, G.F., 1968. Plane strain deformation near a crack tip in a power-law hardening material. *Journal of the Mechanics and Physics of Solids*, **16**, 1–12.

[108] Rice, J.R. and Tracey, D.M., 1969. On the ductile enlargement of voids in triaxial stress fields. *Journal of the Mechanics and Physics of Solids*, **17**, 201–207.

[109] Rodriguez-Ferran, A. and Huerta, A., 2000. Error estimation and adaptivity for nonlocal damage models. *International Journal of Solids and Structures*, **37**, 7501–7528.

[110] Rots, J.G., 1991. Smeared and discrete representations of localized fracture. *International Journal of Fracture*, **51**, 45–59.

[111] Roy, S., Dexter, R.J. and Fossum, A.F., 1993. A computational procedure for the simulation of ductile fracture with large plastic deformation. *Engineering Fracture Mechanics*, **45**, 277–293.

[112] Selman, A., Hinton, E. and Bicanic, N., 1997. Adaptive mesh refinement for localised phenomena. *Computers & Structures*, **63**, 475–495.

[113] Shim, K.H., Lee, S.K., Kang, B.S. and Hwang, S.M., 2004. Investigation on blanking of thin sheet metal using the ductile fracture criterion and its experimental verification. *Journal of Materials Processing Technology*, **155–156**, 1935–1942.

[114] Sih, G.C., 1974. Strain-energy-density factor applied to mixed mode crack problems. *International Journal of Fracture*, **10**, 305–321.

[115] Simo, J.C., 1988a. A framework for finite strain elastoplasticity based on maximum plastic dissipation and the multiplicative decomposition: Part I. Continuum formulation. *Computer Methods in Applied Mechanics and Engineering*, **66**, 199–219.

[116] Simo, J.C., 1988b. A framework for finite strain elastoplasticity based on maximum plastic dissipation and the multiplicative decomposition: Part II. Computational aspects. *Computer Methods in Applied Mechanics and Engineering*, **68**, 1–31.

[117] Simo, J.C., 1992. Algorithms for static and dynamic multiplicative plasticity that preserve the classical return mapping schemes of the infinitesimal theory. *Computer Methods in Applied Mechanics and Engineering*, **99**, 61–112.

[118] Simo, J.C. and Ju, J.W., 1989. On continuum damage-elastoplasticity at finite strains. *Computational Mechanics*, **5**, 375–400.

[119] Simo, J.C. and Miehe, C., 1992. Associative coupled thermoplasticity at finite strains: formulation, numerical analysis and implementation. *Computer Methods in Applied Mechanics and Engineering*, **98**, 41–104.

[120] Simo, J.C., Oliver, J. and Armero, F., 1993. An analysis of strong discontinuities induced by strain-softening in rate-independent inelastic solids. *Computational Mechanics*, **12**, 277–296.

[121] Simone, A., Wells, G.N. and Sluys, L.J., 2003. From continuous to discontinuous failure in a gradient-enhanced continuum damage model. *Computer Methods in Applied Mechanics and Engineering*, **192**, 4581–4607.

[122] Sluys, L. J. and de Borst, R., 1992. Wave propagation and localization in a rate-dependent cracked medium–model formulation and one-dimensional examples. *International Journal of Solids and Structures*, **29**, 2945–2958.

[123] Steinmann, P., 1999. Formulation and computation of geometrically non-linear gradient damage. *International Journal for Numerical Methods in Engineering*, **46**, 757–779.

[124] Sutton, M.A., Zhao, W., Boone, M.L. and Reynolds, A.P., 1997. Prediction of crack growth direction for mode I/II loading using small-scale yielding and void initiation/growth concepts. *International Journal of Fracture*, **83**, 275–290.

[125] Sutton, M.A., Deng, X., Ma, F., Jr., J.C. Newman and James, M., 2000. Development and application of a crack tip opening displacement-based mixed mode fracture criterion. *International Journal of Solids and Structures*, **37**, 3591–3618.

[126] Svedberg, T. and Runesson, K., 2000. An adaptive finite element algorithm for gradient theory of plasticity with coupling to damage. *International Journal of Solids and Structures*, **37**, 7481–7499.

[127] Tang, C.Y. and Lee, W.B., 1995. Anisotropic damage of the 2024T3 aluminum alloy. *Scripta Metallurgica et Materialia*, **32**, 767–772.

[128] Taupin, E., Breitling, J., Wu, W. and Altan, T., 1996. Material fracture and burr formation in blanking results of FEM simulations and comparison with experiments. *Journal of Materials Processing Technology*, **59**, 68–78.

[129] Tvergaard, V., 1990. Material failure by void growth to coalescence. *Advances in Applied Mechanics*, **27**, 83–151.

[130] Tvergaard, V. and Needleman, A., 1984. Analysis of the cup-cone fracture in a round tensile bar. *Acta Metallurgica*, **32**, 157–169.

[131] Tvergaard, V. and Needleman, A., 1995. Effects of nonlocal damage in porous plastic solids. *International Journal of Solids and Structures*, **32**, 1063–1077.

[132] Vaz, M. and Owen, D.R.J., 2001. Aspects of ductile fracture and adaptive mesh refinement in damaged elasto-plastic materials. *International Journal for Numerical Methods in Engineering*, **50**, 29–54.

[133] Wawrzynek, P.A. and Ingraffea, A., 1991. *Discrete modeling of crack propagation: theoretical aspects and implementation issues in two and three dimensions*. Tech. rept., School of Civil Engineering and Environmental Engineering, Cornell University.

[134] Wells, A.A., 1963. Application of fracture mechanics at and beyond general yielding. *British Welding Journal*, **10**, 563–570.

[135] Wells, G.N. and Sluys, L.J., 2001. A new method for modelling cohesive cracks using finite elements. *International Journal for Numerical Methods in Engineering*, **50**, 2667–2682.

[136] Wells, G.N., Sluys, L.J. and de Borst, R., 2002. Simulating the propagation of displacement discontinuities in a regularised strain-softening medium. *International Journal for Numerical Methods in Engineering*, **53**, 1235–1256.

[137] Wilkins, M., 1964. Calculation of elastoplastic flows. Press, Academic (ed.), *Methods in Computational Physics*, vol. 3, 211–263.

[138] Wilson, 1998. *Can desing with easy open end*. International Application pusblished under the patent cooperation treaty. International Publication number WO 98/55366.

[139] Wu, C.H., 1978. Fracture under combined loads by maximum-energy-release-rate criterion. *Journal of Applied Mechanics*, **45**, 553–558.

[140] Zienkiewicz, O.C., Pastor, M. and Huang, M., 1995. Softening, localisation and adaptive remeshing. Capture of discontinuous solutions. *Computational Mechanics*, **17**, 98–106.

Samenvatting

In veel metaal-omvormprocessen (zoals ponsen, knippen, draaien en frezen) worden scheuren veroorzaakt om het materiaal te scheiden langs een gewenste productgeometrie. Deze soort van scheuren wordt voorafgegaan door en vergezeld van grote plastische vervormingen. Als gevolg hiervan is voor het creëren van het scheuroppervlak wezenlijk meer energie nodig dan de oppervlakte-energie van het breukvlak. Dit type breuk staat bekend als ductiele breuk, in tegenstelling tot brosse breuk (zoals in glas, keramiek, beton, etc.), waarbij relatief weinig energie gedissipeerd wordt. Ductiele breuk ontstaat op een microscopisch niveau door de vorming en groei van holten, meestal bij inclusies in het materiaal. Dit microscopische schadeproces leidt op macroscopische schaal tot een verzwakking van het materiaal ('softening'), lokalisering van deformatie en uiteindelijk tot het ontstaan van macroscopishe scheuren.

De initiatie en voortplanting van scheuren wordt veelal bestudeerd met behulp van breukmechanica. Echter, de toepassing van deze theorie op ductiele breuk, waar sterk niet-lineaire processen plaatsvinden (zowel materiaal- als geometrische niet-lineariteit) is controversieel. Om deze processen te beschrijven kunnen continuümmodellen gebruikt worden op basis van (softening) plasticiteit of continueschademechanica. Deze continuümmodellen kunnen echter geen scheurvoortplanting beschrijven, omdat de verplaatsingen in dat geval discontinu verlopen over de scheur. Het correct modelleren van ductiele breuk vereist daarom een nieuwe aanpak, waarbij een schademodel gecombineerd wordt met een strategie om scheuren (verplaatsingsdiscontinuïteiten) te modelleren. Het ontwikkelen van een dergelijke gecombineerde aanpak is het belangrijkste doel van het in dit proefschrift beschreven onderzoek. In de gekozen benadering worden scheuren expliciet beschreven door verplaatsingsdiscontinuïteiten, maar worden de snelheid en richting van scheurvoortplanting bepaald door de evolutie en lokalisering van (continue) schade. Dit is anders dan in een breukmechanica-benadering, waar aparte criteria worden gebruikt voor het bepalen van scheurgroeisnelheid en richting.

Continuümmodellen van degraderende materialen dienen een lengteschaal te bevatten om de localisering van schade te regulariseren en daarmee de goed-gesteldheid van het evenwichtsprobleem te garanderen. Zonder deze uitbreiding op de klassieke continuümsmechanica vertonen eindige-elementensimulaties een pathol-

ogische invloed van de gekozen ruimtelijke discretisatie. In dit werk wordt de lengteschaal geïntroduceerd door middel van een niet-lokale continuumformulering.

Voor het modelleren van verplaatsingsdiscontinuïteiten zijn tal van numerieke methoden beschikbaar. In het huidige kader wordt een remeshing-strategie gebruikt. Deze biedt bij toepassing op problemen met grote en sterk gelocaliseerde deformaties als voordelen dat een goede element-kwaliteit gegarandeerd kan worden en dat de elementen op ieder moment optimaal verdeeld kunnen worden over het domein.

Als eerste stap in de richting van een continuum-discontinuum aanpak, wordt eerst een ongekoppeld schademodel gebruik, waarin schade fungeert als een scheurvoortplantings-indicator, zonder het materiaalgedrag te beïnvloeden. Vanwege deze laatste beperking leidt dit model niet tot localisering van schade en kan de regularisering met behulp van niet-lokaliteit achterwege blijven. Een dergelijke benadering is gerechtvaardigd in het geval dat de grootte van het gebied waarin schadegroei plaatsvindt, de zogenaamde fracture process zone, zodanig klein is dat de invloed ervan verwaarloosd kan worden.

Wanneer de fracture process zone relatief groot is, dient een volledig gekoppelde aanpak gevolgd te worden, zoals die ontwikkeld wordt in het tweede gedeelte van deze studie. Door de degradatie van de lokale materiaalsterkte vindt de overgang van een continuüm naar een discrete scheur geleidelijk plaats, met een relatief geringe herverdeling van spanningen op het moment dat de scheur geïntroduceerd wordt of groeit. Dit is in tegenstelling tot de ongekoppelde aanpak, waarin de overgang van onbeschadigd continuüm naar discrete scheur gepaard gaat met een sprong in de spanningstoestand. Bij de gecombineerde aanpak wordt een bestaande niet-lokale schadeformulering gebruikt in de beschrijving van het verstevigings-/verzwakkingsgedrag van het materiaal. Deze aanpak is met succes toegepast op het voorspellen van ductiele breuk onder afschuif-belastingen.

Om het model geschikt te maken voor meer algemene belastingstoestanden is in het derde gedeelte van de studie de materiaalbeschrijving verbeterd door de invloed van de spanningstriaxialiteit op de schade-evolutie in rekening te brengen. Het model is afgeleid door gebruik maken van het continue-schadeconcept van effective spanningen. In de resultaten wordt getoond hoe de triaxialiteit (in druk en trek) de ductiliteit van het materiaal beïnvloedt.

Tenslotte is de gecombineerde aanpak toegepast op enkele metaal-omvormprocessen uit de praktijk, namelijk ponsen, fijnponsen, en score-vorming. Het constitutieve model is daartoe geïmplementeerd in een zogenaamde operator-split vorm, die aantrekkelijk kan zijn voor praktische toepassingen. Om de optredende grote rekgradiënten goed te kunnen beschrijven wordt een nieuwe vorm van mesh-adaptiviteit voorgesteld. De resultaten van de simulaties komen goed overeen met experimentele gegevens uit de literatuur.

Dankwoord

Graag wil ik mijn begeleiders Ron Peerlings en Marc Geers bedanken voor de uitstekende begeleiding en de nodige kritiek tijdens mijn promotie. Zonder hun ondersteuning zou dit proefschrift nooit tot stand zijn gekomen. De vrijheid die bij de MATE groep heb kunnen genieten was onmisbaar om dit onderzoek tot een goed einde te brengen. In het bijzonder wil ik het NIMR bedanken, als top instituut, voor zijn bijdrage aan dit onderzoek.

Dank aan mijn kamergenoten (Sebastian Boers, Shangping Chen, Roel Janssen, René Ubachs), ex-kamergenoten (Ivan Bazhlekov, Edwin Klompen, Varvara Koutznezova, Harold van Melick en Alex Zdravkov) en de andere collega's van de MATE-groep (in het bijzonder Alpay Aydemir, Adnan Abdul-Baqi, Maurice van der Beek, Kristel Boonen, Marco van den Bosch, Peter Janssen, Yuriy Kasyanyuk, Viny Khatavkar, Tibor Fülop, Abdul Matin, Ruchi Rastogi en Katja Viatkina) voor de leuke gesprekken en gezellige sfeer. Ik wil ook Dirk Brokken bedanken, die mijn voorganger in dit onderzoek was, en wiens hulp aan het begin cruciaal is geweest. Bedankt ook aan Leo Wouters, Patrick van Brakel en Alice van Litsenburg voor hun ondersteuning. Ook wil ik de leden van de kern commissie Han Huétink, Bert Sluys en Kouchi Zhang bedanken.

Ik wil mijn ouders, mijn broer en zus bedanken voor hun geduld en vertrouwen. Tot slot wil ik mijn lieve Hong bedanken voor al de tijd die wij samen achter de PC hebben doorgebracht, en zonder wie deze opgave veel zwaarder en minder leuk was geweest. De komende tijd zal ik aan haar toewijden.

Jesus Mediavilla Varas
Eindhoven, 24 februari 2005

Curriculum vitae

11 August 1971	Born in Ciudad Real, Spain.
1989 – 1995	Ingeniero superior de Caminos, Canales y Puertos (Master in Civil Engineering). Specialty: Structures and Foundations.
1995 – 1996	Second lieutenant in the Spanish Army (Corps of Engineers).
1996 – 1997	Worked as a civil engineer in Spain.
1998 – 1999	Spanish Embassy in The Netherlands.
1999 – 2000	Worked as a civil engineer in The Netherlands.
2000 – 2004	PhD student; NIMR (Netherlands Institute for Metals Research) cluster 2 and Eindhoven University of Technology (Mechanical Engineering Faculty, MaTe: Materials Technology) in the group of Prof.Dr.Ir.M.G.D. Geers. Research topic: "Continuous and discontinuous modelling of ductile fracture", which is the object of this thesis.